12-17-2015

Evaluation of Solid Oxide Fuel Cell Interconnect Coatings: Mechanisms Behind Structure and Property Change During Reaction Layer Formation

Louis V. Gambino
University of Connecticut, louis.gambino@uconn.edu

Evaluation of Solid Oxide Fuel Cell Interconnect Coatings:

Mechanisms Behind Structure and Property Change

During Reaction Layer Formation

Louis Victor Gambino, PhD

University of Connecticut, 2015

Modern solid oxide fuel cells (SOFCs) operate at sufficiently low temperatures to allow the use of alloy interconnects in the SOFC stacks. The alloys used are cheaper, more formable, and more conductive than the traditional ceramic materials used for interconnects. However, the long term SOFC performance is limited by oxidation of the alloy interconnect. To ameliorate the issues which result from oxidation, manganese cobaltite spinel coatings are typically applied.

The microstructural effects of the reduction step in the reactive consolidation of slurry processed $Mn_{1.5}Co_{1.5}O4$ (MCO) coated Crofer 22 APU were studied. The reduced coating contained particles of MnO with the NaCl structure and Co with the face centered cubic (FCC) structure. The interface exhibited a thin dense chromia layer with a thicker porous $MnCr_2O_4$ over-layer with needle-like protrusions into the reduced coating. The consequences of these observations for the complex microstructural variation during subsequent re-oxidation are discussed.

The effects of Cr, Ni, and Fe substitution into MCO spinels are of great interest due to the roles that the diffusion of these cations play in reaction layer development during high temperature exposure of MCO-coated alloys. Here a study is reported on a series of model Cr-,

Ni-, and Fe-substituted MCO spinel ceramics. The cation site occupancies in these samples have been studied by X-ray spectrometry- based Atom Location by CHanneling Enhanced MIcro-analysis (ALCHEMI) experiments in the transmission electron microscope. These ALCHEMI data could provide a useful insight into the role of cation sub-lattice site preference in the formation of reaction layers in MCO-coated stainless steels and superalloys.

The use of pulsed laser deposition to produce high-quality manganese cobaltite spinel coatings on Crofer 22 APU substrates has been investigated. It is shown that deposition from ceramic MCO targets in a N_2 environment results in smooth, dense polycrystalline coatings comprised of rock-salt (Mn,Co)O and FCC Co phases. Post-deposition annealing in laboratory air led to re-oxidation of the coatings to give spinel phases with a thin chromia layer at the interface with the substrate. There are local variations in the porosity and surface morphology of the coating, which appear to be correlated with the orientation of the underlying substrate grains. These observations indicate that control of grain structure in the substrate may be necessary to promote microstructural stability in such coatings.

Evaluation of Solid Oxide Fuel Cell Interconnect Coatings:

Mechanisms Behind Structure and Property Change

During Reaction Layer Formation

Louis Victor Gambino

B.A., Rutgers, The State University of New Jersey, 2011

A Dissertation

Submitted in Partial Fulfillment of the

Requirements for the Degree of

Doctor of Philosophy

at the

University of Connecticut

2015

APPROVAL PAGE

Doctor of Philosophy Dissertation

Evaluation of Solid Oxide Fuel Cell Interconnect Coatings:

Mechanisms Behind Structure and Property Change

During Reaction Layer Formation

Presented by
Louis V. Gambino, B.A.

Major Advisor _____
Mark Aindow

Associate Advisor _____
Ramamurthy Ramprasad

Associate Advisor _____
George A. Rossetti, Jr.

University of Connecticut
2015

Acknowledgements

I would like to give a special thanks to my thesis advisor, Prof. Mark Aindow, for all that he has taught me in Materials Science and Engineering, how to convey my ideas clearly in oral and written form, and his patience throughout my dissertation. I would also like to thank my associate advisors, Prof. Ramamurthy Ramprasad and Prof. George Rossetti for their insightful lectures and thoughtful guidance at my thesis proposal. I would like to highlight the contributions that my principal investigator, Dr. Neal Magdefrau, had on my thesis. He has helped me find key areas for novel and important research and has shown me what research is like in industry.

I would especially like to thank Dr. Roger Ristau and Dr. Lichun Zhang for their in-depth electron microscopy training and also maintaining the equipment necessary for me to complete my thesis. To the past and present members of the Aindow Research Group, I would like to thank you for your support in and out of the laboratory.

I would like to thank Prof. Lisa Klein for introducing me to scientific research at Rutgers University, where I first discovered my passion. Equally contributing was Prof. Andrei Jitianu who was there to monitor my progress and give me the confidence to apply for graduate school.

I would like to thank my family for supporting me throughout my education. My mother, Mary Frances Gambino, for ensuring that I remained healthy and caring for me when sick. My father, Salvatore Gambino, for pushing me to do my best and helping me focus on areas which need improvement. My brother, Jonathan Gambino, for keeping me on the right track. My brother, Philip Gambino, for helping me stay motivated. My grandmother, Irene Gambino, for reminding me to take into consideration everything else besides my work. I feel forever in debt to all of these people as well as my sweetheart, Nicole Chin, for your love and compassion.

Preface

The enclosed thesis is comprised of research performed collaboratively at the University of Connecticut and United Technologies Research Center. This work is entirely original and has not been previously used for the completion of a degree at this or any other university. The work enclosed was completed on a full-time basis from 2011-2015. The majority of this work was paid for by the National Science Foundation under Grant No. 1100427. Chapters 3, 4, and 5 are taken from original published and submitted works by the current author and are referenced below:

Chapter 3: L. V. Gambino, N.J. Magdefrau, and M. Aindow, "Microstructural effects of the reduction step in reactive consolidation of manganese cobaltite coatings on Crofer 22 APU," *Mater. High Temp.*, **32** [1–2] 142–147 (2015).

Chapter 4: L. V. Gambino, A.B. Freeman, N.J. Magdefrau, and M. Aindow, "ALCHEMI studies of site occupancies in Cr-, Ni-, and Fe-substituted manganese cobaltite spinels," *J. Mater. Sci.*, **1** [1] (in press) (2015).

Chapter 5: L. V Gambino, N.J. Magdefrau, and M. Aindow, "Microstructural evolution in manganese cobaltite films grown on Crofer 22 APU substrates by pulsed laser deposition," *Surf. Coat. Technol.*, (submitted).

Table of Contents

Chapter 1: Introduction

1.1 Current Fuel Cell Technology

The impetus for the technological development of fuel cells is due to their inherent capability to provide clean and efficient electricity from fuel. Development of fuel cell technology is necessary for fuel cells to surpass gas turbines which have been so well engineered to provide cheap and reliable electricity. Fuel cells have an advantage because the efficiency of the gas turbine engine is limited by the Carnot cycle [1]. The temperature and pressure difference between the combustion chamber and exhaust duct cannot be increased much further than 900 °C and 50 atm due to the thermal properties of the turbine blades and the friction of air flow [2, 3]. In fuel cells, these intermediate steps of producing heat and mechanical work to generate electricity are avoided with electrochemistry [4].

In the electrochemical reaction, electricity and heat are the byproducts of combining hydrogen and oxygen ions. In a fuel cell, the temperature window of operation is determined by an ion permeable electrolyte which separates the fuel and oxidant. In turn, the temperature window dictates the type of catalysts and fuel that can be used. Therefore, the material and operation cost of a fuel cell is determined by the type of electrolyte.

Proton exchange membrane fuel cells (PEMFCs) are the most common low temperature (LT) devices. The temperature of the polymer electrolyte must be kept below 100°C because the proton exchange mechanism is assisted by liquid water. Pt is generally used as a catalyst at

LT, which limits the feedstock to pure H_2. The high cost of Pt and H_2 make production of electricity with PEMFCs expensive. Expensive electricity is only acceptable for special applications, such as hand held devices and transportation.

Solid oxide fuel cells (SOFCs) are a promising technology to replace or run in conjunction with turbine power plants to increase efficiency [5,6]. SOFCs are run at high temperatures to allow sufficient ion transport across the solid oxide electrolyte. High temperatures permit the use of a variety of cheap catalysts and fuels. Therefore, power can be supplied to a microgrid at competitive prices. However, the high operating temperatures are associated with long term degradation issues of major cell components. The rate and extent of degradation must be addressed so that the high capital cost of the SOFC system can be offset over time with the cheap generation of electricity [7].

Presently, the consumer base for SOFCs is limited to the commercial and industrial sector. Affordable electricity from SOFCs is able to be attained through the manufacture of high power units because of economies of scale. In 2013 the largest fuel cell supplier, Bloom Energy, has made high power SOFC installations across the U.S which provide 81.4 MW of power in total. Bloom Energy's largest SOFC installation, 30 MW, was for a utilities company in Delaware called Delmarva Power [8]. SOFC have commonly been installed at companies which must have uninterrupted power for their computer servers, such as Google, eBay, Verizon, and JPMorgan Chase, and for critical experiments, such as Life Technologies [8]. Walmart has 35 SOFC units supporting stores and distribution centers which will allow them to operate during blackouts [8]. After purchasing and experiencing the benefits of SOFCs firsthand many companies have

purchased additional or even larger SOFC systems [9]. Continued research and development is required to make a wide scale deployment of SOFC power plants [10].

1.2 Solid Oxide Fuel Cell Operation and Design

The electrolytically active components of a SOFC are the cathode, anode, and electrolyte [11]. In Figure 1.1, oxygen gas flows through the porous cathode and is reduced at high energy sites. Oxygen ions then diffuse through the dense electrolyte, reach the anode, and oxidize the fuel producing electricity and heat [12]. Considering methane as the fuel, the chemical reactions for fuel reforming and water-gas shift are shown in Equations 1.1 and 1.2 and are necessary for the electrochemical reaction shown in Equation 1.3.

$$CH_4 + H_2O \leftrightarrow CO + 3H_2 \quad (1.1)$$

$$CO + H_2O \leftrightarrow CO_2 + H_2 \quad (1.2)$$

$$H_2 + \frac{1}{2}O_2 \leftrightarrow H_2O \quad \Delta G = -237 \text{ kJ/mol and } \Delta H = 286 \text{ kJ/mol} \quad (1.3)$$

The heat released from the water-gas shift and electrochemical reaction is recycled to preheat

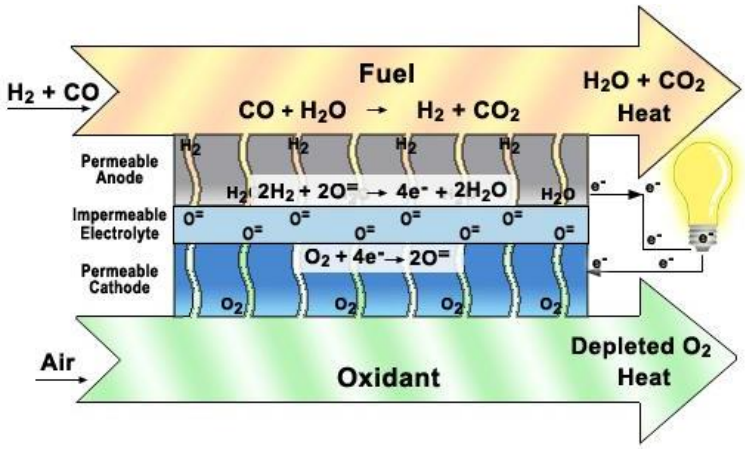

Figure 1.1: Schematic of how the fuel cell components facilitate the electrochemical reaction [Reproduced from 12].

the air entering the cathode and convert the water at the anode inlet to steam.

The maximum electrical efficiency of an electrochemical reaction is [12]:

$$\eta_{rev} = \Delta G/\Delta H \tag{1.4}$$

Using Equation 1.4 with the reaction in Equation 1.3, 83% of the energy released from the oxidation of hydrogen can harnessed in the form of electricity.

The following series of Equations describes the relationship between the energy that is put to work in the form of electricity and lost in the form of heat. Equation 1.5 is the reversible isothermal condition of Gibb's free energy:

$$\Delta G = \Delta H - T\Delta S \tag{1.5}$$

Equation 1.6 is the change in entropy:

$$\Delta S = \frac{Q}{T} \tag{1.6}$$

Enthalpy, ΔH, can be defined as the amount of energy not released as heat, Q, due to the production of work, W.

$$\Delta H = Q - W \tag{1.7}$$

In this case, W is the electrical work and is equal to ΔG by combining Equations 1.5, 1.6, and 1.7.

$$\Delta G = Q - W - T\frac{Q}{T} = -W \tag{1.8}$$

The actual electrical efficiency of the cell can be calculated by comparing the actual voltage and the maximum voltage. The maximum voltage of a cell is:

$$E_{rev} = -\frac{\Delta G}{2F} \tag{1.9}$$

Where the constant, 2, comes from the number of moles of electrons produced in the reaction. F is the Faraday constant, 96,485 C/mole, for the charge on one mole of electrons. Based on the reaction in Equation 1.3, E_{rev} = 1.23 V.

The actual cell voltage, *E*, is affected by polarization losses [13]:

$$E = E_{rev} - V_{act} - V_{ohm} - V_{conc} \quad (1.10)$$

The activation polarization, V_{act}, depends on the catalytic efficiency of the electrodes. The ohmic polarization, V_{ohm}, is due to the ohmic resistance of the electrolyte, electrodes, and the current collectors, interconnects, and their interfaces. The concentration polarization, V_{conc}, depends on the concentration of gases through the entire cross-section of the electrodes.

The current density of each cell is proportional to the inlet molar flow rate of fuel and oxygen. The flow rate is adjusted to maximize the power density with respect to the overall efficiency of the cell [14]. As shown in Figure 1.2, there are three distinct regions of polarization loss with increasing current density. Firstly, activation loss dominates due to the rate limit of fuel and oxygen reduction [15]. Secondly, ohmic loss occurs primarily due to the rate limit of ion transport and increases linearly. Lastly, at high flow rates a sharp drop occurs due to the transport and mechanical limits of the pressure needed to distribute

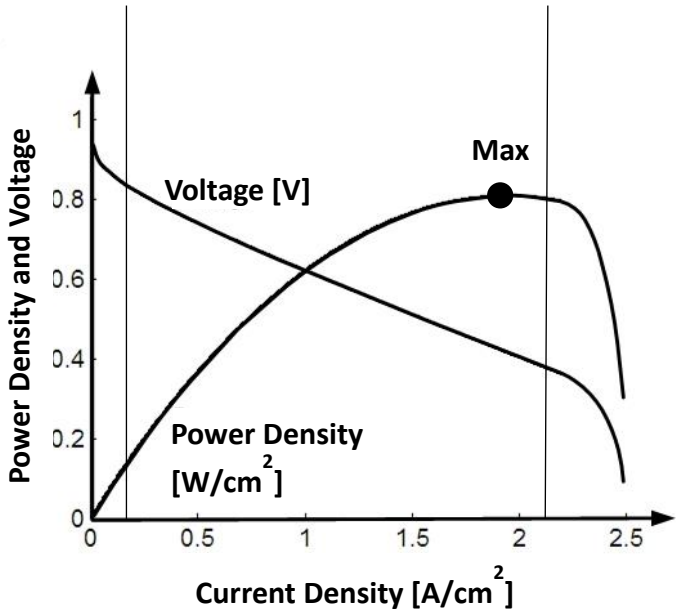

Figure 1.2: Electrical characteristics of a SOFC as a function of current density.

fuel/steam and oxygen through the porous electrodes [16]. A maximum fuel conversion efficiency of 85% is achieved when SOFCs are combined with turbine engines to operate at pressures close to 8 bar [17]. With these three limitations, the optimum cell potential, *E,* is around 0.7 V (Seok Lee). With this voltage the actual electrical efficiency of the cell can be calculated by the Equation:

$$\eta = E/E_{rev} \tag{1.11}$$

State of the art SOFCs operate with an electrical efficiency of $\eta = 0.7$ V/1.23 V = 0.6, which is twice the electrical efficiency of gas turbine engines.

On-site combined heat and power (CHP) SOFC systems allow recovery of the generated heat which is an essential resource for manufacturing plants. The high concentration of CO_2 in the anode exhaust allows for cheap and efficient carbon capture (CC) making SOFCs a solution to greenhouse gas emission. In a carbon-constrained society with penalties on carbon emission, the cost of SOFC-CHP-CC power can currently compete with gas turbine power at 410 $/KWe (the unit KWe stands for Kilowatt electric and represents the amount of electrical power produced) [18]. The generated heat plays a pivotal role in sustaining the kinetics necessary for ion transport through the solid oxide electrolyte. The ceramic microstructure and material make-up of the active layers depicted in Figure 1.1 are shown in Figure 1.3. The electrode materials, Ni-yttria stabilized zirconia (YSZ) and La-based perovskites

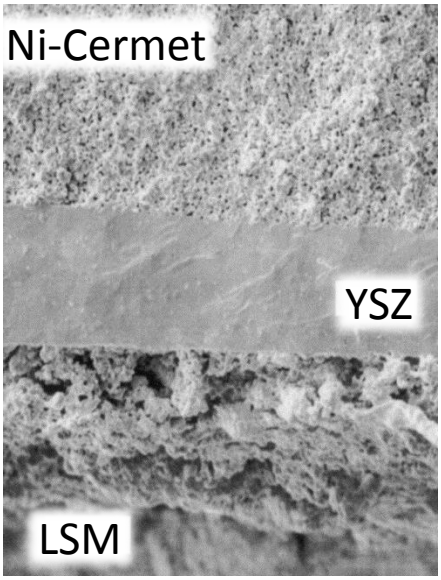

Figure 1.3: Secondary electron micrograph of a Ni-YSZ anode, 10 μm thick electrolyte, and cathode layers shown from top to bottom [Reproduced from 23].

[19] have been chosen based on their interaction with the YSZ electrolyte [20]. The mechanical and oxygen ion transport properties of YSZ make this an exceptional electrolyte material. There have been advancements in processing of the layers through doping and creating a composition variation to reduce polarization losses [21,22]. However, the key development was in sol-gel deposition which has allowed industry to effectively fabricate cells with a dense YSZ electrolyte layer less than 10 μm thick [23]. The reduction in thickness from conventionally 200 μm screen printed YSZ layers allows a greater flux of oxygen ions at a lower operating temperature. A drop in operation temperature from (950° - 1000°C) to (650°C – 800°C) has enabled materials with lower temperature constraints to be used in SOFC manufacture [24].

1.3 Interconnects

SOFCs are manufactured in stacks to increase the combined voltage of the cells, minimize material and fabrication cost, maintain internal heat, and provide compact power. There are two common SOFC stack designs that can achieve these feats, tubular [25] and flat plate [26]. The material specifications for both of these designs are similar [27]. The repeat elements which make up a SOFC stack are illustrated in Figure 1.4. They consist of a cathode, electrolyte, and anode layer joined to an interconnect with a conductive contact paste. The interconnect

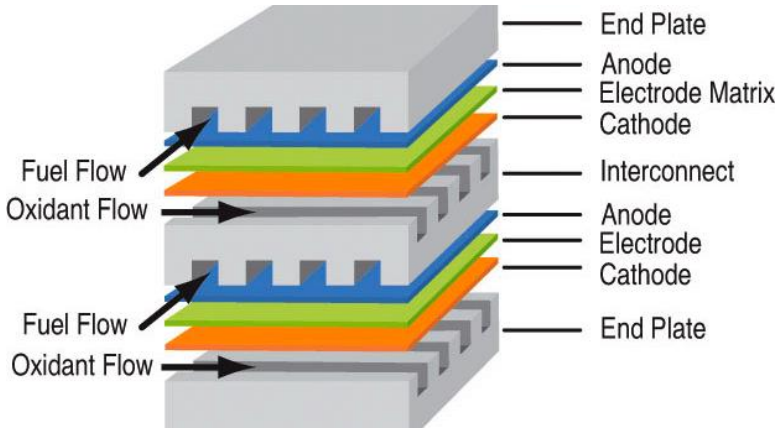

Figure 1.4: Illustration of the flat plate design used for SOFC stacks.

separates each cell in the stack providing a framework for structural stability, fuel and air flow, and electrical current.

High temperature ion conducting ceramic interconnects [28,29], can now be replaced with intermediate temperature metallic interconnect alloys due to the lower temperature constraints [30]. The main drive for using metallic interconnects is that they are cheaper to fabricate, have a better mechanical durability, and have a higher conductivity [31]. There is an extensive list of requirements that interconnects must fulfill due to the multiple roles they play. This list includes:

- Low cost by volume since the interconnect is a repeat component which can attribute up to $10/kW to the cost of an $80/kW stack.
- Ease of fabrication to reduce the cost necessary for complex manufacturing of gas channels that will seal properly.
- Electrical conductivity greater than 1 S/cm for economic efficiency.
- Coefficient of thermal expansion (CTE) within a range of 11 – 13 ppm/K to match the electrodes and electrolyte so that the thermal stresses developed during start-up and shut-down can be minimized.
- Impervious to oxygen and hydrogen gas to prevent direct combination of oxidant and fuel from the cathode and anode side.
- Adequate strength and creep resistance at elevated temperatures.
- No reaction or interdiffusion between the interconnect and its adjoining components.
- Excellent oxidation, sulfidation, and carbon cementation resistance.

Interconnects must maintain performance while operating in the severe conditions of the cathode and anode environment [32]. No material, metal or ceramic, can meet all of these demands. The two classes of materials that have been given considerable interest are Ni-based superalloys and ferritic stainless steel (FSS) alloys. Ni-base superalloys generally have TEC values higher than the ceramic electrode materials. To account for the TEC mismatch, a monolithic SOFC stack design is used with an anode support structure and the Ni-based superalloy is just a wire mesh current collector [27]. FSS alloys are much more common because the CTE has a better match to the ceramic electrode materials allowing SOFC stacks to be supported by the interconnect [27]. FFS alloy interconnects are manufactured as cold rolled sheets with the gas channels pressed and the repeat units welded together to provide a gas tight seal [33].

Commercial interconnect alloys have been developed using microalloying elements to enhance their heat resistant properties. The leading commercial alloy, is a FSS supplied for auxiliary power units (APUs), called Crofer 22 APU [34,35]. The high temperature oxidation properties of this alloy set it apart from conventional FSS because manganese chromite forms above the chromia scale to provide enhanced performance. However, this alloy and all others still have problems with the long term degradation.

1.4 IT-SOFC Degradation Derived from Alloy Interconnects

The Solid State Energy Conversion Alliance (SECA), a program dedicated to the research, development, and commercialization of SOFC technology, has set a goal for SOFCs to last 40,000 hours with a degradation rate less than 0.2% per 1000 hours. Therefore, over the lifetime of the SOFC stack, a voltage drop of 8% would make the production of electricity from

SOCF stacks economically inefficient. 21% degradation was observed in 1000 hours of SOFC operation using the leading commercial alloy interconnect, Crofer 22 APU [36]. The majority of the degradation observed was due to ohmic and activation losses caused by the alloy interconnect.

Initially, the electrical current between the alloy interconnect and electrode is based on the conductivity of the $(La,Sr)_1(Co,Fe)_1O_3$ contact layer (230 S/cm) [37]. Over time a chromia and $Mn_1Cr_2O_4$ scale, both with a conductivity of 0.02 S/cm at 800°C, develop on the surface of the Crofer 22 APU alloy interconnect causing a voltage drop of 3-4.3%/1000 hours [38].

Degradation is also caused by volatile Cr species that transport from the $Mn_1Cr_2O_4$ surface [39,40], through the porous cathode, and deposit at the cathode/electrolyte interface [41]. The formation of chromia at triple phase boundaries and the electrolyte interface causes a reduction in catalytic activity and ion transport [42]. Continued growth of the scale leads to stress between the interconnect and contact layer and has been projected to result in mechanical failure at 4750 hours [43].

1.5 Protective Coatings

A protective coating is required to retard the oxidation kinetics of the interconnect alloy and to inhibit Cr volatility [42]. The requirements that apply to interconnects, listed in Section 1.3, also apply to their coatings. Several coating materials, deposition, and consolidation methods have been studied. The successful materials have been able to form a dense and adherent coating that has a high electronic conductivity and low ionic conductivity.

La-based perovskites doped with alkaline earth [43], transition [44], and rare earth metals [45] were first evaluated as a possible coating material due to their use as electrode and ceramic interconnect materials. Perovskite is an AB_2O_3 compound with a structure dependent on the composition and processing conditions. Rare earth and alkali earth elements substitute into the A sublattice and transition metals typically substitute into the B sublattice. The large ionic radius and electron configuration of La results in a crystal structure and density of states conducive to electronic conduction. The electronic conductivity can be increased further by doping with Sr to increase the carrier concentration and decrease the effective mass [46]. The only success that has been reported for La-based perovskites, has been in the form of dense films achieved by advanced deposition techniques [47, 48, 49, 50, 51, 52, 53, 54].

The temperature necessary for sintering perovskites is near the melting point of alloy interconnects which prevents the use of scalable deposition techniques to achieve consolidated coatings [55, 56, 57, 58]. Without proper coating densification, the volatile Cr compounds have a short circuit path through the pore structure to reach and poison the cathode [59, 60]. Also, there have been several reports of the formation of a Sr-chromite phase at the interface of the alloy interconnect, which have led to increased ohmic resistance [61, 62 63, 37] and spallation [64]. Lastly, the ionic conductivity of perovskites is generally too high to slow down the ingress of oxygen and egress of chromium [65, 66]. The degree of ionic conductivity is a result of the oxygen vacancies which provide a defect free path for ion transport [67, 68, 69]. A new field of research has emerged to take advantage of the electronic conductivity mechanism in spinels, allowing for charge transfer to occur at high temperature without significant Cr and oxygen ion diffusion.

Manganese cobaltite based spinels have proven to be a superior material for protective interconnect alloy coatings. Larring and Norby first reported the use of $Mn_{1.5}Co_{1.5}O_4$ (MCO) coatings to increase the interfacial contact area between the cathode and alloy interconnect and to limit Cr volatilization and Sr-chromite phase formation [53]. MCO was able to form a dense adherent layer between the alloy interconnect and cathode to increase charge transfer [53]. Relatively dense MCO coatings are achieved using a two-step reactive sintering technique of reduction and re-oxidation [53, 59, 70, 71]. $(Mn,Co)_3O_4$ based spinels have received the most attention because of their phase stability [72], high electronic conductivity [73], matching CTE [74], and ability to limit chromia scale growth and Cr volatilization [75, 76] by forming a Cr-rich spinel reaction layer (RL) [77]. The performance of the MCO coating degrades with the extent of this RL since Cr substitution lowers the conductivity [74] and increases the potential for Cr volatilization [78].

1.6 IT-SOFC Degradation Derived from Manganese Cobaltite Spinel Coated Alloy Interconnects

The best performance of an interconnect alloy and coating has been shown to be Crofer 22 APU with MCO based spinels. However, the service lifetime with this interconnect and coating combination still falls short of the 40,000 hour requirement. Megel et al. have recorded the area specific resistance across an interconnect of Crofer 22 APU coated with an MCO based spinel in SOFC conditions for 12,000 hours [38]. The increase in ohmic resistance due to the growth of the chromia scale and Cr-rich spinel RL contributed to the degradation of the SOFC stack at a rate of 0.25%/1000 hours. At this

rate an 8% drop in voltage would occur at 32,000 hours, making the stack economically inefficient [38]. Liu et al. have projected MCO coated Crofer 22 APU interconnects to mechanically fail after 15,000 hours due to spallation and delamination with the contact layer [41]. The effect of Cr poisoning on the degradation of the SOFC stack has yet to be quantified but spinel coatings have successfully reduced Cr volatility by 99% from bare Crofer 22 APU during the first 1000 hours [75].

1.7 Structure of This Thesis

In Chapter 2, the reasoning is provided for the selection of Crofer 22 APU to be the interconnect alloy of study in this thesis. A literature review is given on the oxidation of Crofer 22 APU with a focus on the development of the chromia scale. Then the coating materials of interest, spinel, is explained in terms of its structure, properties, and interaction with Crofer.

In Chapter 3, a study on the effect of the processing parameters necessary for the consolidation of MCO coatings and their effect the coating performance is given.

In Chapter 4, the cation site occupancy of MCO-based spinels is related to the development of spinel reaction layers between interconnect alloys and MCO coatings.

In Chapter 5, an investigation on the interaction of pulsed laser deposited MCO films with Crofer 22 APU is provided.

Chapter 2: Background

2.1 Interconnect Alloy

2.1.1 Evaluation and Selection of Heat-Resistant Alloys for IT-SOFC Interconnects

A comprehensive analysis of the types of alloys that will satisfy the properties necessary for IT-SOFC interconnects has been performed in 2003 at the Pacific Northwest National Laboratory [79]. In this study, alloys which form chromia and alumina (α-Al_2O_3) scales were considered. Alumina forming alloys have a superior oxidation resistance and a lower volatilization rate but, the conductivity of alumina is 10^5-10^6 times lower than chromia [80]. The alumina forming alloys can be used in an alternate SOFC design as the structure for the repeat units of the stack and as the channel for air and gas flow, but not as a current collector. Chromia forming alloys are the best candidate for interconnects in the conventional IT-SOFC design due to the semi-conductive nature of their scale. A key focus of this study was determining the minimum content of chromium necessary to form a continuous chromia scale in order to reduce cost.

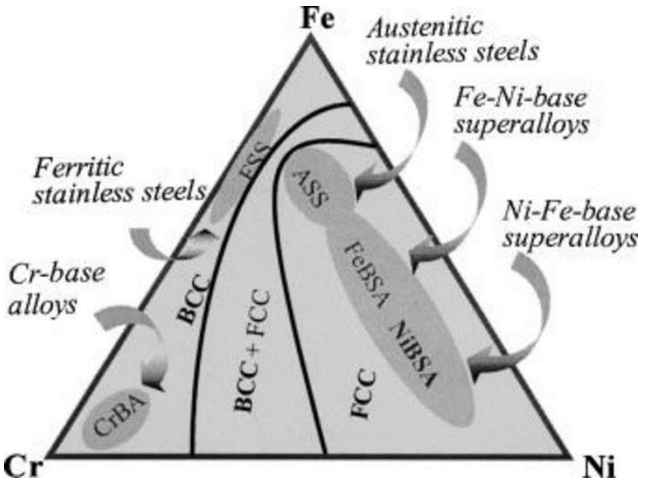

Figure 2.1: Schematic of alloy design for SOFC interconnects [Reproduced from 79].

The material classes of chromia forming alloys are represented schematically in Figure 2.1 in a Fe-Ni-Cr phase diagram [32]. All of these materials have a similar oxidation resistance, but only the ferritic stainless steel (FSS) and Cr-based alloys have a matching CTE with cell components due to their body centered cubic (BCC) crystal structure. The low cost and manufacturability of FSS make this material class superior to Cr-based alloys. The researchers at PNNL established FSS alloys as the best candidate material for interconnects and set the groundwork for future research.

Wilem J. Quadakkers, head of the Corrosion Protection Department at the Jülich Research Center, has set in motion the development of FSS alloys with properties specific to interconnect requirements [81, 82]. Supported by ThyssenKrupp Nirosta and ThyssenKrupp VDM, they have made the interconnect material, Crofer 22 APU, commercially available which satisfies several of the material requirements. Emphasis was put on the growth and adherence of the oxide scales, their contact resistance at service temperature, and their interaction with various perovskite-type contact materials. The refined alloy relies on the addition of Mn, La, Ti, Si, and Al alloying elements to achieve the desired performance. Crofer 22 APU was first released in 2003 and is described in the ThyssenKrupp forum as the answer to the production problems and cost factors inhibiting large scale manufacture of SOFCs [83].

Implementing the production of Crofer 22 APU involved melting with a narrow tolerance in composition and modifying techniques for thermo-mechanical processing of the steel, which has poor hot forming properties, to achieve a sheet thickness of 0.5 mm [83]. In 2002, batch compositions with varied amounts of Mn, Ti, and La were studied and compared to similar commercial alloys after oxidation in simulated cathode and anode environments [84]. It

is this investigation in which the best alloy composition for the production of Crofer 22 APU was determined [84]. The model batch compositions outperformed other commercial high Cr FSSs in scale adherence, growth rate, conductivity, and Cr volatility [84]. By finely tuning the oxygen active minor alloying constituents, it was found that low amounts of Mn, Ti, and La allowed for a controlled growth of the duplex chromia and manganese chromate scale [84]. The specific chemical composition chosen is given in weight and atomic percent in Table 2.1 [85].

Table 2.1: Chemical Composition of Crofer 22 APU.

	Fe	Cr	C	P	S	Mn	Ti	La	Si	Al
Weight %	73.20	24.00	0.03	0.05	0.02	0.80	0.20	0.20	0.50	0.50
Atomic %	71.18	25.07	0.14	0.09	0.03	0.79	0.23	0.08	0.97	1.01

2.1.2 Effect of Alloying Constituents and the Development of Crofer 22 APU

An evaluation of how the Cr and the micoalloying components affect the structure and properties of FSS has been performed in the following section. Key aspects of the processing conditions necessary to incorporate these additives have been considered. The effect of each chemical constituent on the performance of FSSs as an interconnect material has also been considered.

2.1.2 (a) Carbon

The addition of carbon to ferrite can increase the yield strength up to five times that of pure iron by increasing the activation energy necessary for slip [86]. The C occupies the $(00\frac{1}{2})$ octahedral position in the BCC lattice by slightly displacing the two nearest Fe atoms, at the top

and bottom of the octahedron, and causing tetragonal distortion [86]. Martensite, which has a body centered tetragonal structure (BCT), is formed when the C content is high enough and the high temperature phase, austenite, is quenched to prevent the precipitation of carbides [86]. The limit to carbon solubility in ferrite is 0.022 wt.% C and is found at the eutectoid temperature of 727 °C [87]. The equilibrium solubility decreases to 0.005 wt.% C at room temperature so FSSs are quenched to retain the ferritic structure [87]. Increasing the carbon content beyond the solubility limit may cause the formation of cementite in a pearlite microstructure, which would limit the high temperature properties of the FSS [88].

Argon-oxygen decarburization and vacuum melting is used to remove excess carbon during processing. The concentration of C and N can be reduced to levels of 0.015 wt.%, allowing greater amounts of substitutional alloying elements [89]. Several alloying elements such as Si, Mo, and Cr are known to expand the solubility limit of C in ferrite [89]. These elements are known as ferrite stabilizers.

A wide variety of steels and cast irons exploit the properties of ferrite. However, only a few commercial steels, such as Crofer 22 APU, are fully ferritic. The applicability of FSSs is limited by their mechanical properties. They do have a sufficient ductility, between 20 and 35%, and formability to be pressed into the complex shapes of an interconnect [89]. But, strain-hardening rates of ferrite are relatively low which reduce ductility and prevent strengthening by cold working [89]. Typical annealed yield and tensile strengths for ferritic stainless steels are 240 to 380 MPa and 415 to 585 MPa, respectively [89]. The yield strength and tensile strength of Crofer is 291 MPa and 439 MPa [85]. These values are at the low end for conventional FSSs.

A way to increase the yield and tensile strengths to 515 MPa and 655 MPa, would be to add refractory elements, as in superferritic steels [89].

2.1.2 (b) Niobium, Tungsten, and Silicon

Minor additions of refractory elements, Nb and/or W, were used to increase the hot tensile properties and creep resistance of model alloys with compositions based on Crofer 22 APU [90]. Additions of 2 wt.% W had no adverse effect on the oxidation behavior whereas addition of 1 wt.% Nb increased the growth rate of the oxide scale [90]. The adverse effects of Nb were alleviated with suitable additions of Si, which formed Si/Nb-rich Laves phase precipitates [90]. The Laves phase precipitates contributed to an increase in creep resistance and hot tensile strength [90]. The high-temperature electrical conductivity of the scales were slightly affected by Si additions up to 0.42 wt.% [90]. Cross-sectional SEM images through the oxidized surface of the Crofer-based substrate showed that SiO_2 formed below the chromia scale [90].

During prolonged oxidation of the commercial grade of Crofer 22 APU, which has a controlled amount of Si, there is no evidence of SiO_2 development below the scale. Since the interconnect must only support the weight of the SOFC stack under static loading, the composition of Crofer 22 APU is optimized for its oxidation performance rather than its mechanical properties. Therefore, Nb and W have not been added to Crofer 22 APU. Usually, minor additions of Si are used as an oxygen getter in the liquid steel prior to casting but the addition of Si in Crofer 22 APU seems to serve as a ferrite stabilizer by reacting with C to form SiC [91].

2.1.2 (c) Titanium

The addition of titanium to ferritic stainless steel alloys has been shown to benefit the high temperature characteristics of these alloys for use in SOFC interconnects. TiN precipitates can reduce the fractional softening of interconnects at high temperatures by preventing recrystallization and recovery of the cold-worked alloy [92]. TiN has a lower solubility in austenite than ferrite [92]. During solidification of molten steel, TiN precipitates in the austenitic region and is then annealed in the ferritic region [93]. During long term SOFC operation, titanium oxide can form and provide a keying effect at the interface of the alloy and chromia scale [94]. Titanium oxide can also form at the surface of the chromia scale to reduce chromium volatilization [9].

The complex multicomponent diffusion of Cr, Mn, and Ti is partly responsible for the excellent high-temperature oxidation resistance of Crofer 22 APU. Our observations demonstrate that there is a transfer of titanium from the initial TiN precipitates to the fine sub-scale TiO_x particles and to the chromia scale during oxidation at 800 °C. The formation of a primary titanium oxide phase on the scale surface is prevented due to the size of the TiN precipitates. The large precipitates have a small surface area to volume ratio, limiting dissolution and diffusion of titanium to the scale surface. The TiO_x phase forms instead, as sub-scale internal oxides on the dislocations formed during cold rolling, rather than on the grain boundaries [96]. This is significant because grain boundary titanium oxides could lead to spallation of the chromia scale [30].

2.1.2 (d) Lanthanum and Phosphorus

Minor additions of oxygen reactive elements such as the rare earths La, Y, and Ce have been shown to improve the adherence of chromia scales [80, 97]. The effects of these reactive elements are well known but the mechanisms by which the scale adherence is improved are not well understood [80]. There has not been a published study on effect of La in Crofer 22 APU on scale adherence. From the literature it is unclear whether La has an effect on the oxidation of Crofer 22 APU.

P is known to segregate to the alloy interface below the chromia scale and increase the oxidation rate [99, 100]. A proposed mechanism for the increased scale growth rate is that the P aids in the transport and annihilation of vacancies which move toward the alloy-scale interface and allows cation diffusion to become the dominant mode of oxidation [98]. The presence of P in the La/P-rich nodules found in Crofer 22 APU instead of in interstitial sites may slow the segregation of P to the surface.

2.1.2 (e) Chromium and Manganese

A minimum of 13 wt% Cr is required to maintain the BCC ferritic structure in the pure Fe-Cr system [101]. A lower Cr content enables the formation of the high temperature γ-phase, austenite upon heating as shown in Figure 2.2 [102]. FSSs require 17 wt% Cr to provide oxidation and corrosion resistance [103]. As an interconnect, Cr depletion occurs due to interaction with the contact paste. Thus, the critical Cr content should be higher, approximately 22 wt% [103]. However, application of an MCO coating allows a lower alloying content of Cr to be tolerated by reducing Cr volatilization. The upper limit is 26 wt% Cr due to CTE mismatch

between the FSS and the electrode materials [79]. The CTE of Crofer 22 APU ranges from 10.3 to 12.7 ppm/K from 250 to 1000 °C [85].

The Fe-Cr system is complicated by the presence of a miscibility gap at lower temperatures and the formation of several metastable phases at high temperatures. In the composition range from 20 to 30 wt% Cr a disordered solid solution exists with some tendency for chemical separation [104]. Embrittlement can occur with the formation of Fe-rich α_1 and Cr-rich α_2 phases at 475°C. SOFCs run at a higher temperature but the upper end of the miscibility gap is unclear at this point [104].

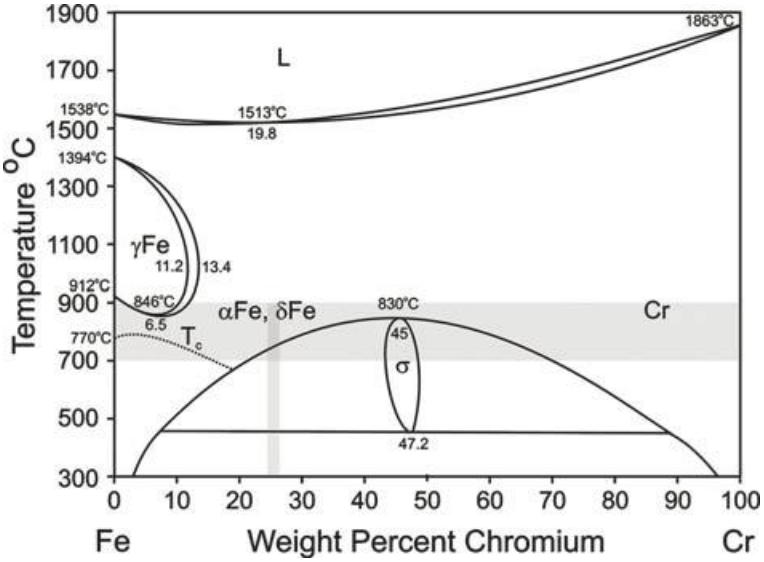

Figure 2.2: The Fe-Cr phase diagram with the shaded regions indicating the Cr content in Crofer 22 APU and the temperature range in which SOFCs operate [Reproduced from 102].

Higher Cr and Si contents increase the probability of forming a σ-phase along grain boundaries which causes embrittlement and leads to Cr depletion [102, 104]. The crystal structure of the σ-phase is tetragonal with the space group $P4_2/mnm$ with the lattice constants a = 0.8800 nm and c = 0.4544 nm [105]. Precipitation of the brittle σ-phase occurs at temperatures below 815 °C, which would have a detrimental effect on the oxidation properties of the interconnect during SOFC operation [106]. Several ferritic stainless steels that have been studied for interconnect applications exhibit the formation of σ-phase precipitates, although

Crofer 22 APU does not [102]. The internal stability and controlled surface oxidation of Crofer 22 APU make this alloy a promising candidate for interconnect applications.

The reactions that occur during oxidation at the surface of bare Crofer 22 APU are:

$$2\ Cr + {}^{2}/_{3}\ O_2 = {}^{1}/_{2}\ Cr_2O_3 \quad (1.12)$$

$$Mn + {}^{1}/_{2}\ O_2 = MnO \quad (1.13)$$

$$Cr_2O_3 + MnO = MnCr_2O_4 \quad (1.14)$$

A chromia scale forms first and then a $MnCr_2O_4$ scale forms with MnO as an intermediate step. The driving force for these reactions is the lowering of Gibbs free energy. The free energy of formation for reaction 1.12, 1.13, and 1.14 at 800 °C is -550 kJ/mol, -600 kJ/mol, and -40 kJ/mol, respectively [107]. Crystal field theory calculations have shown that Mn^{2+} has a higher mobility than Fe^{2+} and Cr^{3+} in chromia [108], which supports the mechanism of oxidation proposed by Stanislowski et al. whereby rapid transport of Mn^{2+} to the chromia scale surface leads to the formation of MnO which reacts with Cr_2O_3 to form $MnCr_2O_4$ [39].

Neal Magdefrau as part of the Aindow Research Group at the University of Connecticut has performed the first detailed microstructural and chemical analysis of the effect of the chemical constituents in Crofer 22 APU on the development of the duplex chromia and $MnCr_2O_4$ scale in SOFC simulated conditions [96]. Site selective specimen preparation with dual SEM/FIB has allowed the detailed analysis these phases in the TEM and such images are shown in Figure 2.3 [96]. The $MnCr_2O_4$ phase, indicated in regions 1 and 3, commonly forms polyhedral particles at the surface and less frequently forms pockets below the chromia scale [96]. The chromia scale, indicated in region 2, has a fine microstructure which completely covers the base

alloy [96]. Now that these phases have been identified in the TEM, SEM data of the surface oxides on Crofer 22 APU can be easily and correctly interpreted.

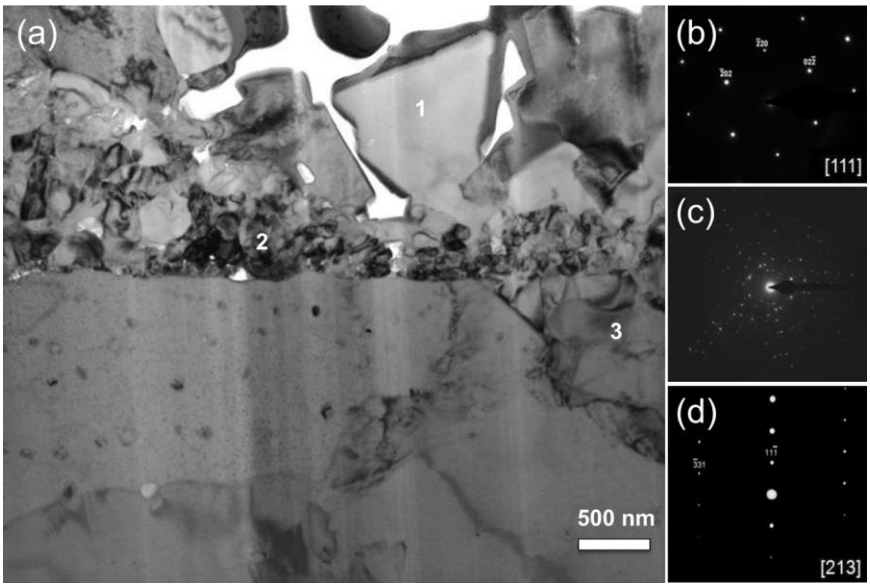

Figure 2.3: TEM data acquired from a FIB-cut cross section through the surface of a Crofer 22 APU sample oxidized for 750 h at 800 °C: (a) BF TEM image; (b), (c) and (d) SADPs from regions 1, 2 and 3 in (a), respectively. The single crystal zone axis patterns in (b) and (d) correspond to a cubic spinel phase whereas the spotty ring pattern in (c) is consistent with the corundum structure of Cr_2O_3 [Reproduced from 96].

The chemistry of the oxide phases that form across the surface of Crofer 22 APU are shown in Figure 2.4 [96]. The boundary of a ferrite grain is shown around the perimeter of the image [96]. The energy dispersive X-ray signal intensity from the Cr, Mn, and O maps along the ferrite grain boundary indicates that there is preferential formation of $MnCr_2O_4$ at these locations [96]. There are also polyhedral $MnCr_2O_4$ particles distributed evenly across the surface of the ferrite grain [96]. The Ti signal must be coming from the internal TiO_x particles because there was no Ti signal from cross-sectional EDXS analysis of the scale in the TEM on regions such as that shown in Figure 2.4 [96].

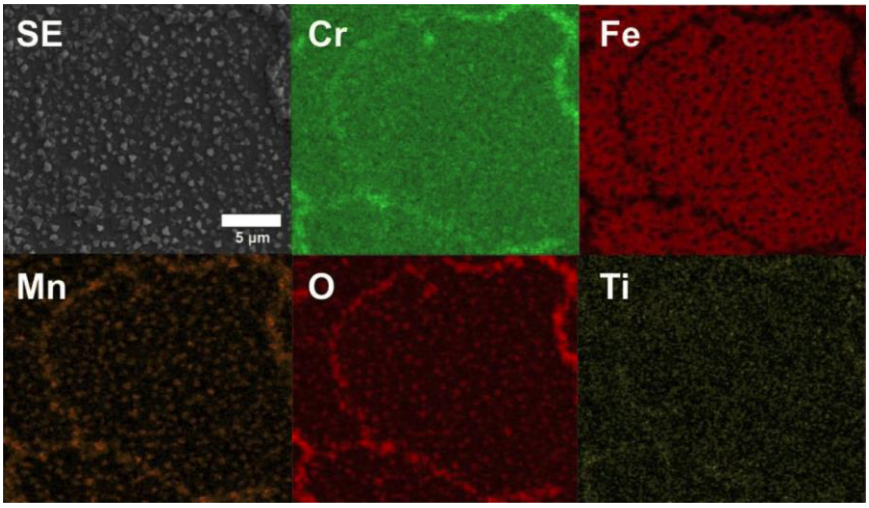

Figure 2.4. SEM data obtained from the surface of a Crofer 22 APU sample oxidized for 5 h at 800 °C. The SE image shows the region analyzed and the X-ray maps show relative intensities proportional to the local composition of each element from quantitative analysis of EDXS data at each pixel [Reproduced from 96].

The surface of the Crofer 22 APU sheets must have a high defect density due to the cold rolling process which was necessary to form the sheet metal. After heating to 800 °C there is recrystallization and the accumulation of fine ferrite grains in the surface region of the alloy [96]. With smaller ferrite grains at the surface, there are a high density of grain boundaries from which rapid ion transport can occur during oxidation. Magdefrau et al. have shown that a pre-oxidation heat treatment of Crofer 22 APU in Ar at 1050 °C can reduce the parabolic oxidation rate of the alloy by two times [96]. In this process, the grain boundary density at the surface is reduced as the average ferrite grain size increases from 15.9 μm in the as-received sample to 248.6 μm in the Ar-treated sample [96]. Therefore, the regions in which there is rapid transport of ions during oxidation are reduced and thus, the propensity for spallation, described in Section 2.2.1, is decreased [96]. Another effect that the pre-oxidation heat treatment has is that with a lower grain boundary density, the coverage of $MnCr_2O_4$ across the chromia scale is increased, which can lower Cr volatilization [96].

2.2 Chromia

2.2.1 Spallation

Although the growth rate of chromia scales in FSS is rather slow, there are problems with buckling and spallation. Concurrent diffusion of O and Cr along the grain boundaries leads to oxide growth within the scale. The increase in volume along the grain boundaries leads to internal stresses which cause the scale to buckle and spall.

The tendency for chromia scales to buckle can be described by the Pilling-Bedworth ratio in Equation 1.15.

$$\mathrm{P-B\ Ratio} = \frac{A_O \rho_M}{a \rho_O A_M} \tag{1.15}$$

Where A_O is the molecular weight of the oxide, ρ_O is the density of the oxide, A_M is the atomic weight of the metal, ρ_O is the density of the metal, and a is the coefficient for the metal species for the overall oxidation reaction described in Equation 1.16.

$$aM + \frac{b}{2} O_2 \rightarrow M_a O_b \tag{1.16}$$

The volume per Cr ion in chromia is over twice as large as the volume per Cr ion in Crofer 22 APU as calculated in Equation 1.17.

$$\mathrm{P-B\ Ratio} = \frac{\left(\left(2*51.996\frac{g}{mol}\right)+\left(5*15.999\frac{g}{mol}\right)\right)*7.7\frac{g}{cm^3}}{2*5.23\frac{g}{cm^3}*\left(\left(0.23*51.996\frac{g}{mol}\right)+\left(0.88*55.845\frac{g}{mol}\right)\right)} = 2.21 \tag{1.17}$$

The ideal P-B ratio is unity. Generally, the compressive stress in oxides with a P-B ratio up to 2 can be tolerated. However, the compressive stress which develops in chromia on Crofer 22 APU is too large causing buckling and eventually spallation.

In SOFC operation, cycling accelerates chromia scale spallation by introducing interfacial shear stresses due to thermal expansion mismatch. The CTE of Crofer 22 APU is ≈12 ppm/K while that of chromia is an average of 6.5 ppm/K and varies depending on the impurity content [85, 109]. The stress that develops can be estimated by Equation 1.18 [109].

$$\sigma = \frac{\Delta a \Delta T E}{1-\nu} \tag{1.18}$$

Where Δa is the difference in the scale and substrate CTE, ΔT is the SOFC operation temperature, E is the elastic modulus of chromia, and ν is the Poisson ratio of the scale. The stress that develops for chromia on Crofer 22 APU is calculated in Equation 1.19 [109].

$$\sigma = \frac{(12-6.5)\frac{ppm}{K} * 1073K * 230GPa}{1-0.25} = 1.81\ GPa \tag{1.19}$$

The thickness and growth mechanism must be taken into account for an accurate estimation of the shear stress that develops, described in Section 2.2.4.

2.2.2 Crystal Structure

The scale responsible for the high temperature properties of FSS is associated with the mineral eskolaite [110]. The scale is more commonly known as α-Cr_2O_3 and is a rhombohedral oxide with a corundum structure which has the $R\bar{3}c$ space group [111]. The corundum structure consists of an hcp array of oxygen with two-thirds of the octahedral sites occupied by chromium [111]. As shown in Figure 2.5, there is a layer of vacancies positioned at every third octahedral site. The vacancies are considered

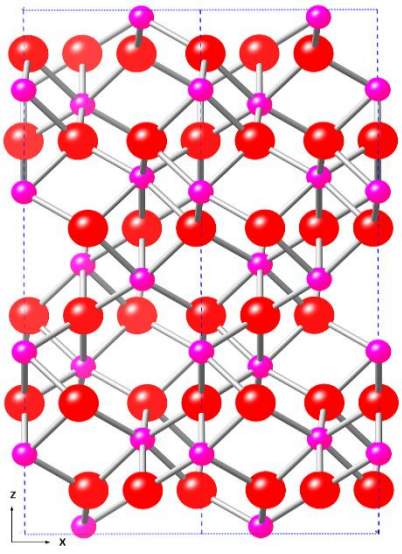

Figure 2.5: The pattern of empty and occupied octahedral sites in the corundum structure viewed along the [010] direction. The smaller and larger ions indicate Cr and O, respectively [Reproduced from Crystal Maker].

interstitial sites which take part in the transport of ions through the chromia lattice [111].

The formation of chromia scales has been understood through studies of the electronic conductivity and the diffusion of tracer ions as a function of temperature and pressure in chromia ceramics.

2.2.3 Electrical Conductivity

Holt and Kofstad have studied and reviewed the conductivity and defect structure of chromia and concluded that chromia behaves as an intrinsic semiconductor at temperatures above 1000 °C and an extrinsic semiconductor at temperatures below 1000 °C [112, 113].

Values for the band gap in chromia have been reported to be between 2.4 eV and 7.0 eV [114]. This wide range of reported values may be due differences in impurity levels in the chromia and various atmospheres used in the measurement. Young et al. have suggested that chromia is an n-type conductor at low oxygen activities and a p-type conductor near atmospheric pressure [114]. At the temperatures in which SOFCs operate the effects from impurities dominate making chromia an extrinsic semiconductor [115].

Ti may have an effect on the defect structure of the chromia scale formed on Crofer 22 APU due to the presence of TiO_x precipitates below the scale [96]. For each Cr^{3+} ion replaced by a Ti^{4+} ion, the compensating electronic and point defects formed comprise of electrons and Cr^{3+} vacancies. In terms of Kr*ö*ger-Vink notation, electroneutrality is given by Equation 1.20 [116].

$$[Ti_{Cr}^{\cdot\cdot}] = n + [V_{Cr}^{3'}] \qquad (1.20)$$

$Ti_{Cr}^{\cdot}$ designates the occupation of a Cr site with an effective charge of +1, $V_{Cr}^{3'}$ designates a vacancy at a Cr site with an effective charge of -3, and n designates the concentration of electrons.

The solubility of Ti and the concentration of electrons is expected to increase with decreasing oxygen activity and elicit n-type conductivity [116, 117]. The magnitude of the conductivity would not be affected by the anode environment of a SOFC due to limited solubility of hydrogen in chromia. As in Figure 2.6, the electrical conductivity of the specimens does not change with the partial pressure of H_2 [117]. Otherwise, the holes produced by dissolution of hydrogen would cancel the electron produced by the dissolution of Ti [117]. With higher oxygen activities a p-type conductivity is observed because Ti^{4+} substitution is accommodated by Cr vacancies instead of electrons. The defect structure has significant consequences on the ionic transport properties and results in different oxidations mechanisms in the cathode and anode environment of SOFCs [118].

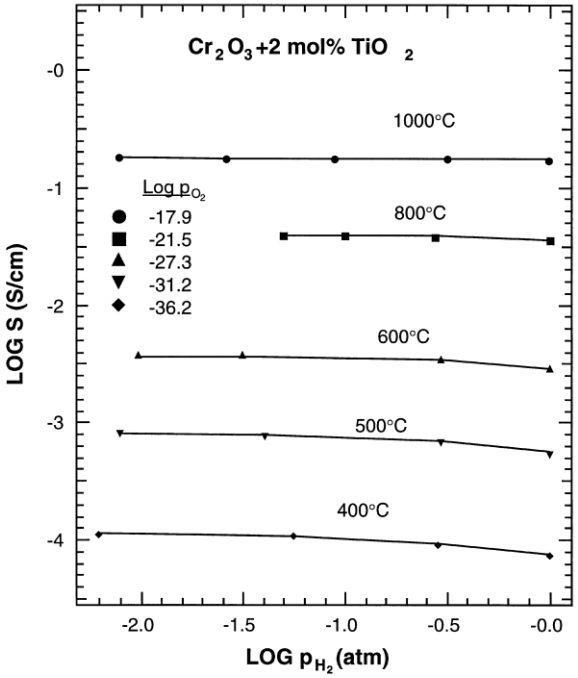

Figure 2.6: The electrical conductivity of the Cr_2O_3 + 2 mol% TiO_2 specimen as a function of the hydrogen at constant oxygen activities at temperatures from 400 °C to 1000 °C [Reproduced from 116].

There are mixed reports on the conductivity mechanism in chromia as to whether the charge carrier is localized to a metal site or delocalized in the conduction band [116, 119, 120]. At lower temperatures, electrons and holes can lower their energy by forming polarons in

polarizable solids. The concept of a polaron was set forth by Landau in 1933 [121, 122]. A polaron is a charge, electron or hole, which sits in a potential well from the ionic displacements it created. The polaron mechanism is described as 'small' because the size of the potential well fits inside one unit cell.

Iordanova et al. have considered the charge transport through the crystal lattice of chromia to be localized for their *ab initio* electronic structure calculations [120]. They have compared values for the electronic coupling with previous work on hematite and found that chromia is more ionic in nature due to a smaller overlap between the donor-acceptor sites [120]. They have shown that the mobility of holes in chromia along the (001) basal plane is 3 orders of magnitude faster than the mobility of electrons [120]. This is because the distance between Cr^{2+} and Cr^{3+} is greater than the distance between Cr^{4+} and Cr^{3+}. The larger ionic radius of Cr^{2+} compared to Cr^{4+} creates a greater polarization which decreases orbital overlap and requires a greater activation energy necessary for charge transfer [120].

2.2.4 **Chromia Scale Growth**

The high Cr content in Crofer 22 APU results in a short transient oxidation period with minimal oxidation of the base metal [123]. Therefore, steady state oxidation is the dominant mechanism in chromia scale growth and can be described by a parabolic rate expression based on weight gain.

Wagner's theory of oxidation can be used to calculate the growth rate of the chromia scale. Firstly, a simple measurement of the weight gain, w, over time, t, across area, A, due to the diffusion of oxygen can elicit a value for the gravimetric rate constant, k_g.

$$(\frac{w}{A})^2 = k_g t \tag{1.21}$$

Secondly, this rate constant can be substituted for the parabolic rate constant (k_p) for Wagner's theory for the oxidation of metals to solve for the diffusivity of the ions based on the defect structure [124].

$$k_p = \frac{c_0}{2b}\int_{P'O_2}^{P''O_2}(\frac{3}{2}D_{Cr} + D_O)d\ln P_{O_2} \tag{1.22}$$

Where D_{Cr} and D_O are the self-diffusion coefficients for Cr and O in Cr_2O_3; c_0 and b are constants; and $P'O_2$ and $P''O_2$ are the oxygen partial pressures at the atmosphere/oxide scale interface and the oxide scale/alloy interface, respectively.

At 800 °C and a PO_2 = 0.1 atm, the diffusion coefficient of Cr and O along the grain boundaries in a chromia scale is $1.1x10^{-12}$ and $5.9x10^{-13}$ cm^2s^{-1}, respectively [125]. At the same conditions, these values are significantly higher than the bulk diffusion of Cr and O, which are $5.9x10^{-18}$ and $2.6x10^{-18}$ cm^2s^{-1}, respectively [125]. With these diffusivity values and the high density of grain boundaries in chromia scales, outward grain boundary diffusion of Cr is the dominant mechanism of oxidation.

Depending on the partial pressure and impurities within the alloy and scale, these diffusion coefficient values for Cr and O can vary up to 5 orders of magnitude [125]. Therefore, the oxidation rate for chromia-forming interconnect alloys is different in the anode and cathode environment [126, 127, 128, 129]. The average oxide thickness formed on Crofer 22 APU exposed at 900 °C for 2000 h in dry air, air + 0.1 H_2O, and $Ar/H_2/H_2O$ were 8, 13.5, and 20 μm, respectively [102]. The increased oxidation rate in the moist air and hydrogen based forming gas is due to inward OH^- diffusion [130]. 2 mol H_2O can react with the outer part of the scale

whereby, 2 mol of OH^- diffuse inward to the scale/alloy interface and 1 mol H_2 (g) release to the atmosphere. OH^- diffuses through chromia more rapidly than O^{2-} due its smaller ionic radius (OH^- ionic radius = 0. 95 Å and O^{2-} ionic radius = 1.40 Å) [130]. Once OH^- reacts with the metal ions at the alloy interface, H_2 (g) is formed which penetrates through the substrate and can cause embrittlement [131]. Although the moist atmospheres result in an increased oxidation rate they can have a beneficial effect on increasing the density and adherence of the scale [132].

2.3 Spinel

2.3.1 Spinel Crystal Structure

The structural parameters of the MCO protective coating change during SOFC operation due the addition of Cr, Fe, and Ni cations from either Fe- or Ni-based chromia-forming interconnect alloys [71]. Substitution of these cations into the MCO spinel lattice results in a reaction layer with different properties than the starting coating composition. The crystal structure of spinel can be used to explain how a variation in composition will result in a property change which is important to understand the degradation of MCO protective coatings.

The crystal structure of spinel was determined independently by Bragg and Nishikawa [133, 134]. The Bravais lattice for the majority of spinel compounds is cF. This non-primitive cell is chosen for the cubic crystal system to conveniently describe the position of atoms in the structure. The motif is shown in Figure 2.7 and consists of two AB_2O_4 formula units and makes up a total of 56 atoms in the cell with face centering [135]. MCO is known to have a normal

spinel structure in which the tetrahedral (A) sublattice is filled with divalent cations and the octahedral (B) sublattice is filled with trivalent cations.

MCO is complicated by the co-existence of a cubic and tetragonal spinel phases at room temperature [72]. However, at temperatures in which SOFCs operate, MCO is single phase cubic [72]. Also, Cr stabilizes the cubic phase, so the RL that develops between chromia forming interconnects and MCO coatings is single phase cubic [136]. Therefore, the symmetry of the cubic phase will be considered first.

The conventional choices for the cubic unit cell origin are on an A site cation, which yields a $\bar{4}$3m point symmetry, or on an octahedral site vacancy, which yields an m$\bar{3}$m point symmetry [135]. The point symmetry shown in Figure 2.7 is of $\bar{4}$3m [135]. The crystallographic point group describes the atomic sites which have translational periodicity matching the Bravais lattice. The point group, $\bar{4}$3m, has a 4-fold rotation and inversion perpendicular to the x-axis, 3-fold rotation perpendicular to the y-axis, and a mirror plane perpendicular to the z-axis. The combination of these symmetry elements will create new symmetry elements that are consistent with operations stated. Once this motif is in position with its characteristic point group symmetry, the overall space group, d$\bar{3}$m, can be generated. The d$\bar{3}$m space group is non-symmorphic, meaning that there has been a replacement in the set with a screw axis, glide plane or both. The replacement here is a diamond glide plane, "d," in which an example of the translation is shown in Figure 2.8 with the simplest motif for the d$\bar{3}$m space group. The diamond glide plane can be seen as it translates the center of the tetrahedron from ($^1/_4$,$^1/_4$,$^3/_4$) to ($^3/_4$,$^1/_4$,$^1/_4$). The same translation, which is parallel to the face diagonal, can be applied to the white and shaded octants and result in the spinel structure.

The tetrahedrally coordinated cations are located at the 8a positions and form a diamond cubic sublattice, shown in Figure 2.8, with a repeat unit equal to the lattice parameter. The octahedrally coordinated cations are located at the 16d positions. The overall cation sublattice has the same structure as the $MgCu_2$ C15 Laves phase [137, 138]. The repeat unit of the anion sublattice is the same in each octant as shown in Figure 2.7 [135].

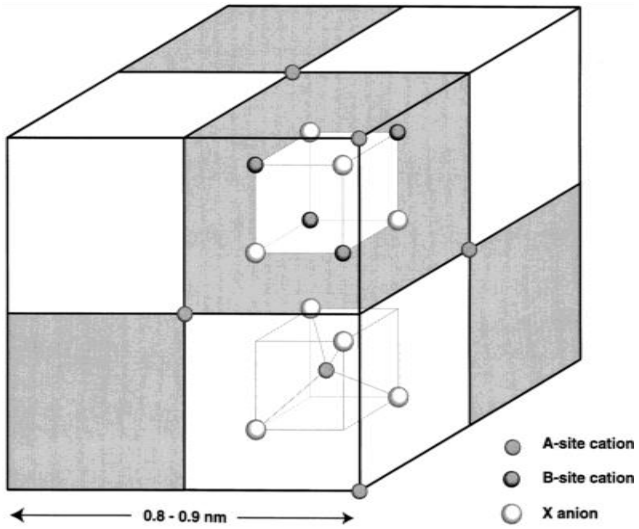

Figure 2.7: The spinel unit cell is made up of a motif of two octants which are translated along the diamond glide plane and repeat with the pattern indicated by the shading in the other octants. Atom positions are shown for the motif only. One A-site in the motif is not visible in the drawing; it is on the center of the base of the cubic unit cell. [Reproduced from 135].

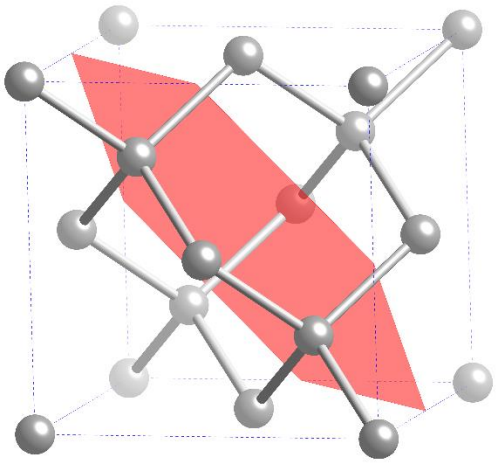

Figure 2.8: Diamond cubic structure illustrating a simple basis of a tetrahedron and the diamond glide plane which translates the basis [Reproduced from Crystal Maker].

The anion sublattice forms a pseudo-cubic close-packed (CCP) arrangement, in which the distortion of the anions from their ideal CCP positions is described by the oxygen deviation parameter, $u^{4\bar{3}m}$ [135]. The anions are displaced in the direction of the body diagonal as shown in Figure 2.9 [135]. The degree of distortion of the anion lattice is based on the size of the

cations distributed on the A and B sites. There is a simple relationship in the oxygen deviation parameter when considering the origin reference point for the spinel unit cell to be either $4\bar{3}m$ or $\bar{3}m$ [135].

$$u^{4\bar{3}m} = u^{\bar{3}m} + \frac{1}{8} \tag{1.23}$$

The ideal CCP anion arrangement corresponds to $u^{\bar{3}m} = 0.25$ [135].

The tetragonal unit cell is described by the Bravais lattice *tI*. The body centered tetragonal (BCT) unit cell is related to the face centered (FCC) unit cell by $a_{tetragonal} = b_{tetragonal} = a_{cubic}/\sqrt{2} = b_{cubic}/\sqrt{2}$ [141]. The tetragonal spinel phase, with the space group $I4_1md$, has half the number of atoms as the cubic spinel phase with the space group, $Fd\bar{3}m$. Thus, a direct comparison can be made between half of the cubic unit cell volume and the tetragonal unit cell volume. Comparing the two phases in MCO, $MnCo_2O_4$ ($a^3/2$ = 286 Å^3) and Mn_2CoO_4 (a^2c = 301 Å^3), the tetragonal phase occupies a larger volume per atom than the cubic phase due to lattice distortion in the c-direction by Jahn-Teller effect of Mn substitution on the B sublattice [141].

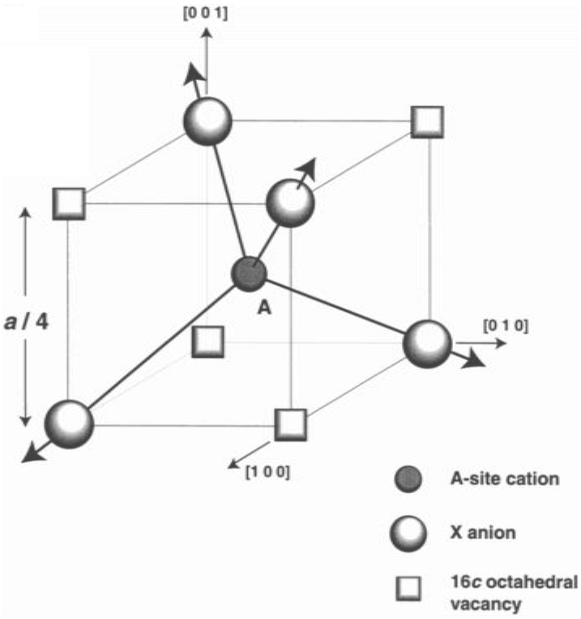

Figure 2.9: Schematic drawings of lattice surroundings and nearest neighbors for (a) the tetrahedral A-site (8a), **[**Reproduced from 135].

2.3.2 Phase Separation

2.3.2 (a) MCO Spinel

The lattice parameter of the cubic phase is shown to increase with Mn substitution from $Mn_{0.07}Co_{2.93}O_4$ to $Mn_{1.22}Co_{1.78}O_4$ in Figure 2.10 [142]. The lattice parameter across the single phase cubic region ranges from a = 8.107 Å for $Mn_{0.07}Co_{2.93}O_4$ [143] to a = 8.318 Å for $Mn_{1.22}Co_{1.78}O_4$ [142]. The sintering process, conventional or spark plasma sintering, has little effect on the crystal cell parameter values [142].

With further Mn substitution, a two phase equilibrium exists at room temperature. A tetragonal phase of high Mn content forms and a cubic phase of high Co content forms. Co-refined structural parameters from X-ray and neutron diffraction data have indicated that the two phase spinel mixture, when x = 1.5 in $Mn_{3-x}Co_xO_4$, consists of 40 % $Mn_2Co_1O_4$ and 60 % $Mn_{1.66}Co_{1.34}O_4$ [141]. Overlap of the characteristic X-ray reflections in these two phases has led to an obvious inaccurate measurement in the mass fraction, indicating a greater content of Mn than the average composition of the precursors used to prepare the powder sample. Thus, there has yet to be a reliable published study on the composition and distribution of the equilibrium phases formed upon cooling MCO ceramics from sintering temperatures.

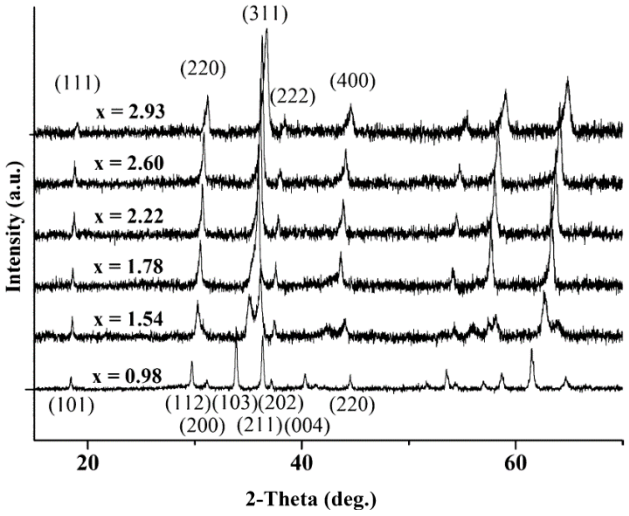

Figure 2.10: XRD patterns for the $Mn_{3-x}Co_xO_4$ 0.98 < x < 2.93 ceramics. As Co substitutes in the A site for Mn there is a tetragonal to cubic transition and then a decrease in lattice parameter. Reproduced

Activity calculations by Aukrust and Muan have shown at sintering temperatures, MCO spinel is single phase cubic and that at lower temperature two phases can exist in equilibrium [72]. Based on the phase diagram presented by Aukrust and Muan, annealing at 650 °C may give a more accurate evaluation of the segregation effects in MCO spinel. The phase segregation effects are correlated to the cation site preference of the Mn and Co cations.

2.3.2 (b) Cr- and Fe-Substituted MCO Spinel

In $Mn_xCo_1Cr_{2-x}O_4$, the tetragonal/cubic phase region extends from x = 1.1 to 1.2 and in $Mn_xCo_1Fe_{2-x}O_4$, extends from x = 1.25 to 1.55 at 950°C [150]. The high temperature spinel phase field for Cr substituted MCO is limited to thin region connecting the cubic compounds $MnCr_2O_4$ and $CoCr_2O_4$ while deviation from this region would cause either the formation of Cr_2O_3 or (Mn,Co)O [77]. Higher Fe contents increase the susceptibility for FeO formation which limits the use of Fe_3O_4 for high temperature applications. The segregation of tetragonal and cubic spinel phases is due to the tendency of Mn^{3+} to cluster and form domains [151].

2.3.3 Conditions for Stability

2.3.3 (a) Electroneutrality

For the spinel structure to be stable, the conditions for electroneutrality must be met. For electroneutrality, the combined charge of cations must equal the combined charge of the anions. There are several types of spinels which satisfy the electroneutrality condition with cations having a different oxidation state, such as 0-3, 1-3, 2-3, 4-2, 2-5, and 6-1 [152]. MCO is

known to be of the 2-3 normal spinel type because the oxidation state of the cations on the A sublattice are mainly divalent and the cations on the B sublattice are mainly trivalent.

2.3.3 (b) Gibbs Energy Minimum

The equilibrium distribution of the cation species across the A and B sublattice is reached at a Gibb's energy minimum. The stability of the cations in the A and B sublattices depends on the internal energy (U), pressure-volume (PV) contribution, and temperature-entropy (TS) contribution.

$$G = H - TS = U + PV - TS \quad (1.24)$$

U is comprised of the electrostatic energy, U_E, the Born repulsion energy, U_B, and the crystal field stabilization energy, U_e.

$$U = U_E + U_B + U_e \quad (1.25)$$

2.3.3 (c) Coulomb Energy

The largest contribution to G, is from the Coulomb energy, U_E. U_E can be obtained from the heat of vaporization of a crystal plus the energy necessary to separate the vapor molecules. In Equation 1.23, the oxygen parameter is buried in terms of the Madelung constant, M [153].

$$U_E = \frac{Ne^2M}{4\pi\varepsilon_0 a} \quad (1.26)$$

e is the charge of an electron, N is the moles of ion pairs, ε_0 is the vacuum permittivity, and a is the lattice parameter. Thus, the oxygen parameter is related to the average charges of the cations in the A and B sublattice using Equation 1.24 which was developed by Thompson and Grimes [154].

$$M = \alpha_1 Q_A^2 + \alpha_2 Q_A Q_B + \alpha_3 Q_B^2 + \alpha_4 Q_A Q_O + \alpha_5 Q_b Q_O + \alpha_6 Q_O^2 \qquad (1.27)$$

Q_A, Q_B, and Q_O are the average charges on the A, B, and O sites; α_1, α_2, and α_3 are constants; and α_4, α_5, and α_6 are functions of the oxygen parameter. This relationship between the oxygen parameter, $u^{\bar{3}m}$, and the Madelung constant has been plotted by O'Neil and Navrotsky and is shown in Figure 2.11 [140]. When the oxygen parameter is below 2.555, a 2-3 normal spinel is favored and above 2.555 a 2-3 inverse spinel is favored [153]. Higher values of M correspond to the more stable spinel type by leading to a more negative Coulomb energy.

For Cr and Ni substituted spinels, $u^{\bar{3}m}$ is between 0.259 and 0.262 [136]. The Fe substituted spinels have a lower range of $u^{\bar{3}m}$ values between 0.256 and 0.259 [150]. The large Fe^{3+} cations on the B site, increase the size of the octahedra, and therefore displace the oxygen ions along the body diagonal towards the ideal CCP position of 0.25. A comprehensive study on the range of $u^{\bar{3}m}$ values verse cation distributions confirm that these spinel compounds have mixed valency across the A and B sites [135].

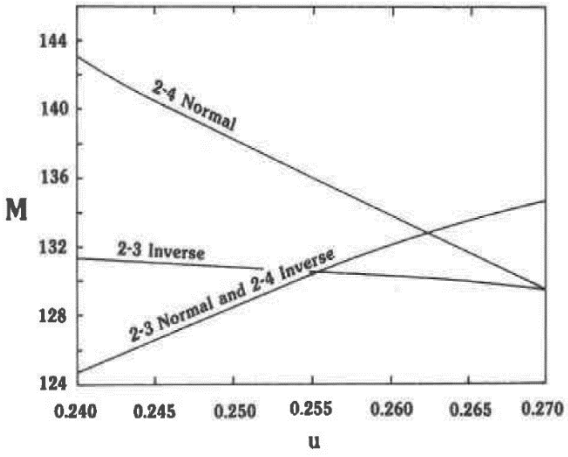

Figure 2.11: Madelung constant (M) versus the crystallographic oxygen parameter $u^{\bar{3}m}$ for normal and inverse 2-3 spinels and normal 2-4 spinels. Inverse 2-4 spinels have the same charge distribution and therefore the same Madelung constant as normal 2-3 spinels. [Reproduced from O'Neil].

2.3.3 (d) Born Repulsion Energy

The simplified expression for the Born repulsion energy is:

$$U_B = \frac{NB}{r^n} \qquad (1.28)$$

Where N is the moles of ion pairs, B is a constant, and r^n is the distance between the ion pairs in which the power, n, can be between 6 and 12. A full representation of this expression is given by Pollert [152].

2.3.3 (e) Crystal Field Stabilization Energy

U_e can be a significant factor in deciding the stable cation distribution for transition metal spinels. When cations from the d-group are inserted into the crystal field their orbitals are split in order to lower the degeneracy. The magnitude of splitting is given by the crystal field splitting parameter, Dq, which is determined from the FTIR absorption spectrum with the aid of crystal field theory (CFT) [155]. Splitting in the tetrahedral field results in t_{2g} and e_g orbitals of high and low energy, respectively [156]. Splitting in the octahedral field also results in t_{2g} and e_g orbitals, but their order is reversed with low and high energy, respectively [156]. When the crystal field is less than the correlation effect, Hund's rule is preserved and the cation takes the high spin state, as for Mn^{3+}, and can lead to the distortion along the prolate axis described in Section 2.3.6 [152]. A stronger crystal field results in a low spin state as for Co^{3+} ($3d^6$) and Ni^{3+} ($3d^7$) and can distort the crystal along the oblate axis [152].

The CFSE is the stability that results from putting electrons in the lower energy orbitals which arose from the splitting of the d-orbitals. The difference between the CFSE for a cation in the octahedral and tetrahedral coordination is known as the octahedral site preference energy (OSPE) [157]. The OSPE can be used to calculate the inversion parameter for simple binary spinels [157]. However, when the OSPE for both cations in the binary spinel are small, the Madelung energy is necessary to calculate the site occupancy [158].

2.3.3 (f) Elastic Energy

Considering the PV contribution, the cations must be of adequate size to fill the relevant holes for spinel generated by the FCC anion lattice. With the hard sphere model using 1.40 Å as the anionic radius, the radius of the tetrahedral and octahedral holes is 0.31 Å and 0.58 Å, respectively [152]. The FCC structure is distorted when cations of a different size fill the interstitial sites. The ionic radius of the cations relevant to MCO protective coatings and the RLs that form are given in Table 2.3. Correspondingly, the formulae necessary to calculate the volume of the spinel structure based on the cationic radii and composition are given in Section 2.3.5. Considering the radius ratio rule, all of these cation combinations satisfy the constraint of .732 $\geq r_c/r_a \geq$ .414 and could result in a stable structure [159].

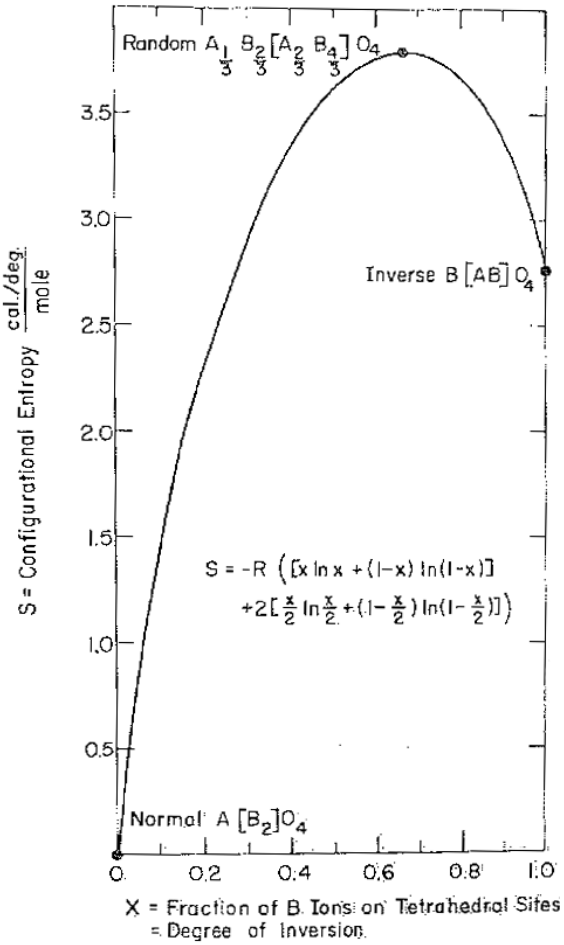

Figure 2.12: The dependence of the configurational entropy in spinels on the degree of inversion [Reproduced from 160].

2.3.3 (g) Configurational Entropy

The TS factor contributes to the disorder of cations from the equilibrium cation distribution. Navrotsky and Kleppa have shown that the temperature dependence of disorder relies solely on the configurational entropy [160]. This is the entropy assigned to the exchange of cations

between the tetrahedral and octahedral sites. The standard thermodynamic assessment of configurational entropy, S_C, assuming a completely random mixing of ions is given by:

$$S_C = -R \sum b^s N_i^s \ln N_i^s \qquad (1.29)$$

where N_i^s is the fraction of species i in site s, and b^s is the number of s sites per formula unit [160]. For the formula unit AB_2O_4, this may be evaluated as:

$$S_C = -R[x \ln x + (1-x)\ln(1-x) + xln\left(\frac{x}{2}\right) + (2-x)\ln\left(1-\frac{x}{2}\right)] \qquad (1.30)$$

where x is the inversion parameter [140]. The variation of the configurational entropy for a simple binary spinel is shown in Figure 2.12 [160].

2.3.3 (h) Interchange Enthalpy

For a normal spinel the exchange of cations from their equilibrium sites is given by the reaction:

$$A + [B] \rightarrow [A] + B \qquad (1.31)$$

where the cations in the octahedral site are bracketed [140]. Considering the entropy released from the disorder of a normal spinel, the reaction involving one divalent A cation from the tetrahedral sublattice and two trivalent B cations from the octahedral sublattice is shown in Equation 1.32.

$$A_{1-x}B_x[A_xB_{2-x}]O_4 \qquad (1.32)$$

At high temperatures the thermal energy acts against the internal energy and the PV contributions. In doing so, the value of the disorder/inversion parameter, x, will increase starting from a normal spinel and decrease starting from an inverse spinel.

The change in free energy on disordering is given by:

$$\Delta G = \Delta U - T\Delta S + P\Delta V \qquad (1.33)$$

where ΔS is comprised of the configurational and non-configurational entropy and ΔV is sufficiently small enough to ignore [160].

Under equilibrium conditions, $\Delta G = 0$, the interchange enthalpy can be simply represented as:

$$\Delta H = \Delta U = T\Delta S_C \qquad (1.34)$$

where ΔS_C is the configurational entropy [160].

At equilibrium the rate of change in the free energy with disorder parameter is zero. This condition is represented by Equation 1.35 [140].

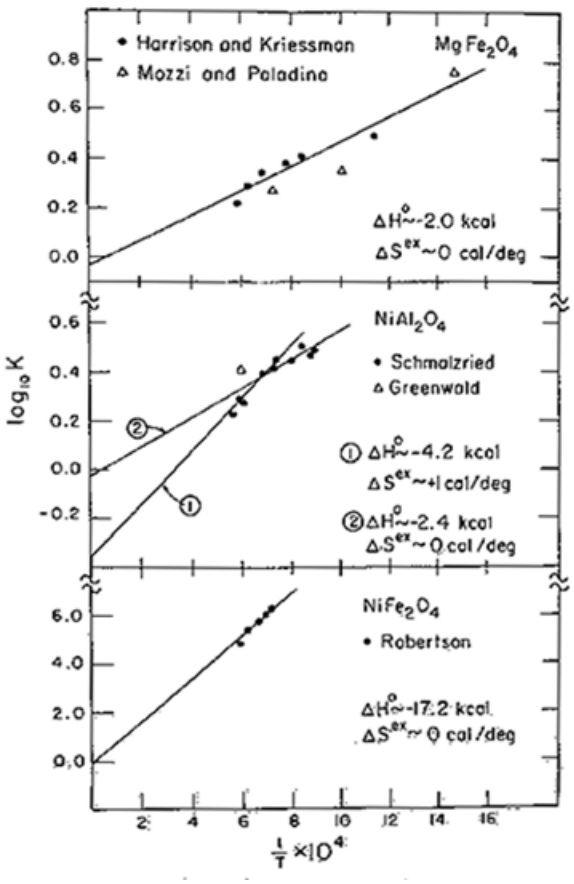

Figure 2.13: Three examples which show the calculation of the interchange enthalpy ΔH^0 from the slope and that the non-configurational entropy $\Delta S^0 = 0$ [Reproduced from 160].

$$\frac{\partial \Delta G}{\partial x} = 0 \qquad (1.35)$$

Combining Equations 1.33 and 1.34 and carrying out the differentiation given in Equation 1.35 gives the equilibrium constant, K [140].

$$K = \frac{[A]B}{A[B]} = \frac{x^2}{(1-x)(2-x)} \qquad (1.36)$$

Measurements of inversion parameter, x, as a function of temperature have been compiled by Navrotsky and Kleepa [160]. A linear fit to this data provides the interchange enthalpy, ΔH, from the slope and demonstrates by the location of the y-intercept that the non-configurational

entropy, ΔS_D, equals zero [160]. In Figure 2.13, three plots of this this data are shown which convey this trend [160].

2.3.3 (i) Site Preference Energy

Navrosky and Kleppa have found a way to distinguish the enthalpy released from an individual cation from the enthalpy released in the interchange of cation pairs over the A and B sublattice [160]. They start with the enthalpy released in the conversion of γ-Al_2O_3 to α-Al_2O_3 which is due to just Al ion transfer from an A site to a B site [160]. In the structural transformation of alumina, there is an exchange of 0.25 mol Al^{2+} in the A sublattice to Al^{3+} in the B sublattice [160]. In this reaction 10.6 kcal/mol is released and is considered as the octahedral site preference energy (OSPE) [160]. They then calculate the interchange enthalpy of several binary spinel aluminates and use the OSPE of Al^{3+} in each case to calculate the individual OSPE of the other cations [160]. An example of this calculation is given for $MgAl_2O_4$, where the 10% of the Mg^{2+} on the A sublattice exchange with Al^{3+} on the B sublattice and release 0.9 Kcal of energy [160]. Therefore,

$$\Delta H = -0.9 \text{ kcal}/0.1 \text{ mol} = -9 \text{ kcal/mol} \quad (1.37)$$

$$\text{OSPE } Mg^{2+} = \Delta H - \text{OSPE } Al^{3+} \quad (1.38)$$

$$-9 \text{ kcal/mol} - (-10.6 \text{ kcal/mol } Al^{3+}) = 1.6 \text{ kcal/mol } Mg^{2+} \quad (1.39)$$

By thermodynamic convention an exothermic reaction is given a negative sign. The OSPE for Al^{3+} is negative because energy is released when occupying the B sublattice and the OSPE for Mg^{2+} is positive because it takes energy to occupy the A sublattice [160]. This OSPE for Mg^{2+} and many others can be read off the diagram in Figure 2.14 [160].

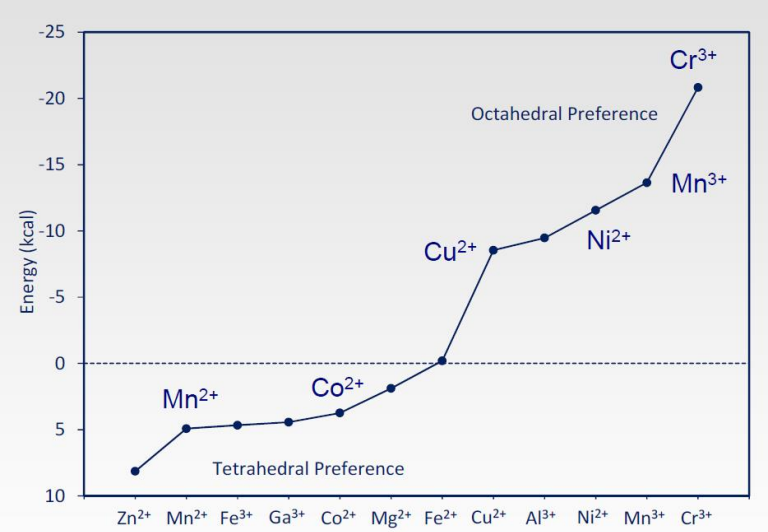

Figure 2.14: Empirical site preference energies for some divalent and trivalent cations in the spinel structure [Reproduced from

For the chemical species relevant to MCO protective coatings and the RLs that form, Cr^{3+} has the most negative OSPE followed by Mn^{2+} and Ni^{2+} [160]. The positive OSPEs for Mn^{2+} and Co^{2+} indicate that these ions prefer the A sublattice [160]. The OSPE for Fe^{2+} is roughly zero while the OSPE for Fe^{3+} is positive which explains why Fe_3O_4 is an inverse spinel [160].

2.3.4 Cation Site Occupancy in Spinel

With this description of the parameters which affect the cation site occupancy in spinel, an overview of several studies which measure the cation site occupancy in MCO protective coatings and the RLs that form are given.

2.3.4 (a) Manganese Cobaltite

With Co substitution in the binary spinel, $Mn_{3-x}Co_xO_4$, for x = 0 to 1, Mn^{2+} is progressively replaced by Co^{2+} on the A sublattice [73]. When x = 1 the crystallochemical formula is $(Co^{2+})_A(Mn^{3+}{}_2)_BO_4$ [73]. Further addition of Co goes into the B site as Co^{2+} and Co^{III} by replacing Mn^{3+} and partially oxidizing Mn^{3+} to Mn^{4+} [73]. The trend of Co substitution can be seen in Figure 2.15; starting from x = 0, Co substitutes completely into the A sublattice, and then from x = 1 Co substitutes into the B sublattice [73]. As the cobalt content in the B sublattice increases, a shift from the tetragonal to cubic lattice occurs [73]. The reason for the shift from a tetragonal to cubic structure is explained in Section 2.3.6. The tetragonal to cubic transition point indicated in Figures 2.15 and 2.16 at x = 1.78 is presented for simplicity and is actually the transition from two phase cubic and tetragonal to mostly cubic spinel [73].

The lattice and the oxygen displacement parameter have been shown to mostly depend on the content of cations on the B sublattice due to the range of possible ionic radii [161]. The ionic radii of the cations that go into the B sublattice are: (Mn^{3+} = 0.065nm > Co^{III} = 0.053 nm), (Co^{2+} = 0.073 nm > Co^{III} = 0.053 nm), and (Mn^{4+} = Co^{III} = 0.053 nm) [161]. For both the reaction $Mn^{3+} \rightarrow Co^{III}$ and the reaction $Mn^{4+} + Co^{2+} \rightarrow 2Co^{III}$, the cations on the B sublattice are substituted with cations of a smaller radius [161]. This cation exchange explains the decrease in the lattice parameter, shown in Figure 2.16, as the unit cell contracts to compensate for the smaller cations [73]. Bordeneuve et al. have shown that an increase in Co causes an abrupt drop in the oxygen deviation parameter as the structure shifts from tetragonal to cubic [162]. As the Co content increases from x = 1.78 to 3 the oxygen deviation parameter is displaced further from its ideal position [162].

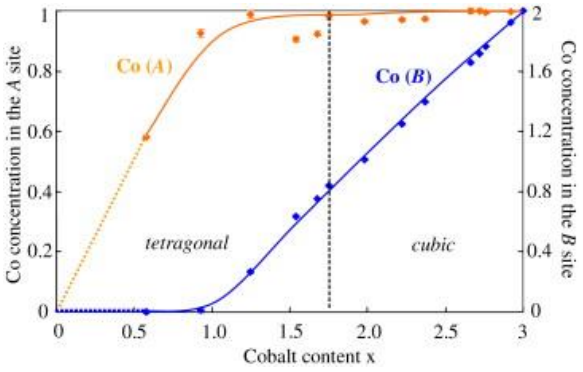

Figure 2.15. Variations of the cobalt concentrations on the *A* and *B* sites for $Mn_{3-x}Co_xO_4$ ceramics. [Reproduced from 73]

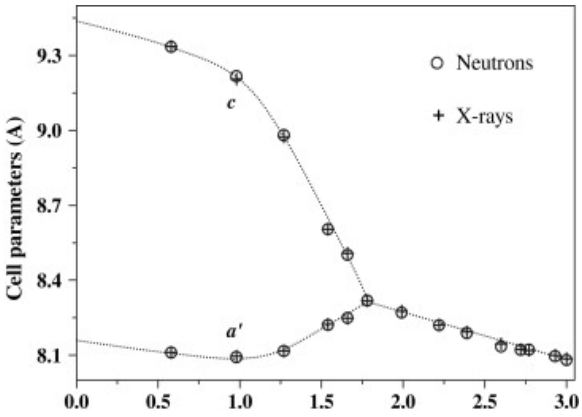

Figure 2.15. Cell variation of $Mn_{3-x}Co_xO_4$ ceramics, with $0 \leq x \leq 3$, determined from neutron diffraction measurements. X-ray data is showed for comparison [Reproduced from 73].

2.3.4 (b) Nickel Substituted MCO Spinel

Ni-substituted MCO spinels have a similar chemistry to the RL that forms on nickel-based superalloys and a modified interconnect coating composition with Ni as an additive which may have enhanced performance. The Ni substitution process is quite complex since Ni^{2+} is the stable oxidation state on the B sublattice. First, the cation site occupancy of binary Ni-spinels are considered to make sense of the Ni substitution process.

XRD data for $Co_{3-x}Ni_xO_4$ indicate that single phase cubic spinel is formed up to x = 1 [163]. In industry, the composition of Ni-spinel used for negative temperature coefficient thermistors, does not exceed x = 1 because the formation of a Ni-rich rocksalt structure, tetragonal spinel, and cubic spinel results in unreliable electrical resistance measurements [163]. Substitution of Ni into the binary spinel structure was defined by the parameter, x, and Equation 1.39 [163].

$$(Co^{2+})_A(Ni^{2+}{}_xCo^{3+}{}_{2-2x}Co^{4+}{}_x)_BO^{2-}{}_4 \qquad (1.39)$$

Therefore, substitution of Ni into Co_3O_4 occurs in the B sublattice by replacing Co^{3+} and maintaining electroneutrality by oxidizing an equivalent number of Co^{3+} to Co^{4+} [163]. This substitution mechanism explains the linear variation in the lattice parameter for $Co_{3-x}Ni_xO_4$ from x = 0 to 1 with corresponding values of 8.080 Å to 8.119 Å [164].

In the binary spinel, $Mn_{3-x}Ni_xO_4$, the substitution of Ni into Mn_3O_4 is similar to the process that occurs with $Co_{3-x}Ni_xO_4$ with Equation 1.39 [165]. For x = 0 to 1, Ni^{2+} has been shown to substitute into the B sublattice by replacing Mn^{3+} and oxidizing an equivalent number of Mn^{3+} to Mn^{4+} to maintain electroneutrality [165]. As with all spinels, increased temperature results in cation disorder. For the composition, $Mn_2Ni_1O_4$, up to 9% of the A sublattice can be filled with Ni^{2+}, which lowers the resistivity significantly [165].

There is a distinct difference in the substitution mechanism which occurs at x = 1. Electroneutrality is maintained with Ni substitution in Mn_3O_4 up to x = 1 with the oxidation of Mn^{3+} to Mn^{4+} [166]. All of the Mn^{3+} is converted to Mn^{4+} at x = 1 and with further Ni substitution electroneutrality is maintained by the oxidation of Mn^{2+} to Mn^{3+} on the A sublattice. The substation process for x > 1 is shown in Equation 1.40 [166].

$$(Mn^{2+}_{(3-2x)}Mn^{2+}_{(2x-2)})_A(Ni^{2+}_xMn^{4+}_{2-x})_BO^{2-}_4 \qquad (1.40)$$

The effect of the change in cation substation mechanism on the lattice parameter is shown in Figure 2.17 [166].

Yokoyama et al. have studied the cation site occupancy in ternary $(Mn,Co,Ni)_3O_4$ spinels to better understand the effect of composition on the electrical conductivity [166, 167, 168, 169]. The cation distribution in this ternary spinel is even more complex than the binary spinels and requires the formulation of three separate Equations, shown in Table 2.2, to describe the

substitution mechanism [167]. The composition ranges in which these three Equations apply are shown in Figure 2.18 where there is a slight deviation from Vegard's law at x = 0.5 and 0.84 [167]. The cation distribution at points A through G, in Figure 2.18, were used to derive the three Equations using structure calculations [167, 168].

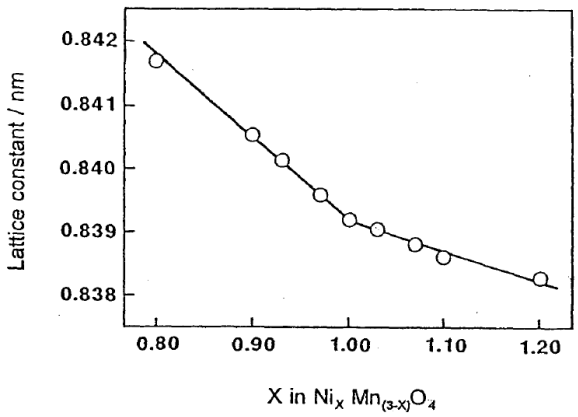

Figure 2.17: Lattice constant as a function of x in $Mn_{3-x}Ni_xO_4$ ceramics for $0.8 \leq x \leq 1.2$, determined from X-ray diffraction measurements and bond valence sum calculations. [Reproduced from 166].

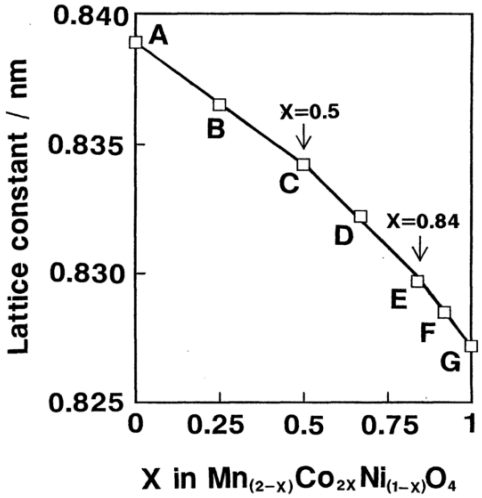

Figure 2.18: Lattice constant as a function of x in $Mn_{2-x}Co_{2x}Ni_{1-x}O_4$ ceramics for $0 \leq x \leq 1$, determined from X-ray diffraction measurements and bond valence sum calculations. [Reproduced from 167].

From the oxidation states of the cations described by these Equations, it was found that the conductivity dependence on composition was related to the ratio of Mn^{3+} to Mn^{4+} cations on the B sublattice disorder parameter, δ, given in Equation 1.44 [167].

$$\delta = Mn^{3+} \cdot \left(1 - \frac{Mn^{3+}}{Mn^{3+} + Mn^{4+}}\right) \qquad (1.44)$$

This conductivity dependence must be due to the ability of Mn to switch between oxidation states effectively lowering the activation energy necessary for polaron transport [169]. Specimens A and B were found to be n-type semiconductors because there is a greater amount of Mn^{3+} than Mn^{4+} [167]. Specimens C through G were found to be p-type semiconductors

because there is a greater amount of Mn^{4+} than Mn^{3+} [167]. In this series of Ni-substituted MCO, the highest conductivity observed is in the composition range $0.5 \leq x \leq 0.84$ [167]. In this composition range the number of charge carriers is maximized and it is probable that in the B sublattice a Mn^{4+} cation will have at least one of the 6 B site nearest neighbors occupied by a Mn^{3+} cation to allow for hole transport.

Table 2.2. Cation distributions in $Mn_{2-x}Co_{2x}Ni_{1-x}O_4$ ceramics [Reproduced from 167].

Composition Range	Equations 1.41, 1.42, and 1.43.
$0 \leq x \leq 0.5$	$(Co^{2+}_{1.16x}Mn^{2+}_{1-1.16x})_A(Ni^{2+}_{1-x}Co^{3+}_{0.84x}Mn^{4+}_{1-x}Mn^{3+}_{1.16x})_BO^{2-}_4$
$0.5 \leq x \leq 0.84$	$(Co^{2+}_{0.08+x}Mn^{2+}_{0.92-x})_A(Ni^{2+}_{1-x}Co^{3+}_{x-0.08}Mn^{4+}_{1-x}Mn^{3+}_{x+0.08})_BO^{2-}_4$
$0.84 \leq x \leq 1$	$(Co^{2+}_{0.5+0.5x}Mn^{2+}_{0.5-0.5x})_A(Ni^{2+}_{1-x}Co^{3+}_{1.5x-0.5}Mn^{4+}_{1-x}Mn^{3+}_{0.5x+0.5})_BO^{2-}_4$

2.3.4 (c) Iron Substituted MCO Spinel

Cation site occupancy studies on Mn ferrite spinel have shown that Mn substitution in $Mn_xFe_{3-x}O_4$ occurs preferentially on the A sublattice according to Equation 1.45 from x = 0 to 1 [170, 171].

$$(Mn^{2+}_xFe^{3+}_{1-x})_A(Fe^{2+}_{1-x}Fe^{3+}_{1+x})_BO^{2-}_4 \quad (1.45)$$

The substitution of Mn^{2+} into the A sublattice of Fe_3O_4 may be due to Mn^{3+} having an unfavorable symmetry to occupy the B sublattice. Fe^{2+} substitution on the B sublattice creates a trigonal distortion along the [111] direction, which acts to compress the unit cell acting against the tendency for Mn^{3+} substitution to expand the unit cell [172].

Cation site occupancy studies on Co ferrite spinel have shown that Co substitution in $Co_xFe_{3-x}O_4$ occurs preferentially on the B sublattice according to Equation 1.46 from x = 0 to 1 [152].

$$(Fe_1)_A(Co_xFe^{2+}_{1-x}Fe^{3+}_1)_BO^{2-}_4 \quad (1.46)$$

Co^{2+} has a similar effect with trigonal distortion compared to Fe^{2+} and may satisfy the elastic constraints for substitution in the B sublattice [151]. Another reason Co may substitute directly into the B sublattice of Fe_3O_4 is that charge compensation is not necessary for the replacement of Fe^{2+} with Co^{2+} on the B sublattice. Substitution of Co greater than x = 1, occurs preferentially on the A sublattice due the large ionic radius of the Co^{2+} cation and the ability for the A sublattice to accommodate larger cations [152].

Co-refinement of neutron and X-ray diffraction data taken at 950 °C for $Mn_1Co_1Fe_1O_4$ has also shown that Mn substitutes on the A sublattice and Co substitutes on the B sublattice. The crystallochemical formula for $Mn_1Co_1Fe_1O_4$ is $(Mn_{0.44}Co_{0.02}Fe_{0.54})_A(Mn_{0.56}Co_{0.98}Fe_{0.46})_BO_4$ [150]. The measured cation distribution in these studies is not consistent with the site preference enthalpy for each of these cations [160].

Configurational entropy cannot be used to explain the difference in measured cation site occupancies for with their cation site preference [173]. It is possible that the lattice measurements made by Benard et al. were not accurate enough to determine the cation site occupancy [150]. The accuracy of the lattice parameter calculations was ± 0.005 Å and there is only a deviation of 0.08 Å across the composition range from $CoFe_2O_4$ (a = 8.39 Å) to $CoMn_2O_4$ (a = 8.47 Å) [150].

2.3.4 (d) Chromium Substituted MCO Spinel

Cation site occupancy studies on Cr-containing spinel have all concluded that Cr prefers the B sublattice. However, in one study the calculated x-ray diffraction intensities for $Mn_1Co_1Cr_1O_4$ have been reported to best match experimental results for the cation distribution, $(Mn^{2+})_A(Co^{3+}Cr^{3+})_BO_4$ [174]. This result is contrary to other experiments where Mn prefers the B sublattice and Co prefers the A sublattice in $(Mn,Co,Cr)_3O_4$ [136, 152]. The measured lattice parameter was 8.34 ± 0.02 Å and oxygen parameter, $u^{\bar{3}m}$, was 0.261 ± 0.002 [174]. The precision in the reported lattice parameter measurement is too low to make a confident assessment of the cation distribution [174]. The lattice parameter and oxygen parameter make a better match by considering Co^{2+} and Mn^{3+} to occupy the A and B sites, respectively.

2.3.5 Calculation of Oxidation States of Cations in Spinel

The oxygen parameter can be calculated with Equation 1.47, where R is given in Equation 1.48 as the ratio of the octahedral and tetrahedral effective cation radii [135]. The effective cationic radius is defined as the sum of the ionic radii of the cation and anion. The distribution of chemical species across both the A and B sublattices results in an average ionic radius for each sublattice. Equation 1.49 and Equation 1.50 describe the average ionic radii of the cations on the A and B sublattice in disordered spinels, where x indicates the degree of inversion from 0 to 1 [135].

$$u^{4\bar{3}m} = \frac{\frac{1}{2}R^2 - \frac{11}{12} + \left(\frac{11}{48}R^2 - \frac{1}{18}\right)^{1/2}}{2R^2 - 2} \tag{1.47}$$

$$R = \frac{R_B + R_O}{R_A + R_O} \tag{1.48}$$

$$R_A = (1-x)R_A^{2+} + (x)R_A^{3+} \quad (1.49)$$

$$R_B = (0.5x)R_B^{2+} + (1-0.5x)R_B^{3+} \quad (1.50)$$

Values for the ionic radii have been compiled and published by Shannon [139]. However, these values rely on data from several structures and have been found to give certain systematic differences when calculating the lattice and oxygen parameters for spinel by Hill et al [175]. O'Neil and Navrotsky have determined ionic radii values based only on data from spinel in which the oxidation states of the cations and the cation site occupancy was unambiguously known [140]. The ionic radii values have been obtained by a process of adjustment in increments of 0.005 Å using Equations 1.51 and 1.52 until there was an optimum match of the lattice parameters for a set of 66 spinel compositions to their experimentally measured lattice parameters [140]. The ionic radius of oxygen, R_O, was considered to be 1.38 Å. The results of this analysis are shown in Figure 2.19 [140].

$$\mathrm{R}_A = a\sqrt{3}\left(u - \tfrac{1}{4}\right) - \mathrm{R}_O \quad (1.51)$$

$$\mathrm{R}_B = a\sqrt{2[(u-\tfrac{3}{8})^2 + (\tfrac{5}{8}-u)^2]} - \mathrm{R}_O \quad (1.52)$$

As seen in Figure 2.19, the calculated effective cationic radii yield discrepancies which makes accurate calculations of the cation distribution based on the lattice parameter difficult [140]. The effective cationic radii presented by O'Neil and Navrotsky for the relevant chemical constituents in the reactions layers developed between alloy interconnects and MCO coatings is shown in Table 2.3 [140]. As larger cations are substituted onto the A sublattice, the oxygen ions displace along the [111] direction, causing the tetrahedra to expand at the expense of the

octahedra. Therefore, the bond lengths of the A and B sites determine the aspect ratio of the unit cell.

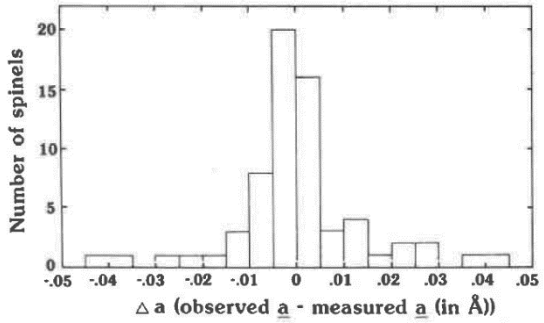

Figure 2.19: Histogram showing the differences between experimentally measured lattice constants (a) and the lattice constants obtained from the calculated ionic radii. [Reproduced from 140].

Table 2.3: Ionic radius (Å) for the chemical constituents found in the reaction layers formed between MCO and interconnect alloys. [Reproduced from 140].

Charge	Mn	Co	Cr	Ni	Fe
			A Site (R_A)		
2+	0.655	0.580		0.565	0.615
3+			0.615		0.485
			B Site (R_B)		
2+		0.720		0.690	0.740
3+	0.645		0.615		0.645
III		0.530		0.560	
4+	0.53				

The amount of mixing on the B sublattice is difficult to calculate with precision due to the small variation in lattice parameter with the possible alternate oxidation states, Mn^{4+} and Co^{2+} [161]. With a variance in the measurement of peak position by ±0.02°, the precision in the measurement of the lattice parameter is ±0.005 Å. Combined with the variance in reported data for the effective cation radii measured in spinels [140, 166], there is too much uncertainty in the calculation of the cation site occupancy. The radii must depend on the composition of the spinel and therefore cannot be used to accurately determine the cation distribution. Lattice parameter calculations based on the average radii can however, be used to check the general site preference of cations in spinel.

2.3.6 Jahn-Teller Distortion

The valency of the cations present in the MCO-based spinels can be evaluated with the critical concentration of Jahn-Teller ions necessary to cause a tetragonal phase transformation [176]. The Jahn-Teller effect is due to the lowering of energy by removing orbital degeneracy [156]. This distortion effect is described by the crystal field splitting parameter, Dq, and the highest value in spinels is observed for Mn^{3+} ions in octahedra [155]. For MCO, a molar content of 1.25 Mn on the B sublattice of which 1.1 is Mn^{3+} is necessary for tetragonal extension of the unit cell, where c > a [155]. At the transition point, $Mn_{1.25}Co_{1.75}O_4$, a cation mole fraction of 0.15 Mn must take the Mn^{2+}/Mn^{4+} state and/or occupy the A site.

The critical content for the binary spinel, $(Mn,Cr)_3O_4$, is 0.35 Mn^{3+} at liquid helium temperature and 0.4 Mn^{3+} at room temperature [156]. An increase in temperature deceases the long range order in which a domain is formed by the collective orientation of the prolate axis in octahedra and therefore increases the critical Mn^{3+} content [177]. At 950 °C, tetragonal distortion for $Mn_xCo_1Cr_{2-x}O_4$ occurs at a critical content of 1.2 Mn^{3+} [136]. In this case substitution for Cr^{3+} by Mn^{3+} has been assumed to take place solely on the B sites [136]. Along with temperature, the addition of Co also increases the critical Mn^{3+} content. Co^{2+} partly counteracts the Mn^{3+} ions to compress the unit cell along the c-axis, c < a [172]. Besides Co^{2+} causing oblate distortion, Co^{2+} would also cause oxidation of Mn^{3+} to form Mn^{4+} reducing the number of Jahn-Teller ions. Cr substitution acts in a different way to increase the critical content by breaking up clusters of Mn^{3+} ions on the B sublattice, and therefore lowering the cooperative distortion [136]. But Cr^{3+} has a high Dq value, which can also account for the large tetragonal distortion seen compared to Fe and Ni substituted MCO-based spinels [178].

2.3.7 Computational Approach to Study Cation Distribution in Spinel

The computational approach for studying the site preference between the reaction products that form allows experimental results to be explained in theory. The most common theoretical techniques to compute the cation site occupancy of spinel are crystal field theory (CFT) and then ligand field theory (LFT). The effectiveness of these two techniques are generalized by F.A Cotton's assertion that, 'crystal field theory of bonding is too good to be true and ligand field theory is too true to be good [179].' In essence, CFT can describe the cation site occupancy in terms of the energy of atomic orbitals while LFT is in terms of the energy of molecular orbitals. CFT is a simplified approach which does not account for covalent bonding and LFT is complicated by the orbital overlap and symmetry constraints. Density functional theory (DFT) can give the most exact measurement of the cation site occupancy by calculating the minimum of the ground state energy with the electron wave functions. Thus far with DFT, only binary spinel systems have been studied to describe the geological formation of mostly aluminate spinels within the earth's crust [180, 181, 182].

2.3.8 Electronic Conductivity of Spinel

The electronic conductivity accounts for the majority of the charge flux through spinels due a small polaron hopping mechanism. The transport of polarons is generated by thermally activated hopping [121, 122]. Thus, at the temperatures in which SOFCs operate, charge transport is relatively high in spinels.

The polaron hopping occurs between octahedral sites which form chains in the [110] directions [183]. The distance between the B sites responsible for the mechanism of conductivity is $a\sqrt{2}/4$ for cubic and $a'\sqrt{2}/4$ where $a' = \sqrt[3]{a^2c}$ for tetragonal spinel [184]. A shorter distance between sites may enable a higher conductivity but the conductivity has been shown to have a greater dependence of the number of charge carriers.

In Figure 2.20, the greatest amount of mixing of the B sublattice and thus the greatest number of charge carriers can be seen at x = 2, which corresponds to the highest conductivity [73]. The cation distributions in $Mn_{3-x}Co_xO_4$ ceramics ($0 \leq x \leq 3$) shown in Figure 2.20 were determined by the bond

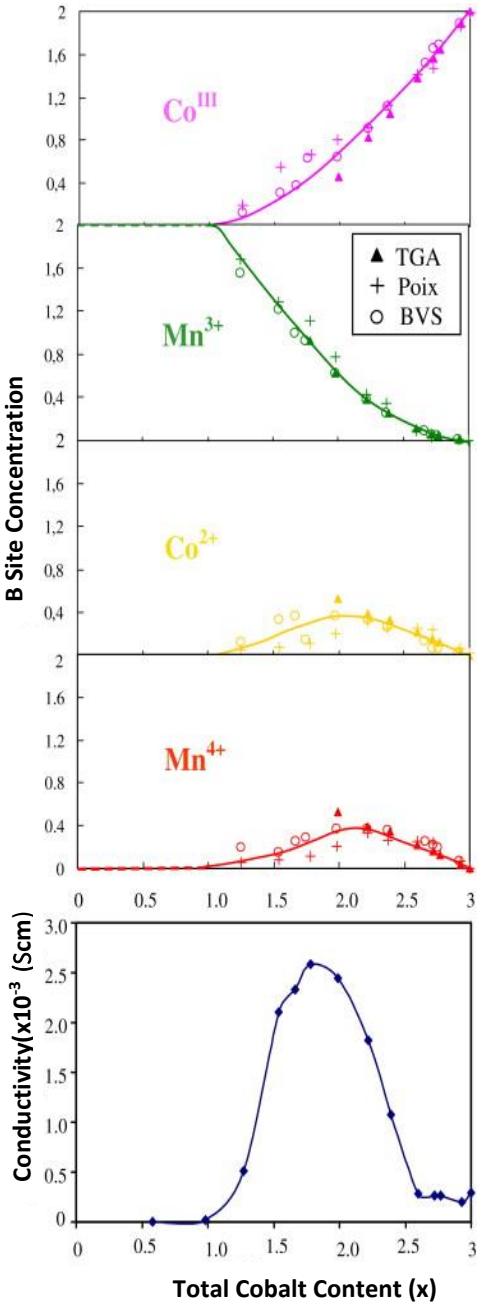

Figure 2.20: Variations of cation concentrations on the B site and ac conductivity $\sigma(\omega)$ as a function of composition (x) for $Mn_{3-x}Co_3O_4$ dense ceramics, with $0 \leq x \leq 3$ [73].

valence sum (BVS) calculations from refinement of neutron diffraction data [73] and compared to the structural methods following Poix's work [185], and TGA data obtained on powders for 2 ≤ x ≤ 3 [143]. The conductivity measurements were made at room temperature, but the ceramics were quenched from 800 °C in an attempt to maintain the high temperature disorder [73].

The electronic conductivity is related to the electron configuration of the chemical species on the B sublattice. Co and Mn can support a charge transfer by changing the valence state on the B sublattice but the symmetry of the Cr^{2+} cation on the B sublattice makes this oxidation state too unfavorable and hinders the charge transfer.

2.3.9 Permittivity of Spinel

The electronegativity of the ions in the RLs is: Mn (1.55), Co (1.88), and Cr (1.66). Compared to O which is 3.44, the difference elicits a polar covalent bond. Considering ionic conductivity, the atoms of a higher electronegativity create a structural network and small ions can provide charge transport. The small ions fit into the octahedral site and lithium spinels are the best example in which spinels are used for their ion transport properties in re-chargeable batteries [186].

The permittivity of MCO is directly related to Mn substitution in Co_3O_4 spinel. The Mn^{3+} creates an off center symmetry in the unit cell and allows ferroelectric behavior at room temperature [143]. Thin dense ceramic samples with contacts of silver paste were used to measure the capacitance, C, which can be used to calculate the dielectric constant of the material, k_m, with Equation 1.53,

$$C = k_0 k_m A/d \quad (1.53)$$

where k_0 is the permittivity of free space. In the measurement of capacitance, a large surface area, A, and thin specimen thickness, d, are typically used to decrease experimental error.

The dielectric constant and loss has provided important information about the structure of MCO. The properties of dielectric constant and conductivity increase with the increase of Mn from pure Co_3O_4 to Co_2MnO_4 [143]. As the Mn content increases, the structure shifts away from its equilibrium position. Lattice distortion causes the center of charge to shift and a dipole is created, which is measured by the distance between two separate charges. Meena et al. were not able to determine the permittivity of a single crystallographic orientation due to the use of polycrystalline ceramics [143].

In the composition ranges of x from 0.3 to 0.7 in $Co_xMn_{3-x}O_4$ where random substitution of Co occurs, the loss tangent was the highest [143]. This means that the oscillations at that frequency (electronic, dipole, ionic, and molecular) lag behind the AC electric field. This causes dissipation in the lattice and generates heat. It is important to tune the structure to have minimal loss at the frequency for the device which is operating. Nickel ferrite spinels can be used as the insulator material in resistive random access memory devices due to their unipolar switching behavior [187].

2.4 Oxidation of MCO Coated Crofer 22 APU

2.4.1 Microstructural Development

In one respect, the kinetics of an interconnect system with a spinel coating deposited onto a chromia-forming metal alloy can be similar to just the bare alloy. The model of a bare

alloy assumes that at the chromium ions reach a point where they are oxidized by an abundant source of oxygen ions within the chromia scale. If oxygen ions can diffuse into and through the spinel and reach the spinel/scale interface, this interface can be effectively considered to be on the surface and open to free air. Crude evidence that the oxygen ions do penetrate through the bulk of the spinel before the chromium ions can advance, comes from the fact that a chromia scale does not form on the outside surface of the spinel [70].

Magdefrau et al. have performed one of the first controlled studies on the chemistry, crystal structure, and morphology of the interfacial region that develops between interconnect alloys and MCO protective coatings after long term oxidation [71]. The interfacial analyses were performed using a combination of TEM and STEM on FIB-cut specimens and one such analysis is shown in Figure 2.21 [71]. The features in this STEM image from left to right are: the Crofer 22 APU alloy with the white arrows indicating the internal TiO_x, pockets of a $MnCr_2O_4$ subscale (SS), the chromia scale, and a $(Mn,Co,Cr)_3O_4$ RL. From the chromia scale to the RL, there is an abrupt drop in Cr-content by 35 at%, thereafter the Cr-content gradually decreases. The solubility limit of Cr in spinel is equivalent to the number of B sites [77] and the RL at the chromia scale

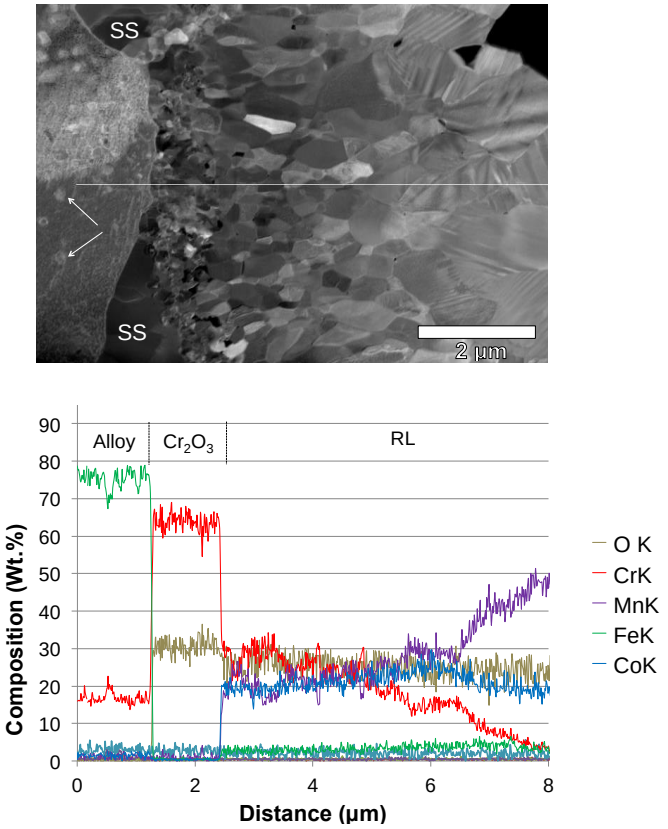

Figure 2.21: Dark field STEM image and EDXS line- scan obtained from a FIB cross section through MCO-coated Crofer 22 APU oxidized at 800 °C for 1000 h [Reproduced from 71].

interface has reached this solubility limit. The reaction layer at the chromia scale interface has a finer grain microstructure than the rest of the coating indicating that there is nucleation and growth of the spinel grains with high Cr-content. For this process to occur, Mn^{2+} and Co^{2+} ions must diffuse inward and react with the Cr at the chromia scale interface. Thus, the RL indicated in Figure 2.21 is actually an interfacial region composed of two layers: one of $(Mn,Co)Cr_2O_4$ formed at the chromia scale surface and one of $(Mn,Co,Cr)_3O_4$ formed through the coating [71]. Wang et al. have shown cross-sectional SEM images of the two layer interfacial region from a diffusion couple experiment between a chromia and MCO ceramic block [188].

The interfacial layer of high Cr-content that forms has a significant effect on the performance of the coating [71]. The bare alloy model cannot entirely explain the growth of the chromia scale due to concurrent diffusion of Cr^{3+} and O^{2-} ions through the MCO spinel coating.

2.4.2 Kinetics

Prior to this detailed microstructural examination, a simple two layer model of a coating and chromia scale was used to explain the oxidation behavior [189, 190]. Now, a three layer model of a coating, intermediate region, and scale has been proposed and fit to experimental results [70]. The circuit shown in Figure 2.22

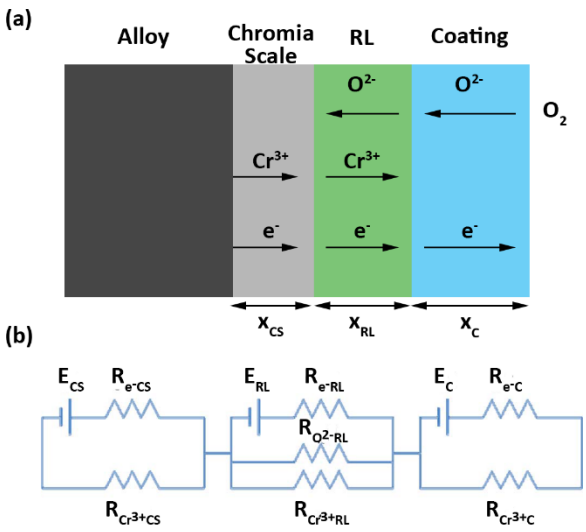

Figure 2.22: a) Illustration of ionic and electronic fluxes. b) An equivalent circuit for the trilayer flux model [Reproduced from 70].

represents indicates three layers in series which each have an electronic and ionic path in parallel [70].

The three layer model, shown in Figure 2.22, accounts for the progress of the oxygen ions slowing down before reaching the chromia scale. This makes sense because an increase of chromium ions causes the tetragonal distortion to decrease, thereby confining the O^{2-} ions in a more close packed structure and increasing the activation energy necessary for diffusion.

In the chromia scale, the transport of Cr ions is much faster than the transport of oxygen ions [80]. This allows the Cr ions to reach the chromia interface and enter the spinel region before reacting with O^{2-}. Once neutralized their diffusion is inhibited. The purpose of the coating is to prevent the egress of Cr and the ingress of O. Limiting the growth of the chromia scale and RL will result in a greater overall electronic conductivity.

Finally, the Nernst-Einstein relationship can give the ionic conductivity by taking self-diffusion coefficients calculated above [124].

$$\sigma_i = \frac{z_i^2 e^2 c_i D_i}{kT} \tag{1.54}$$

Where σ_i is the ionic conductivity of the diffusing species, z_i is the net charge of the ion, c_i is the concentration of the ions (atoms/volume) or mobile defects, k is Boltzmann's constant and T is temperature.

The charged ions are acted upon by an electromotive force (EMF). The mass transport can be related to the change in free energy through the Equation for the EMF with the number of electrons in the reaction, n, and the Faraday constant, F [70].

$$E_t = -\frac{\Delta G}{nF} \tag{1.55}$$

The current, *I*, in the equivalent circuit can then be described in terms of the electromotive force, *E*, and the ionic/electronic resistance, *R* for each of the three layers in Equations 1.56, 1.57, and 1.58 [70].

$$I_{e^-C} = \frac{E_C}{R_{O^{2-}C} + R_{e^-C}} \tag{1.56}$$

$$I_{e^-RL} = \frac{E_{RL}}{R_{e^-RL} + \frac{R_{O^{2-}RL} R_{Cr^{3+}RL}}{R_{O^{2-}RL} + R_{Cr^{3+}RL}}} \tag{1.57}$$

$$I_{e^-CS} = \frac{E_{CS}}{R_{Cr^{3+}CS} + R_{e^-CS}} \tag{1.58}$$

The total electrical current through the coating, RL, and chromia scale is given by the parallel combination of the current in each of the three layers in Equation 1.59 [70].

$$I_{e^-} = \frac{E_T}{R_{O^{2-}C} + R_{e^-C} + R_{e^-RL} + \frac{R_{O^{2-}RL} R_{Cr^{3+}RL}}{R_{O^{2-}RL} + R_{Cr^{3+}RL}} + R_{Cr^{3+}CS} + R_{e^-CS}} \tag{1.59}$$

Taking into account the thickness of each layer the total electrical current across a surface area, A, is given by Equation 1.60 [70].

$$I_{e^-} = \frac{E_T}{\frac{x_{CS}}{A}\left(\frac{\sigma_{Cr^{3+}CS} + \sigma_{e^-CS}}{\sigma_{Cr^{3+}CS}\sigma_{e^-CS}}\right) + \frac{x_{RL}}{A}\left(\frac{1}{\sigma_{e^-RL}} + \frac{1}{\sigma_{Cr^{3+}RL}\sigma_{O^{2-}RL}}\right) + \frac{x_C}{A}\left(\frac{\sigma_{O^{2-}C} + \sigma_{e^-C}}{\sigma_{O^{2-}C}\sigma_{e^-C}}\right)} \tag{1.60}$$

The symbols for each of these properties in the three layers are given below [70].

I_{e^-C} electronic current of coating

I_{e^-RL} electronic current of the RL

I_{e^-CS} electronic current of the chromia scale

I_{e^-} total electronic current

E_C EMF in spinel coating

E_{RL} EMF in the Cr-modified reaction layer

E_{CS} EMF in the chromia scale

E_T total EMF

R_{e^-CS} σ_{e^-CS} electronic resistance and conductivity of the chromia scale

R_{e^-RL} σ_{e^-RL} electronic resistance and conductivity of the RL

R_{e^-C} σ_{e^-C} electronic resistance and conductivity of coating

$R_{Cr^{3+}CS}$ $\sigma_{Cr^{3+}CS}$ Cr^{3+} ionic resistance and conductivity of the chromia scale

$R_{Cr^{3+}RL}$ $\sigma_{Cr^{3+}RL}$ Cr^{3+} ionic resistance and conductivity the RL

$R_{O^{2-}RL}$ $\sigma_{O^{2-}RL}$ O^{2-} ionic resistance and conductivity of the RL

$R_{O^{2-}C}$ $\sigma_{O^{2-}C}$ O^{2-} ionic resistance and conductivity of coating

The electronic current corresponds to the majority of the charge flux through the three layers. With an increase in thickness of the chromia scale and RL, the electrical current decreases due to the relatively low electrical current of these layers. The three layer equivalent circuit model is much better than the two layer model because the properties in each layer are so different. For example, the oxygen ionic resistance in the chromia scale is greater than

spinel, while the chromium ionic resistance is greater in the spinel than chromia. The diffusivity of O^{2-} chromia and Cr^{3+} in spinel supports the theory that the $(Mn,Co)Cr_2O_4$ spinel grows at the chromia scale interface. There must be a surplus of O^{2-} and Cr^{3+} at the chromia scale surface which translates to the formation of $(Mn,Co)Cr_2O_4$ because spinel is more thermodynamically favorable [191]. The formation of the $(Mn,Co)Cr_2O_4$ is rate limited by the diffusion of Mn^{2+} and Co^{2+} ions to the chromia scale surface.

2.4.3 Effect of Cation Site Occupancy on Kinetics

A way to decrease the diffusion of Mn^{2+} and Co^{2+} cations to the chromia surface would be to alter the starting composition of the MCO coating to include a cation which prefers the A sublattice more than Mn^{2+} and Co^{2+}. Navrotsky and Kleppa's determination of cation site preference, Zn^{2+} may substitute on the A sublattice and impede the inward diffusion of Mn^{2+} and Co^{2+}. $ZnCr_2O_4$ has a more negative free energy of formation than $CoCr_2O_4$ and $MnCr_2O_4$ and may preferentially react with Cr to form a $ZnCr_2O_4$ inner RL. For this reason, Zn may not be the best option to limit the growth of the high Cr-content inner RL [74]. The cation must have a limited reactivity with the chromia scale to form spinel. A better option may be to substitute MCO with Fe because Fe is not known to preferentially react with Cr to form spinel [192]. Fe^{3+} has a greater site preference for the A site than Mn^{2+} and Co^{2+}, and Fe^{2+} has a low OSFE [160].

Fergus et al. have found that the diffusivity of Cr through MCO is decreased by altering the starting composition to include Fe and Ti [193]. Figure 2.23 indicates the extent of the Cr diffusion after a diffusion couple experiment between a chromia pellet and pellets of MCO and MCO doped with Fe and Ti [193]. Fe had a better effect than Ti on limiting Cr diffusion [194]. Of

the Fe-substituted MCO spinels, the composition, $MnCo_{0.77}Fe_{0.34}O_4$, limited the outward Cr^{3+} diffusion the best [195]. The study showed that Fe was not present in the $(Mn,Co)Cr_2O_4$ inner RL where there are two Cr atoms per M_3O_4 unit. Fergus et al. did not propose a mechanism to explain why the addition of Fe to MCO spinel inhibited outward Cr diffusion [193]. The two ways to decrease the extent of Cr^{3+} diffusion through protective interconnect coatings are to limit the growth of the inner and outer RLs. From the diffusion profile in Figure 2.23, it seems like the addition of Fe and Ti to MCO has an effect on limiting the both the inner RL and outer RL [193].

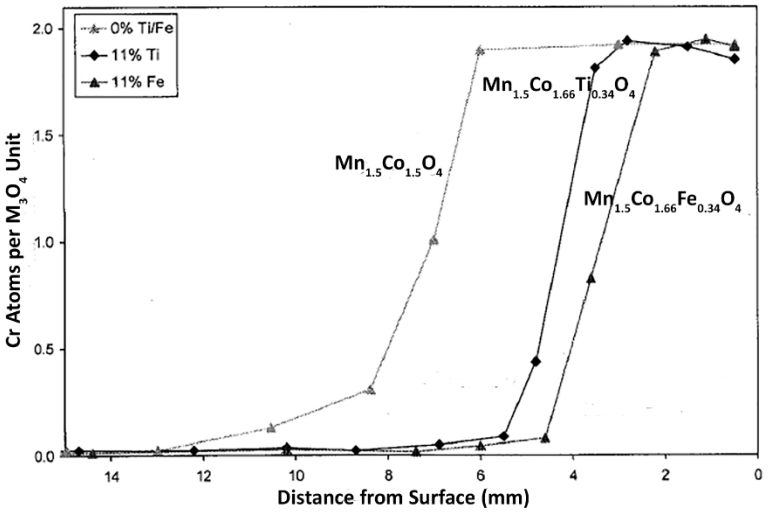

Figure 2.23: Cr contents in undoped, Ti-doped, and Fe-doped $(Mn,Co)_3O_4$ [Reproduced from 193].

Sun has measured the diffusivity of Co^{2+} and Cr^{3+} in $CoCr_2O_4$ and has proposed a mechanism for the diffusion of these cations [Sun]. At the same temperatures Cr was found to have a higher diffusion coefficient than Co even though the activation energy, Q, necessary for Cr transport is higher (Q_{Cr} = 3.04 eV and Q_{Co} = 2.39 eV) [183]. The activation energy for Cr transport is higher than other transition metal cations since the shape of the Cr^{3+} electron cloud makes its ionic radius appear larger to the tetrahedral site. Therefore, the mechanism for Cr diffusion relies on the direct transport of Cr from an occupied to unoccupied octahedral site which must be accommodated by a lattice strain equal to the size of the Cr^{3+} ionic radius [197].

The diffusivity of Cr is faster than Co because there are more possible migration routes for cations occupying the B sublattice.

The derivation parameter, n, describes the probable migration route for a diffusing species based on the Debye temperature, activation energy, and mass of the ion. This is related to the average inverse of the jump distance that a cation may take in a given structure. Each occupied B site is surrounded by 12 nearest neighbors (n = 2.83), half of which are unoccupied. Each occupied B site is surrounded by 8 nearest A sites (n = 4.62), all of which are unoccupied. Each occupied A site is surrounded by 6 nearest A sites (n = 4) and 4 nearest B sites (n = 4.62), all of which are unoccupied [183]. Grimes has evaluated the probable migration path for several transition metal elements based on the derivation parameter calculated with CFT. Higher values of the derivation parameter indicated that the cation transports along the A sublattice since the average n values for the A sublattice are higher. Conversely, lower values indicate that the diffusing transports along the B sublattice. Grimes has confirmed the mechanism proposed by Sun that Cr diffuses mainly through the B sublattice.

Since Co has a relatively low site preference for both the A and B sublattice, the migration route can take the path of least resistance by hopping from the A site to an unoccupied B site and back to the A site. The activation energy necessary for Co^{2+} and Cr^{3+} transport in $CoCr_2O_4$ is 2.22 eV and 3.04 eV, respectively. Since Zn^{2+} has a higher site preference for the A sublattice, the migration route for Zn^{2+} involves direct jump across A sites, and the activation energy necessary for diffusion is even higher than Cr^{3+} in $ZnCr_2O_4$ spinel (Q_{Zn} = 3.72 eV and Q_{Cr} = 3.52 eV) [183]. Interestingly, the activation energy necessary for Cr diffusion is also

higher in $ZnCr_2O_4$ than $CoCr_2O_4$ and therefore, and for this reason Zn may be an additive to retard Cr diffusion in MCO interconnect coatings.

With perfect packing of oxygen ions cation diffusion should take place by cations hopping to a vacant A site and then to a vacant B site. But with normal spinels having a $u^{\bar{4}3m}$ parameter greater than 0.385, direct diffusion along octahedral sites becomes easier due to separation of the oxygen ions [183]. For oxygen diffusion in spinel there are three possible pathways. Six neighbors form a plane parallel to (111) in which the orientation is almost unaffected by the deviation parameter. The other two pathways are two sets containing three neighbors each, which depend on the deviation parameter [183]. A lower deviation parameter may decrease O^{2-} diffusivity through spinel by decreasing the volume for free oxygen displacement.

The key to producing a better protective coating would not be to force Cr to the tetrahedral site to increase electronic conductivity, but to trap the Cr^{3+} on the octahedral site by changing the symmetry of the unit cell to limit Cr^{3+} and O^{2-} diffusion. By optimizing the coating composition, a smaller deviation parameter can be achieved and result in a more close packed structure effectively increasing the activation energy necessary for oxidation.

2.5 Focus of Thesis Research

There are three main objectives in this thesis which address the degradation derived from manganese cobaltite spinel coated alloy interconnects in intermediate temperature solid oxide fuel cells.

1. To investigate the interactions between the coating and substrate during reactive sintering of slurry-deposited MCO and thus to develop an understanding of the mechanisms for the densification and substrate adherence.
2. To determine cation site distributions within MCO-based spinels using ALCHEMI, to explore the viability of using ALCHEMI to study local site occupancies in spinel RLs, and thus to elucidate the mechanisms and kinetics for RL formation at alloy/coating interfaces.
3. To study the effects of material and process parameters on the morphology and microstructure of pulsed laser deposited MCO films and to study the interaction of these films with the alloy substrate.

Chapter 3:

Microstructural Effects of the Reduction Step in Reactive Consolidation of Manganese Cobaltite Coatings on Crofer 22 APU

3.1 Introduction/Preamble

A scalable reactive sintering process has been developed for the application of MCO spinel coatings to metallic interconnects [198]. This comprises: application of an MCO slurry, drying, reduction in moist H_2-based forming gas to form a MnO/Co phase mixture, and then re-oxidation in air to form a relatively dense MCO coating. Magdefrau et al. have shown previously [70] that such coatings inhibit the oxidation kinetics significantly for ferritic stainless steels such as Crofer 22 APU under SOFC operating conditions. A Cr-modified spinel reaction layer (RL) was detected at the alloy/coating interface and the effects of this layer were described using a 3-layer oxidation kinetics model based upon an equivalent circuits approach.

In recent work by Magdefrau et al., a combination of focused ion beam (FIB) sectioning and electron microscopy techniques was used to reveal the details of the oxide scale microstructures for uncoated and MCO-coated Crofer 22 APU [71, 96]. It was found that the uncoated Crofer formed a two-layer chromia + $MnCr_2O_4$ scale, whereas the MCO-coated Crofer exhibited a $(Mn,Co,Cr,Fe)_3O_4$ spinel RL between the coating and the chromia sub-scale on the

Crofer substrate surface. The development of the RL was studied by comparing data from coated samples oxidized for different times at 850 °C in air. An unusual variation in the composition of the spinel RL was observed wherein the Cr content decreased during the initial stages of oxidation and then increased $_{again}$ for longer exposures [96]. It was proposed that this effect might arise due to outward diffusion of Cr from the Crofer substrate into the metallic Co phase during the reduction stage of the reactive sintering process. To test this hypothesis, we have now prepared a sample for which the MCO slurry coating on Crofer has been reduced but not re-oxidized. The microstructure of this reduced coating has been investigated using FIB and electron microscopy as in our previous studies [71, 96]. It is shown that the interfacial microstructure in this sample is somewhat different from that anticipated, with thin chromia and spinel layers forming even during the reduction step. The consequences of these observations for the mechanisms of microstructural development in MCO coatings are discussed.

3.2 Materials and Methods

Square coupons (25 mm by 25 mm) were cut from 0.5 mm thick Crofer 22 APU commercial sheet stock. The coupon surfaces were prepared by: mechanical grinding with successively finer grades of SiC paper, polishing with 6 µm diamond paste, ultrasonic cleaning in an acetone bath, and then rinsing with isopropanol. $Mn_{1.5}Co_{1.5}O_4$ powder purchased from Praxair was used to form a slurry, which was used to coat the alloy coupons using a variant of the process sequence described by Yang *et al.* [198] A layer of the slurry was applied to the polished surfaces of the coupons, and these were then dried in an oven at 100 °C for 2 h. The

dried samples were then reduced in a sealed tube furnace under flowing Ar/2.75%H_2 /3%H_2O at 850 °C for 4 h, resulting in a porous coating of approximately 27 μm in thickness.

Metallographic cross-sections were prepared by mounting the reduced coupons in a two-part cold mount epoxy, grinding using successively finer grades of SiC paper, and then polishing using diamond paste down to 0.25 μm. Scanning electron microscopy (SEM) was performed using a JEOL 6335F Field Emission SEM.

Site-selective transmission electron microscopy (TEM) sample preparation was performed using a FEI Strata 400S Dual Beam focused ion beam (FIB) instrument equipped with a flipstage and a scanning transmission electron microscopy (STEM) detector for improved final thinning. In-situ platinum deposition was performed to protect the surface of the TEM specimen during ion milling. Ga^+ beam currents were reduced iteratively to a value of 9.7 pA during final milling to avoid excessive Ga^+ implantation and beam damage. TEM foils were mounted onto copper Omni grids and attached at 2 corners to limit mechanical buckling of the samples during final thinning.

TEM analysis was performed using a FEI T12 Tecnai S/TEM operated at 120 kV equipped with an EDAX ultra-thin window energy-dispersive X-ray spectrometry (EDXS) system. For higher resolution analysis, a JEOL JEM-2010 TEM operating at 200 kV was used. This microscope is equipped with a UHR objective lens polepiece (C_s = 0.5 mm), which gives a point-to-point resolution of <0.19 nm at Scherzer defocus, and an EDAX Phoenix EDXS detector that has a super-ultrathin polymer window. STEM analysis was performed using a Philips CM-200 Supertwin operating at an accelerating voltage of 200 kV and equipped with an EDAX 30 mm^2 Si(Li) EDXS detector.

3.3 Results

The overall morphology and microstructure of the reduced MCO coating were first investigated using secondary electron (SE) SEM imaging. Figure 3.1(a) is a representative low magnification SE SEM image obtained from a metallographic cross-section showing the bright alloy substrate on the left and the dark epoxy mount on the right. The porous coating occupies most of the field of view, and it is noted that the pores are filled with epoxy due to infiltration during the mounting process. This infiltration is necessary to preserve the coating structure during subsequent grinding and polishing. A typical higher-magnification SE SEM image obtained from a region near the center of the coating is shown in Figure 3.1(b). Image analysis revealed that these areas contain about 14% of a bright equi-axed phase surrounded by 32% of a darker agglomerated phase; the remaining 54% of the microstructure corresponds to the epoxy-filled pores. Most of the coating exhibits this phase distribution. The notable exception is an interfacial layer of around 3 μm in thickness between the Crofer substrate and the porous coating. The

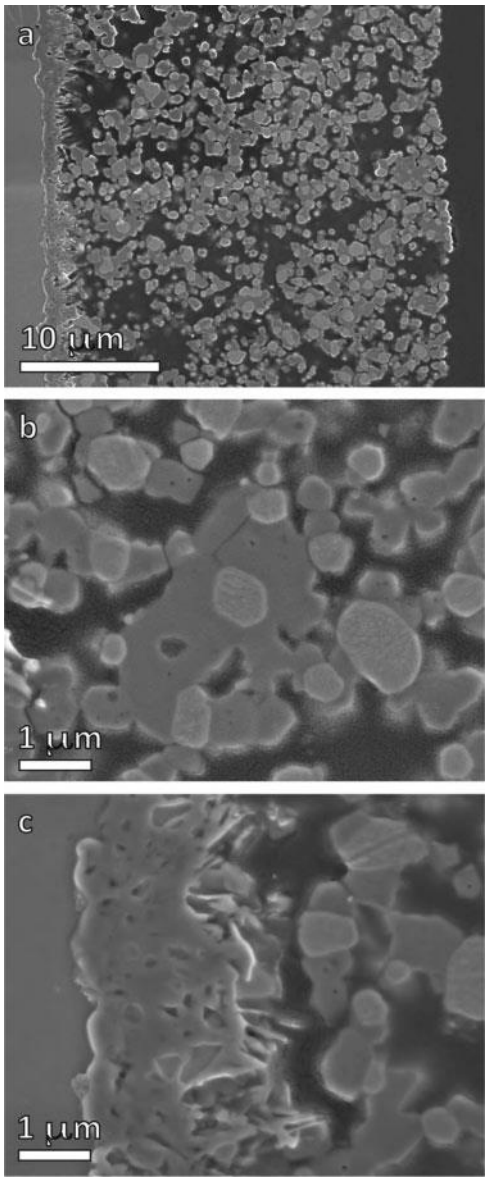

Figure 3.1: SE SEM images from metallographic cross-sections showing (a) full thickness of reduced coating from Crofer 22 APU substrate on left, to epoxy mount on right; (b) region in center of porous reduced MCO coating showing two distinct phases; (c) interface between Crofer 22 APU substrate and reduced MCO coating.

morphology of this layer is revealed in SE SEM images such as Figure 3.1(c), which was obtained at the same magnification as Figure 3.1(b). This layer seems to have a rather rough but abrupt interface with the alloy substrate. The layer is quite dense immediately adjacent to the substrate, exhibits increasing porosity (up to 8%) with distance from the interface, and adopts a needle- or plate-like morphology at the interface with the coating.

Further analysis of the microstructures in these regions was performed using TEM and STEM techniques. A selection of the TEM data from a FIB-cut cross-section through the center of the coating is shown in Figure 3.2. Figure 3.2(a) is a representative low-magnification bright field (BF) TEM image. Such images revealed that the coating is a two-phase mixture comprising equiaxed particles up to 1μm in diameter of a darker phase surrounded by agglomerated polyhedral particles of a brighter phase. A higher-magnification BF TEM image from one of these latter particles is shown in Figure 3.2(b). The particle is cuboidal and contains an internal cuboidal void whose faces are aligned with the external faces of the particle. The compositions of these phases were measured using EDXS and these data (not shown) indicate that the bright and dark phases are essentially MnO and Co, respectively. Selected area diffraction patterns were used to confirm the phase identification, and examples of zone-axis SADPs from the bright and dark phases are shown in Figures 3.2(c) and 3.2(d), respectively. Figure 3.2(c) corresponds to the [011] zone axis pattern for MnO with the face-centered cubic (FCC) NaCl-type structure. All of the other patterns obtained from this phase were consistent with this structure, although in each case the calculated lattice parameter (0.441nm) was slightly smaller than published values for stoichiometric MnO (0.448 nm [199]). Figure 3.2(d) could not be indexed to the usual hexagonal-close-packed (HCP) structure for Co, but instead corresponds to the $[\bar{1}12]$ zone axis

pattern for the high-temperature FCC allotrope of Co with a lattice parameter of 0.356 nm. All of the other patterns obtained from the Co-rich phase in the coating were also consistent with the FCC, rather than the HCP, structure. It is noted that the FCC Co particles closest to the deposit surface contained stacking faults, whereas those closer to the substrate did not.

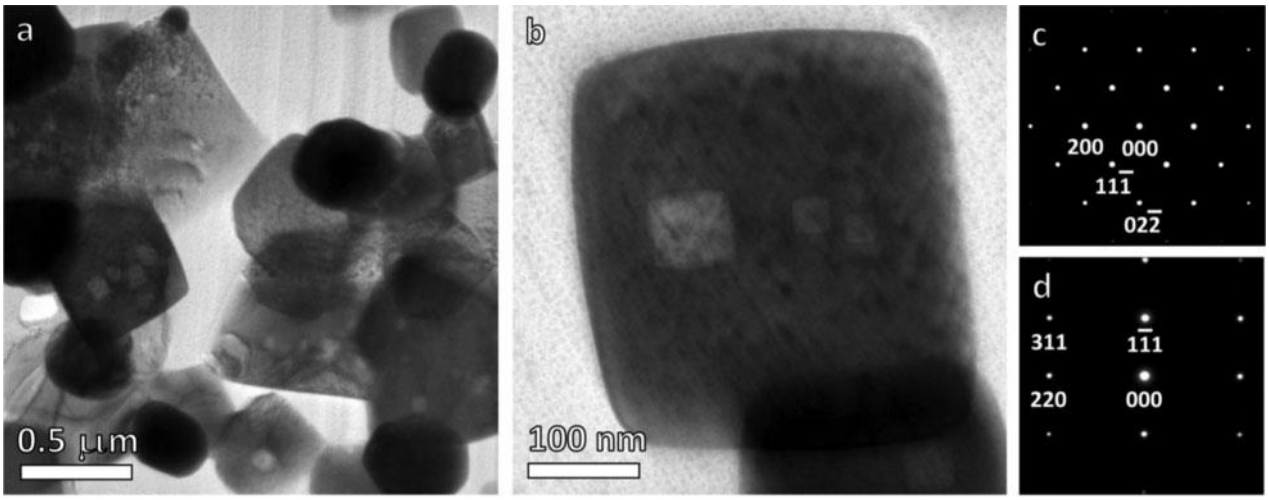

Figure 3.2: TEM data acquired from FIB cut cross-section through reduced MCO coating: (a) BF TEM image of polyhedral MnO particles bound together with smaller equi-axed Co particles; (b) higher magnification BF TEM image of MnO particle with faceted internal pore; (c) [011] zone axis SADP from MnO particle with NaCl structure; d [–112] zone axis SADP from a Co particle with FCC structure.

A montage of BF TEM images obtained from a FIB-cut cross-section through the alloy/coating interface is shown in Figure 3.3. The region in the upper left is the alloy substrate, and the region on the far right exhibits similar contrast to that found in the bulk of the coating (e.g. Figure 3.2(a)), but the contrast in the 2-3 µm thick layer between these zones is complex and could not be interpreted easily.

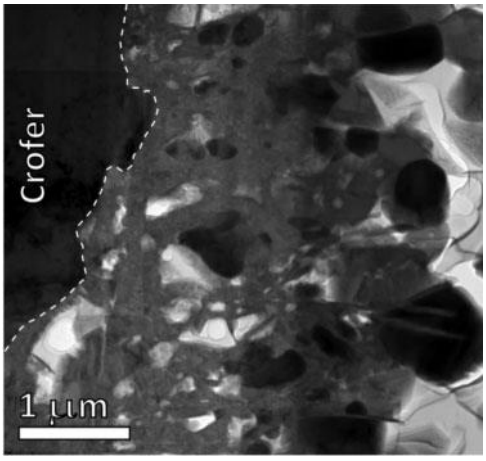

Figure 3.3: BF TEM image acquired from FIB cut cross-section through substrate/coating interface.

The details of this complex interfacial microstructure were revealed using STEM imaging and EDXS data; an example of one such analysis is shown in Figure 3.4. The Figure contains an annular dark field (ADF) STEM image and chemical maps for Cr, Fe, O, Mn and Co. Each map represents a grid of 256 x 200 measurements taken using a 100 eV window centered around the K- (or Kα-) peak for the relevant element. The data was acquired by scanning over the same region 2048 times with a dwell time at each point of 0.2 ms for a total acquisition time of around 5.8 h. Here again, the region on the left hand side is the Crofer alloy substrate. The measured alloy composition is approximately 78 at.% Fe and 22 at.% Cr although there is a 2-3 at.% depletion of Cr in the layer immediately adjacent to the interface. At the interface, there is a rough discontinuous layer 100-200 nm in thickness, which is enriched in Cr and O. The measured composition is approximately 40 at.% Cr and 60 at.% O, corresponding to Cr_2O_3. The ADF STEM image shows that the chromia grains in this layer range from 25 to 250 nm in diameter. Immediately beyond this layer is a RL region enriched in Cr, Mn and O. The measured composition of this RL is approximately equal to that expected for the Manganese Chromite spinel $MnCr_2O_4$, although there is a small amount (up to 2 at.%) of Fe throughout, and the Mn:Cr ratio changes with distance from the interface. At >1µm from the interface, the spinel RL forms protruding needles or laths with an average chemistry of $Mn_{1.35}Cr_{1.55}Fe_{0.1}O_4$. There are also occluded pockets of Fe/Co metal within the RL as revealed by dark patches in the Cr, Mn and O maps and corresponding bright patches in the Fe and Co maps. The ratio of Fe:Co in these regions varied between 7:1 and 1:1. Further from the interface on the right hand side there is a mixture of MnO, Co and infiltrated pore (i.e. epoxy) phases with the spinel protrusions between them. These can be distinguished in the Cr, Mn and O maps thus: MnO is

very bright in Mn, bright in O and dark in Co; Co is dark in Mn and O but very bright in Co; epoxy is very bright in O, but dark in Mn and Co. The Co phase in these areas also contains up to 10% Fe, although there is very little Fe in the FCC Co phase well away from the interface.

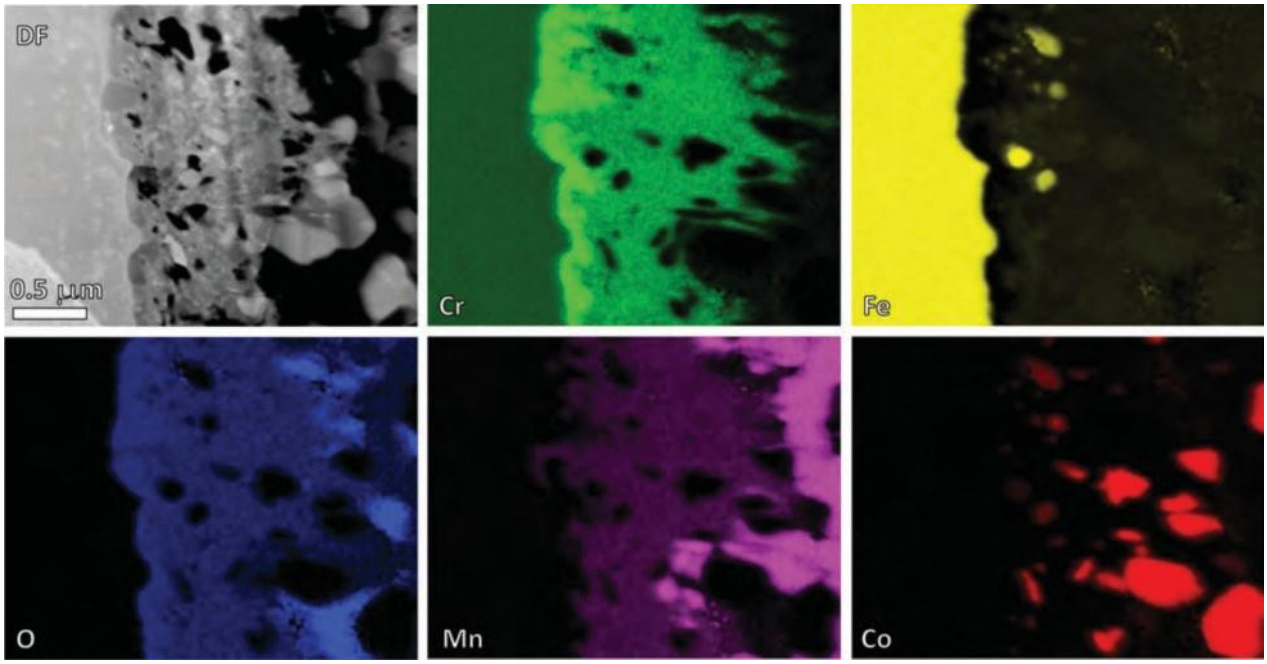

Figure 3.4: STEM data acquired from FIB cut cross-section through substrate/coating interface: DF image shows region analyzed; X-ray maps show integrated intensities in 100 eV windows centered on K and Ka1 peaks for Cr, Fe, O, Mn and Co.

The main features of the microstructure observations are summarized schematically in Figure 3.5. Going from left to right we have: the Crofer 22 APU alloy substrate; a rough abrupt interface with a dense chromia layer of variable thickness; a spinel RL with embedded Fe/Co-rich particles, increasing porosity with distance from the chromia layer, and a needle- or lath-like morphology at the interface with the porous coating; and a highly porous mixture of equi-axed metallic FCC Co and polyhedral MnO particles. The mechanisms behind the development of these features are discussed below.

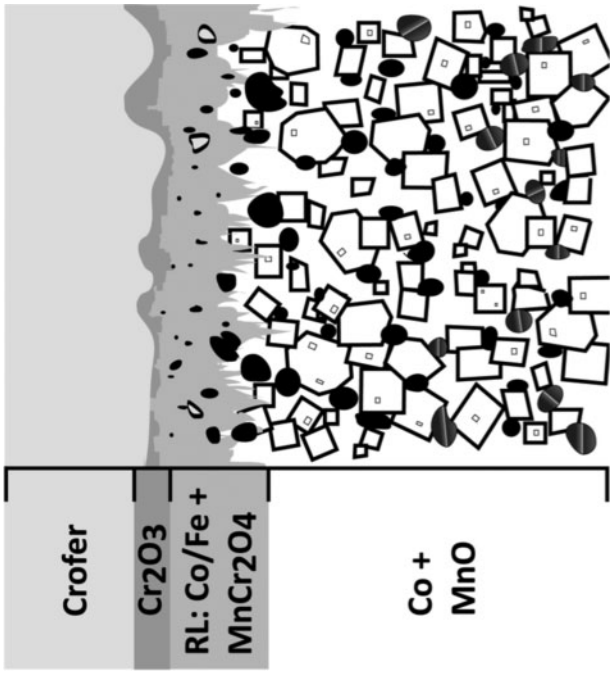

Figure 3.5: Schematic diagram showing main microstructural features in the coating after reduction process: RL contains Fe and Co rich metallic particles indicated in grey and black respectively; reduced coating includes defect free Co particles closer to substrate in black and faulted Co particles near surface in banded gray.

3.4 Discussion

As far as we are aware, there have been no previous TEM or STEM studies of microstructures in reduced slurry-processed MCO coatings, but the observations are broadly consistent with the findings of previous SEM studies in which a mixture of MnO and Co phases was reported [200, ,201]. At room temperature $Mn_{1.5}Co_{1.5}O_4$ forms a two-phase mixture comprising cubic $MnCo_2O_4$ and tetragonal Mn_2CoO_4 spinel phases [59, 200], although recent X-ray

and neutron diffraction studies [141] suggest that the stoichiometries, site occupancies and oxidation states are more complex than those implied by these chemical formulae. At the reduction temperature (850°C), however, $Mn_{1.5}Co_{1.5}O_4$ forms a single-phase cubic spinel, and thus the simplified reduction reaction is given by Equation 3.1.

$$2\ Mn_{1.5}Co_{1.5}O_4\ (s)\ +\ 5\ H_2\ (g)\ \rightarrow\ 3\ MnO\ (s)\ +\ 3\ Co\ (s)\ +\ 3\ H_2O\ (g) \qquad (3.1)$$

It has been shown previously[14] that if one assumes that the MCO is a cubic spinel with a_0 = 0.828 nm, Co is HCP with a_0 = 0.251 nm, c_0 = 0.407 nm and MnO adopts the NaCl structure with a_0 = 0.445 nm, then the above reaction would result in a reduction in the volume of the solid of ≈ 30%. While the Co phase observed here is FCC, not HCP, and the lattice parameter measured from MnO is slightly smaller (0.441 nm), these differences will not affect the expected reduction in volume significantly. The discrepancy between the calculated contraction of ≈ 30% and the observed porosity of ≈ 54% is presumably due to the initial porosity of the dried slurry. It is expected that initial porosity to be far greater than 24%, and thus there is presumably significant densification occurring during the reduction process. Indeed the porosity of the re-oxidized coating is only 20-25% and so most of the densification (as opposed to volumetric shrinkage or expansion due to reduction or oxidation, respectively) must occur during the reduction step rather than during the subsequent re-oxidation.

The MnO phase that forms during reduction appears to be highly defective with polyhedral internal voids and a lattice parameter smaller than that anticipated for normal variations in stoichiometry [199]. This suggests that the reduction occurs by outward diffusion of the Co, which is reduced to the metallic form at the particle surfaces, and that the resultant vacancy-rich Manganese oxide transforms to the NaCl structure with voids being formed by

vacancy agglomeration. The equilibrium allotrope of Co at the reduction temperature is FCC, but one might expect that this would transform to the low-temperature HCP structure upon cooling. This transformation might be inhibited by the size, morphology and/or low defect content of the Co particles, any of which could suppress the formation of the Shockley partial dislocations that mediate allotropic FCC to HCP transformations. Another possibility is suggested by the detection of low levels of Fe in the FCC Co particles. Onozuka *et al.* [202] have shown that additions of Fe to Co stabilize the FCC phase at room temperature for > 6 at. % Fe, and that the double-HCP (DHCP) structure forms for 1.5-6 6 at. % Fe. Thus the incorporation of Fe from the substrate into the Co phase could help to suppress the FCC to HCP (or DHCP) transformation, particularly close to the substrate where no stacking faults are observed. It is noted that FCC Co particles have also been observed by Brylewski *et al.* [203] in a reduced lanthanum strontium cobaltite coating on a chromia-forming Fe alloy.

The interfacial layers between the reduced coating and the Crofer substrate could have been anticipated. The partial pressure of oxygen within the tube furnace is approximately 10^{-17} atm, and under these conditions one would expect the oxidation of both metallic Cr and Mn within the alloy. The two interfacial layers observed (Cr_2O_3 plus $MnCr_2O_4$) are similar to those observed by us and by other authors in the scale on bare Crofer 22 APU oxidized in air at atmospheric pressure [204]. It has been established for bare Crofer, and other ferritic Fe-Cr-Mn stainless steels, that the chromia scale forms first. There is limited solubility of Mn_2O_3 in Cr_2O_3 (12-17 wt.%), and once this value is reached, $MnCr_2O_4$ spinel nucleates on the surface and grows via a reaction between Mn_2O_3 and Cr_2O_3 [57]. This reaction dominates the subsequent scale development because grain boundary diffusion of Mn in Cr_2O_3 is 1-2 orders of magnitude

faster than grain boundary diffusion of Cr or Fe [205]. There are other features of the interfacial layers that suggest that moisture may be playing a significant role. For example, it has been shown previously that H_2O reduces the porosity at the chromia scale interface [206], and can cause the formation of $MnCr_2O_4$ whiskers [90]; both of these features are evident in the interfacial layers observed here.

The metallic Fe-rich inclusions in the spinel layer are similar to those reported previously in the literature for similar alloy systems [128, 204, 207]. In these previous works the metallic inclusions are attributed to stresses that arise from internal oxidation of titanium or the formation of $MnCr_2O_4$ subscale pockets. Issartel *et al.* accounted for these stresses on the basis of the Pilling-Bedworth ratio for these internal oxidation reactions [207]. While this seems like the most likely reason for the Fe/Cr metallic inclusions observed in the previous work on oxidation of Crofer 22 APU [71,96], the inclusions observed here are markedly different in that they contain Co. Thus, it seems likely that there is concurrent growth of the $MnCr_2O_4$ spinel phase on the chromia and decomposition of the $Mn_{1.5}Co_{1.5}O_4$ spinel phase in the coating. This could lead to the incorporation of Co into the metallic Fe inclusions at the growth front for the $MnCr_2O_4$ spinel RL and a corresponding enrichment in Mn for the RL itself.

The complex variation that has been observed in the RL chemistry and morphology after re-oxidation and subsequent long-term exposure [71] could thus be explained on the basis of a reaction between the $Mn_{1.5}Co_{1.5}O_4$ coating and the $MnCr_2O_4$ interfacial layer observed here. There are Cr-rich protrusions that penetrate into the MCO coating in the re-oxidized condition, which are clearly a remnant of the needle-or plate-like morphology of the $MnCr_2O_4$ layer in the as-reduced condition. Over time the site preferences for the various cations will

drive diffusion of each of these species in particular directions, leading to the eventual formation of a steady-state RL of constant composition. Thus, the character of this steady state RL, the rate at which it forms, and the eventual thickness may all depend upon the cations present and the sites that they occupy in the spinel structure. For example, Wang et al. have shown that the presence of Fe within the RL may impede the outward diffusion of Cr from the alloy [188]. Further studies on the site occupancies in these microstructural layers and in model ceramic spinels of the same compositions are underway to investigate these effects.

3.5 Conclusions

An electron microscopy study was performed on the effect of a reduction heat treatment at 850 °C in moist H_2-based forming gas on the microstructure of a Crofer 22 APU substrate coated with a $Mn_{1.5}Co_{1.5}O_4$ slurry. The key findings of this study were:

1. The reduction process converted the $Mn_{1.5}Co_{1.5}O_4$ spinel to a porous mixture of MnO and Co phases. The MnO phase exhibited the usual NaCl structure, but was highly defective with internal voids and a smaller lattice parameter than the stoichiometric structure. The Co phase exhibited the high-temperature FCC structure, possibly stabilized by the presence of Fe.

2. There is a concurrent oxidation of the Crofer substrate surface with a thin dense chromia scale and a more porous $MnCr_2O_4$ interfacial layer with needle- or lath-like features protruding into the coating. There is some evidence of reaction between the MnO+Co mixture and the interfacial layers, with Co-rich metallic pockets in the spinel layer and an enrichment in the Mn content of the spinel with distance from the chromia layer.

These observations help to explain the peculiar microstructural development observed previously for $Mn_{1.5}Co_{1.5}O_4$-coated Crofer 22 APU after re-oxidation and subsequent high-temperature exposure.

3.6 Future Work

The reactive sintering process results in a much denser MCO coating than can be achieved with low temperature sintering in air [53, 59, 70, 71]. Further consolidation of MCO coatings may be achieved by running several reduction and re-oxidation cycles by flowing moist H_2 based forming gas and air through a tube furnace at 850 °C. This consolidation technique has proven to be successful for LSM-based contact pastes for SOFCs [249, 250]. Future work may be performed to show the extent of consolidation and reaction layer development of MCO coatings with each thermal cycle.

Chapter 4:

ALCHEMI Studies of Site Occupancies in

Cr-, Ni- and Fe-substituted Manganese Cobaltite Spinels

4.1 Introduction/Preamble

Normal spinels are AB_2O_4 compounds with tetrahedrally coordinated A sites occupied by divalent cations and octahedrally coordinated B sites occupied by trivalent cations [175, 208]. The extent of the cation ordering across the A and B sites can depend on the cation size [140], the energy of the s and p orbitals [157], and the temperature [209]. A variety of different experimental techniques have been used to determine the cation site occupancies in spinels including: X-ray diffraction [210], neutron diffraction [211], magnetization saturation [212], and Mössbauer spectroscopy [213]. The common drawback of all of these techniques is that they provide volumetric average or "bulk" measurements and thus simple, single-phase samples are required. For example, the cation site occupancies in MCO [73] and $Mn_{0.4}Co_{0.6}Cr_2O_4$ [141] powders have been determined by co-refinement of X-ray and neutron diffraction data. To obtain an acceptable fit for the structural data, the MCO powders had to be specially processed to achieve single-phase materials [162], and even then there were complications in determining the cation site occupancy with accuracy due to the multiple oxidation states that the Mn and Co cations can adopt. There was even greater uncertainty in the cation site occupancies for the

ternary compound because of the need to assign a constraint for the refinement of more than two cations [141].

Atomic Location by CHanneling Enhanced MIcroanalysis (ALCHEMI) is a transmission electron microscopy (TEM) technique for the measurement of site occupancies in crystals using X-ray or electron spectrometry. In this technique the electron beam is aligned with a channeling orientation in the crystal, and the site occupancies are determined from the variation in apparent composition due to differences in the ionization cross sections for the sub-lattices [214-218]. One of the main advantages of the ALCHEMI approach is that analyses can be performed on small crystals selected using the focused electron beam allowing for site occupancies to be studied in complex multi-phase materials. While ALCHEMI analyses have been performed on a variety of different spinels [219-224], to the author's knowledge there has not been any previous ALCHEMI studies on site occupancies in MCO-based materials. This study used combustion synthesis to produce a series of ceramic powders in which Cr, Fe, and Ni have been substituted into MCO as models for the spinel reaction layers formed on MCO-coated SOFC interconnect alloys. ALCHEMI studies have been performed on sintered compacts of these powders to measure the site occupancies for each of the cations. These findings are compared with the results of previous X-ray and neutron diffraction studies on MCO-based spinels, and with early thermo-physical analyses of cation site preferences, to infer the likely consequences for reaction layer development.

4.2 Materials and Methods

A series of transition metal (TM) substituted MCO spinel ceramic pellets was produced for this study; these materials had the general formula $(Mn,Co,TM)_3O_4$, where TM = Cr, Fe or Ni. For each of the TM additions, a series of three $Mn_{1.5-x}Co_{1.5-x}TM_{2x}O_4$ samples was produced with different TM contents: 2x = 0.5, 1.0 and 1.5, referred to as Low, Medium and High TM contents, respectively. For the Cr series only, samples with different Mn and Co contents were also produced: $Mn_{2x}Co_{1.5-x}Cr_{1.5-x}O_4$ and $Mn_{1.5-x}Co_{2x}Cr_{1.5-x}O_4$ with 2x = 0.5 and 1.5 in each case. These thirteen different compositions are summarized in Table 4.1.

Table 4.1: Nominal molar composition of the 13 Cr-, Ni-, and Fe-substituted MCO samples.

Cr-substituted	*Low Cr:* $Mn_{1.25}Co_{1.25}Cr_{0.5}O_4$		*High Cr:* $Mn_{0.75}Co_{0.75}Cr_{1.5}O_4$
	Low Co: $Mn_{1.25}Co_{0.5}Cr_{1.25}O_4$	*Med. Cr/Mn/Co:* $Mn_1Co_1Cr_1O_4$	*High Co:* $Mn_{0.75}Co_{1.5}Cr_{0.75}O_4$
	Low Mn: $Mn_{0.5}Co_{1.25}Cr_{1.25}O_4$		*High Mn:* $Mn_{1.5}Co_{0.75}Cr_{0.75}O_4$
Ni-substituted	*Low Ni:* $Mn_{1.25}Co_{1.25}Ni_{0.5}O_4$	*Med. Ni:* $Mn_1Co_1Ni_1O_4$	*High Ni:* $Mn_{0.75}Co_{0.75}Ni_{1.5}O_4$
Fe-substituted	*Low Fe:* $Mn_{1.25}Co_{1.25}Fe_{0.5}O_4$	*Med. Fe:* $Mn_1Co_1Fe_1O_4$	*High Fe:* $Mn_{0.75}Co_{0.75}Fe_{1.5}O_4$

Powders of each composition were synthesized using the glycine nitrate process (GNP), which involves a highly exothermic combustion reaction between glycine (fuel) and metal nitrates (oxidizer) to produce an oxide ash [225]. The precursors glycine (99%), manganese(II) nitrate tetrahydrate (98%), cobalt(II) nitrate hexahydrate (97.7% min), chromium(III) nitrate nonahydrate (98.5%), iron(III) nitrate nonahydrate (ACS, 98.0-101.0%), and nickel(II) nitrate hexahydrate (98%) were purchased from Alfa Aesar. For each sample, the nitrate salts were mixed in proportions that would give the appropriate cation ratio upon complete conversion to

spinel oxide. The proportion of glycine required to give a stoichiometric redox reaction was then calculated using the net oxidizing and reducing valences in each reagent [226]. In preliminary trials using such stoichiometric glycine/nitrate mixtures there was incomplete conversion of the nitrates suggesting that there is significant glycine loss during the process. Fuel-rich mixtures containing 250% of the stoichiometric amount of glycine gave full conversion, and such mixtures were used for all of the materials described in this study.

In each oxide synthesis, a stock solution was produced from the glycine/nitrate mixture by adding sufficient de-ionized water to dissolve the powders and stirring until a clear solution was obtained. For the combustion reaction, 40 mL of the stock solution was placed into a 4 L stainless steel beaker, and the beaker was covered with a 230 stainless steel mesh to contain the ash. Heat was applied to the beaker using a Bunsen burner causing the solution to convert to a viscous liquid which then boiled, auto-ignited, and underwent a self-sustaining combustion reaction. The resulting oxide ash was then calcined at 850°C. Both the ash and the calcined powders were checked for residual metal nitrates and/or glycine using Fourier Transform Infrared Spectroscopy (FTIR) with a Nicolet Magna 560 spectrometer. X-ray diffraction (XRD) with a Bruker 5005 diffractometer was also used to check the phase purity.

Pellets were prepared with 10 g of calcined spinel powder and 1 g of 10% polyvinyl acetate in H_2O. Pellets were formed under a low load of 4000 psi in a floating die with an internal diameter of 25 mm, cold isostatically pressed at 27000 psi, sintered at 1000°C for 10 hours, and then cooled at 100°C per hour to room temperature. The resultant sintered pellets had a thickness of approximately 10 mm.

TEM specimens were obtained from the spinel pellets by: cutting slices 0.5 mm in thickness using a SiC abrasive disc saw; extracting 3 mm diameter discs using an ultrasonic disc cutter; dimpling to a minimum central thickness of 50 μm; and Ar ion milling to perforation at an accelerating voltage of 4 kV in a Gatan DuoMill. All ion milling was performed using a liquid N_2 cold stage to minimize ion beam damage. The ALCHEMI experiments were performed on a FEI Tecnai T12 TEM operating at 120 kV and equipped with an EDAX ultra-thin window energy-dispersive X-ray spectrometry (EDXS) system.

4.3 Results

To demonstrate the approach taken in these analyses, the data presented first is from the Medium Cr/Mn/Co sample from the Cr-substituted series (i.e. the sample with a nominal molar composition of $MnCoCrO_4$). The XRD data from both the calcined oxide powder (Figure 4.1(a)) and the sintered pellet of this composition are consistent with this being a single-phase cubic spinel material; after correction for instrumental errors, the value obtained for the lattice parameter, a_0, from these data was 0.8469 nm. A typical SE SEM image obtained from a section through the sintered pellet is shown in Figure 4.1(b). Such images reveal the equi-axed grains and pores in the sample clearly. The diameters of the spinel grains range from 0.2 – 1.0 μm and the porosity of this sample is estimated at 28 % by comparing the density of the pellet to the theoretical density for a cubic spinel with this lattice parameter and composition. The overall composition of the sample was measured by obtaining EDXS spectra at non-channeling orientations. The spectra exhibited very little point-to-point variation, as one might expect for a homogeneous single-phase sample. Standard-less quantification performed on these data using

the thin film approximation gave an overall cation composition of 34 % Mn, 33.7 % Co and 32.3% Cr. This is close to the nominal composition and corresponds to a Mn:Co:Cr molar ratio of 1.02:1.01:0.97 (i.e. the spinel is $Mn_{1.02}Co_{1.01}Cr_{0.97}O_4$).

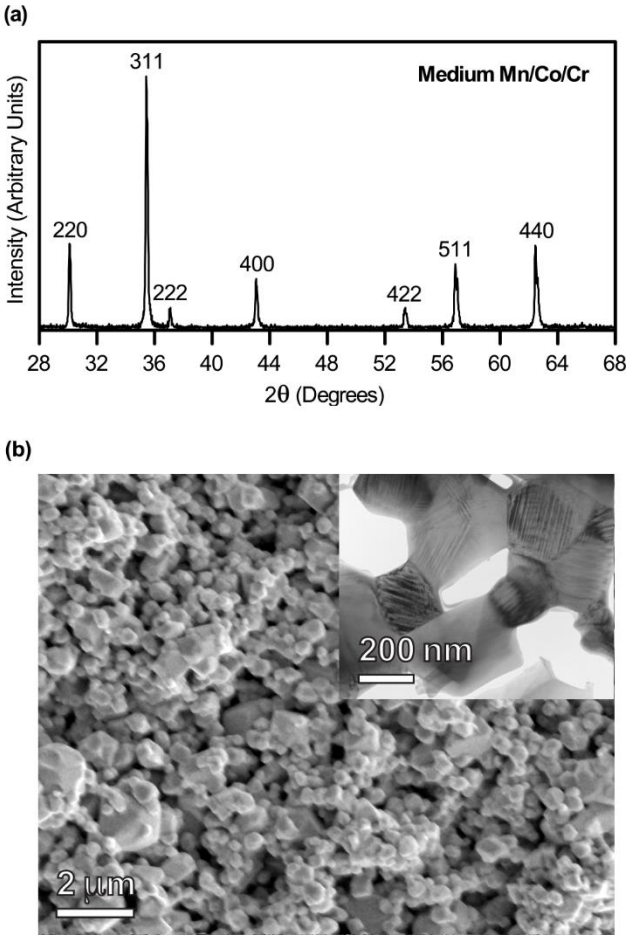

Figure 4.1: Microstructure of the Medium Mn/Co/Cr sample: (a) XRD data obtained from the calcined oxide powder showing the cubic spinel structure; b) SE SEM image of a section through the sintered pellet, with a BF TEM image inset.

Following previous ALCHEMI studies on cation site ordering in spinels [215, 223, 224], EDXS channeling data were obtained using the "planar ALCHEMI" configuration for orientations along the 400 systematic row. In this approach the grain of interest is tilted to a 400 two-beam condition well away from any zone axis; EDXS data are then obtained at different values of the deviation parameter to reveal the effects of channeling on the apparent composition. A [001] projection of the normal cubic spinel structure is shown in Figure 4.2(a). This reveals the alternating layers of A and B sites on the {400} planes, with oxygen lying in the same layers as the B sites. To reveal the effects of channeling, planar ALCHEMI data were obtained from a large grain in the Medium Cr/Mn/Co sample by tilting away from the two-beam condition *perpendicular* to [100] in increments of approximately 0.05°

to vary the deviation from the Bragg condition for the {n00} planes systematically. The apparent compositions obtained from the EDXS data by standard-less quantification are shown in Figure 4.2(b). The orientations are plotted on the abscissa with “000” being the symmetry condition, “400” being the Bragg condition for the (400) planes, and so on. For reference, the mean Mn, Co and Cr contents as percentages of the total cations are indicated by the horizontal bars on the left of the Figure. At the symmetry condition, the deviation parameter, *s*, is negative for both (400) and ($\bar{4}$00) and the apparent Co content is much lower than the mean, whereas the Mn and Cr contents are much higher. For orientations to the right of the Bragg position for (400), where *s* is positive for (400) but large and negative for ($\bar{4}$00), the apparent Co content is higher and the Mn and Cr contents are lower. Similar effects are seen to the left of the Bragg position for ($\bar{4}$00), where *s* is positive for ($\bar{4}$00) but large and negative for (400), although there is some asymmetry due to sample geometry effects. These data clearly show that Mn and Cr are strongly correlated, and that they are anti-correlated with Co. By comparing these observations with previous studies of site occupancies in spinels [140, 157, 175, 208], it is inferred that the Mn and Cr tend to occupy the B sites with Co on the A sites.

The site occupancies in such three-component systems are represented most clearly using the ordering tie line (OTL) construction introduced by Hou et al [227]. The OTL is a graphical approach based on the principle that in any ordered system the mean composition is a weighted average of the sub-lattice compositions. Thus, if the compositions of the two sub-lattices in a ternary system are plotted on a compositional triangle, then the mean composition will lie on the tie line connecting these points. Moreover, in the absence of any complications such as delocalization effects, any apparent compositions measured in channeling experiments

must also lie on the tie line. This approach has been used in ALCHEMI studies in a variety of alloy, intermetallic and oxide systems [228-232], but not to the best of the author's knowledge in any previous studies of site occupancies in spinels. The OTL for the data from Figure 4.2(b) is shown in Figure 4.2(c): each of the apparent compositions is plotted in an Mn-Co-Cr compositional triangle; the best-fit OTL is constructed using orthogonal distance linear regression; and the end points are then identified as the most highly ordered state possible given the overall composition and the sense of the ordering implied by the slope of the OTL. In this case the coefficient of determination, R^2, is 0.998 indicating that the ALCHEMI data give an excellent fit to the OTL indicated. The end points of the extrapolated OTL lie at (12% Mn, 88% Co) and (45% Mn, 6.5% Co, 48.5% Cr); this corresponds to a $(Mn_{0.12}Co_{0.88})_A(Mn_{0.9}Co_{0.13}Cr_{0.97})_BO_4$ spinel. It has been shown that the strength of the channeling in an ALCHEMI experiment, *S*, is equal to the length of the tie line segment spanning the measured apparent compositions divided by the total length of the tie-line between the actual sub-lattice compositions [217]. Since the actual sub-lattice compositions cannot be determined unambiguously, the tie-line end points are used to obtain $S = 0.25$. It is noted that this is a lower bound on *S* since the ordering may not be as strong as that implied by the calculated end points. Moreover, even this lower bound of 0.25 is considered a very strong channeling effect since the maximum possible value of S is only 0.3-0.5 depending on absorption effects [217].

Figure 4.2: EDXS ALCHEMI data from the Medium Mn/Co/Cr sample: (a) schematic [010] projection of the cubic spinel structure showing the alternating sheets of A and B/O ions parallel to {100}; (b) variation in apparent cation composition with specimen orientation; (c) OTL plot showing the best fit tie line with end points corresponding to the most highly ordered state.

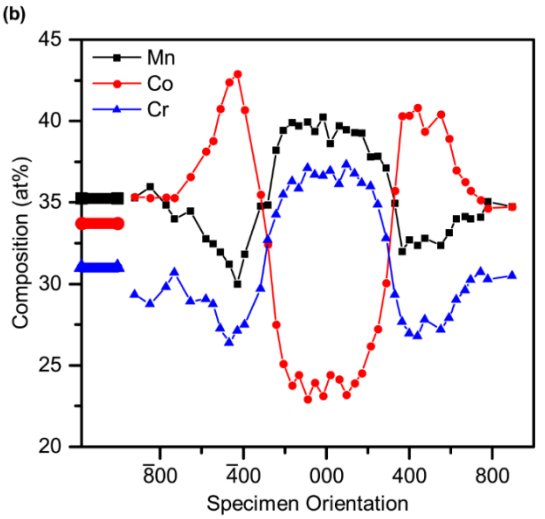

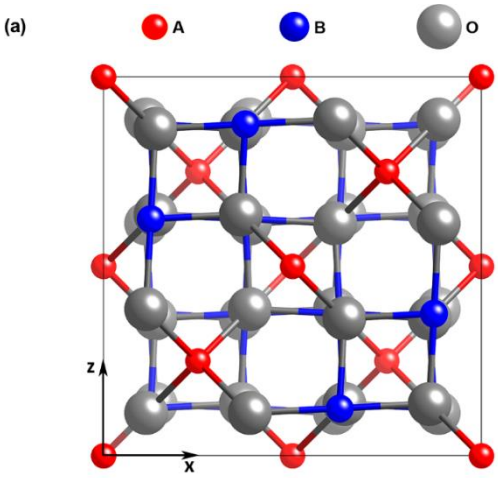

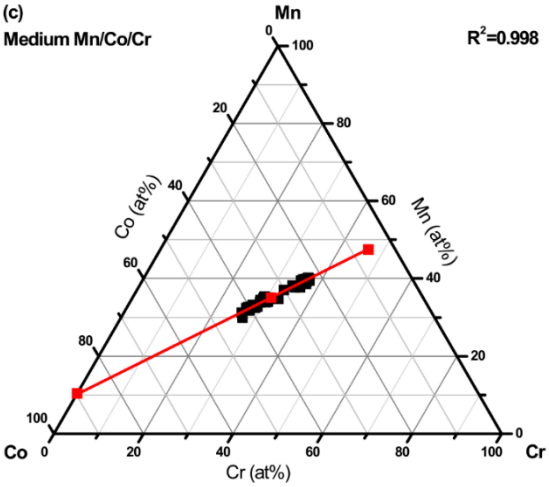

A similar approach was used to analyze the other 12 samples. The XRD data from the other 6 Cr-substituted samples are shown in Figure 4.3. The Low Mn, Low Co, High Co and High Cr samples all appear to be single-phase cubic spinels, and the corresponding values of a_0 are given in Table 4.2. The High Mn sample is also single-phase but exhibits the tetragonal $CoMn_2O_4$ structure; this is a tetragonal distortion of the cubic spinel structure giving a change in symmetry from $Fd\bar{3}m$ to $I4_1/amd$ [234]. The axes of this tetragonal structure are rotated by 45° about [001] with respect to the parent cubic structure so that $a_0' \approx a_0\sqrt{2} \approx c_0$, where a_0' is the

equivalent cubic lattice parameter; the values of a_0 and c_0 are given in Table 4.2. The Low Cr sample exhibits a mixture of the cubic and tetragonal structures, which is similar to that observed previously for MCO samples with the composition $Mn_{1.5}Co_{1.5}O_4$ [71, 162, 200]. The XRD peaks from this sample were significantly broader than those from the other samples, presumably due to some combination of grain size and/or defect content, and so it was not possible to determine the lattice parameters accurately. The overall cation compositions of the samples measured by EDXS at non-channeling orientations are also included in Table 4.2. In each case, these were very close to the nominal compositions for the samples.

Table 4.2: Summary of data from the six Low/High Mn, Co and Cr samples in the Cr-substituted series. Phase(s) and Lattice parameters are from XRD data. Mean cation compositions are from EDXS data obtained at non-channeling orientations. Sub-lattice compositions, coefficients of determination (R^2) and channeling strength (S) were obtained from OTL plots of EDXS ALCHEMI data.

	Phase	Lattice Parameter (nm)	Mean Cation Composition (%)			A Sub-Lattice (%)			B Sub-Lattice (%)			R^2	S
			Mn	Co	Cr	Mn	Co	Cr	Mn	Co	Cr		
Low Mn	C	a_0 - 0.8329	19.2	38.5	42.3	4.0	96.0	0	26.8	9.7	63.5	0.997	0.24
High Mn	T	a_0 - 0.5845 c_0 - 0.8787	51.5	24.2	23.3	31.3	68.7	0	61.5	2.1	36.4	0.992	0.23
Low Co	C	a_0 - 0.8418	42.9	15.7	41.4	49.1	47.2	3.7	39.7	0	60.3	0.999	0.22
High Co	C	a_0 - 0.8321	26.9	48.3	24.8	1.7	98.3	0	39.6	23.3	37.2	0.999	0.24
Low Cr	C + T	*	42.4	41.2	16.4	0	97.3	2.7	63.6	13.2	23.2	0.996	0.21
High Cr	C	a_0 - 0.8400	25.4	25.6	49.0	25.8	74.2	0	25.2	1.3	73.5	0.999	0.27

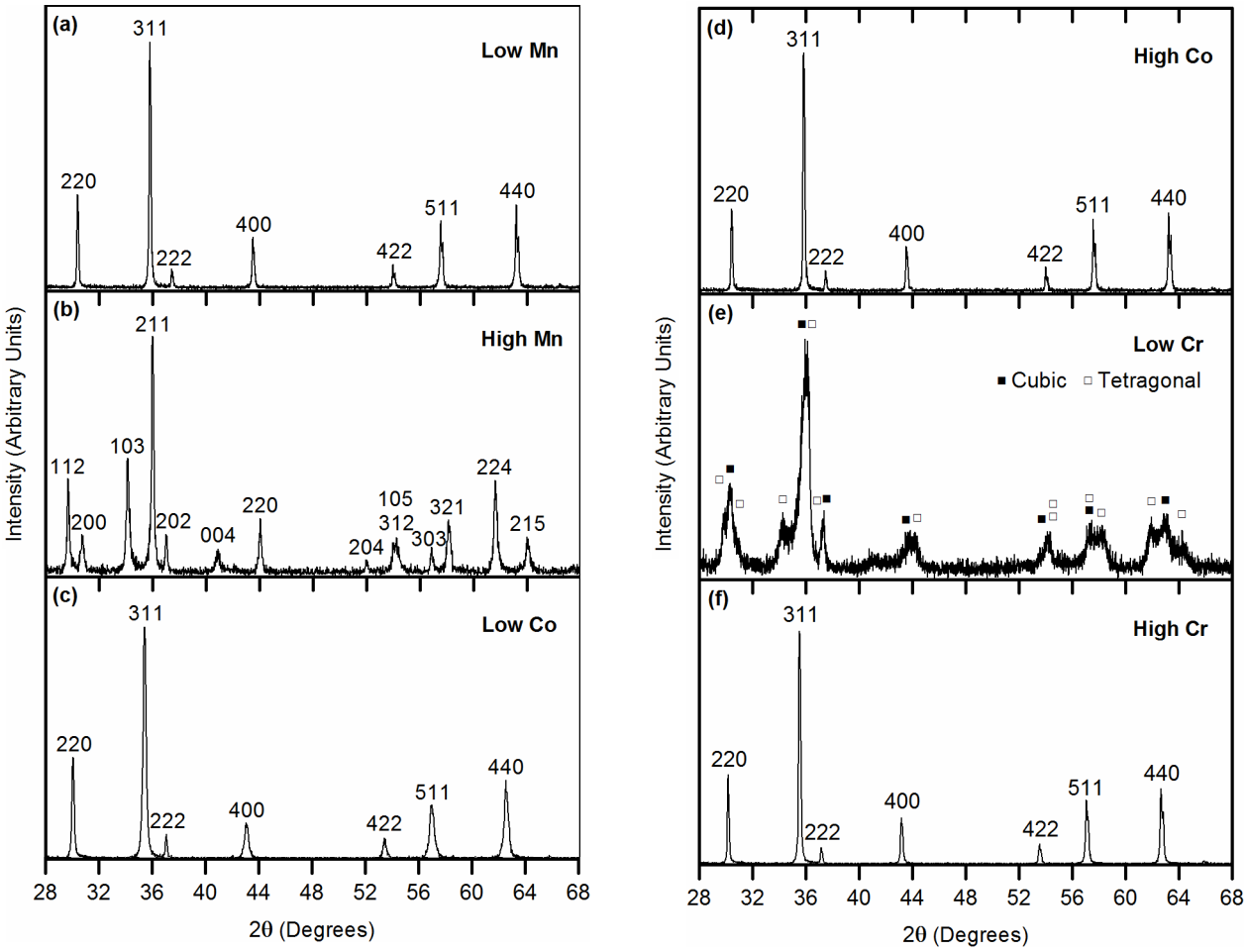

Figure 4.3: XRD data obtained from the calcined oxide powder for six Cr-substituted samples: (a) Low Mn; (b) High Mn; (c) Low Co; (d) High Co; (e) Low Cr; (f) High Cr.

Examples of OTL plots from each of these samples are presented in Figure 4.4. In each case, these correspond to data with R^2 > 0.99 from a single grain in the sample, although several such experiments were performed for each sample and each gave similar results. The compositions of the tie-line end-points, and the values of R^2 and S are given in Table 4.2. In the Low Mn sample (Figure 4.4(a)), the OTL is oriented similarly to that for the Medium Cr/Mn/Co sample (Figure 4.2(c)), and here again the Co resides mainly on the A sites with Cr and Mn on the B sites. In the High Mn sample (Figure 4.4(b)), the data were acquired at deviations from the 220 systematic row for the tetragonal structure, which is equivalent to the 400 row for the parent cubic structure. Here again, the slope of the OTL is similar, indicating that the same site preferences prevail, with Co on the A sites and Cr on the B sites. In this case, however there are more Mn ions than can be accommodated on the remaining B sites and approximately 30% of the A sites are occupied by Mn in the most highly ordered state. The same Co and Cr site preferences are evident for the Low Co sample (Figure 4.4(c)), resulting in an OTL with a rather different orientation; at this composition there are more Mn ions on the A sites than Co ions. The OTLs for the High Co and Low Cr samples (Figure 4.4(d) and (e)) again resemble those for the Low Mn and Medium Cr/Mn/Co samples (Figure 4.2(c)), but in these cases the A sites are occupied almost exclusively by Co and there is also a significant Co content on the B sites. It is noted that no significant differences in overall or sub-lattice compositions were measured between the cubic and tetragonal phases in the Low Cr sample. Thus, the data from a cubic grain in Figure 4.4(e) are representative of both phases. In the High Cr sample the OTL orientation resembles that for the Low Co sample, with the Co on the A sites, the Cr on the B sites, and the Mn distributed evenly across the A and B sites.

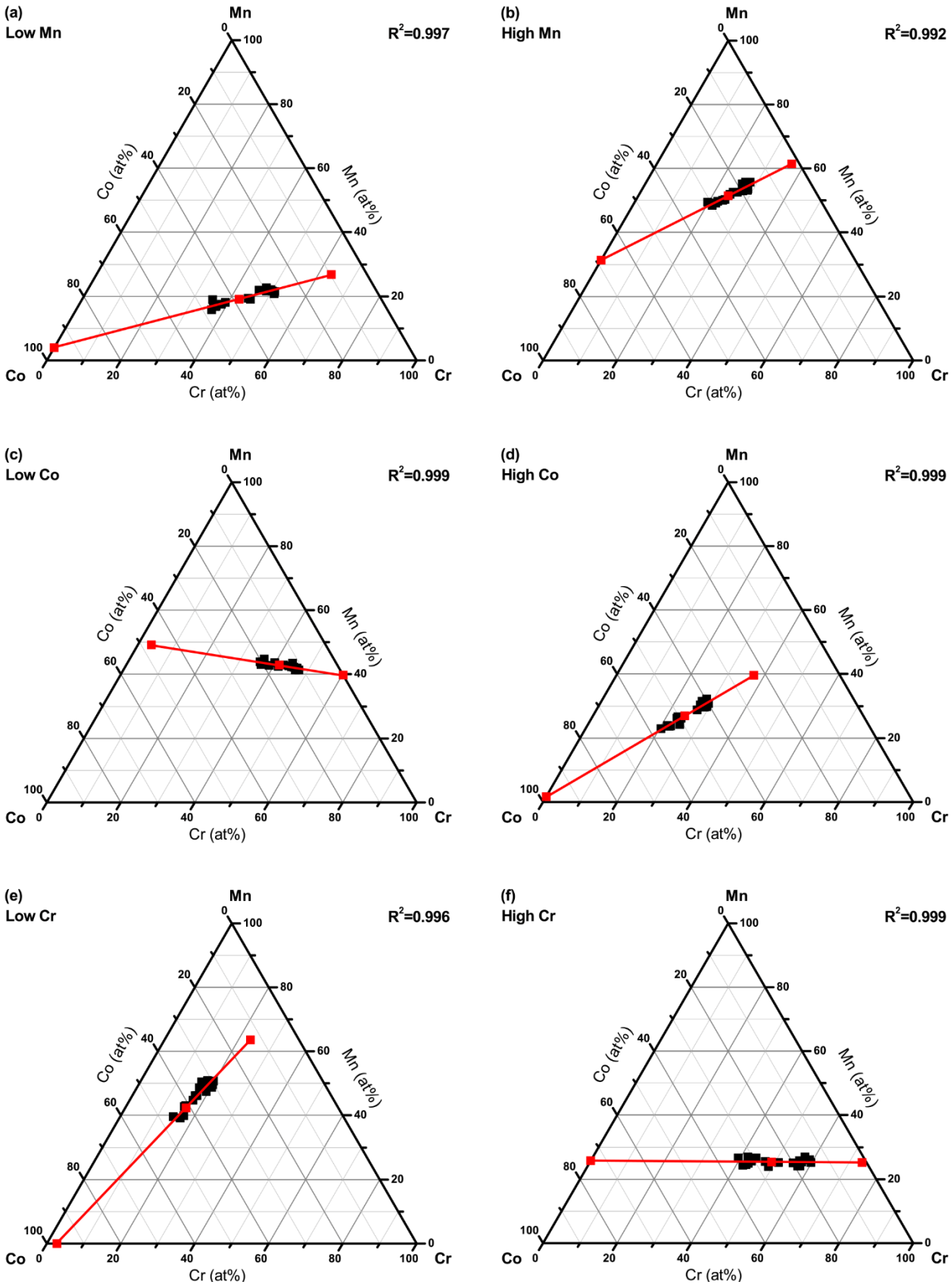

Figure 4.4: OTL plots obtained from sintered samples of six Cr-substituted samples: (a) Low Mn; (b) High Mn; (c) Low Co; (d) High Co; (e) Low Cr; (f) High Cr.

The XRD data from the three Ni-substituted samples are shown in Figure 4.5. All three samples show the cubic spinel phase, and the corresponding values of a_0 are given in Table 4.3. For the Medium and High Ni samples, there are also peaks corresponding to cubic NiO with the rock-salt structure; the lattice parameters for these phases were 0.4201 and 0.4180 nm, respectively. The mean cation compositions of the spinel phases measured by EDXS are given in Table 4.3, whereas the cation compositions for the rock-salt phases were 1 % Mn / 22 % Co / 77 % Ni, and 1 % Mn / 14 % Co / 85 % Ni in the Medium and High Ni samples, respectively. Due to the porosity it is not possible to measure the volume fractions of the rock-salt phase accurately, but by using a mass balance approach they are estimated to be 20% and 37%, respectively. It is noted that the presence of the rock-salt phase in these two samples leads to a larger deviation of the spinel from the nominal composition of the overall sample than in the Cr-substituted samples. Examples of OTL plots from each of these samples are presented in Figure 4.6. In each case the OTLs are oriented similarly, indicating that Co tends to occupy the A sites with Mn and Ni on the B sites. For both the Low and the Medium Ni samples, however, about 10% of the A site cations are Mn and approximately 17% of the B site cations are Co.

Table 4.3: Summary of data from the spinel phase in three Ni-substituted samples.

	Phase	Lattice Parameter (nm)	Mean Cation Composition (%)			A Sub-Lattice (%)			B Sub-Lattice (%)			R^2	S
			Mn	Co	Ni	Mn	Co	Ni	Mn	Co	Ni		
Low Ni	C	a_0 - 0.8327	41.6	42.5	15.9	10.5	89.5	0	57.2	18.9	23.9	0.997	0.31
Med. Ni	C	a_0 - 0.8311	41.4	39.9	18.7	11.6	88.4	0	56.1	15.8	28.1	0.998	0.21
High Ni	C	a_0 - 0.8321	39.5	34.8	25.7	2.3	97.7	0	58.1	3.3	38.6	0.997	0.22

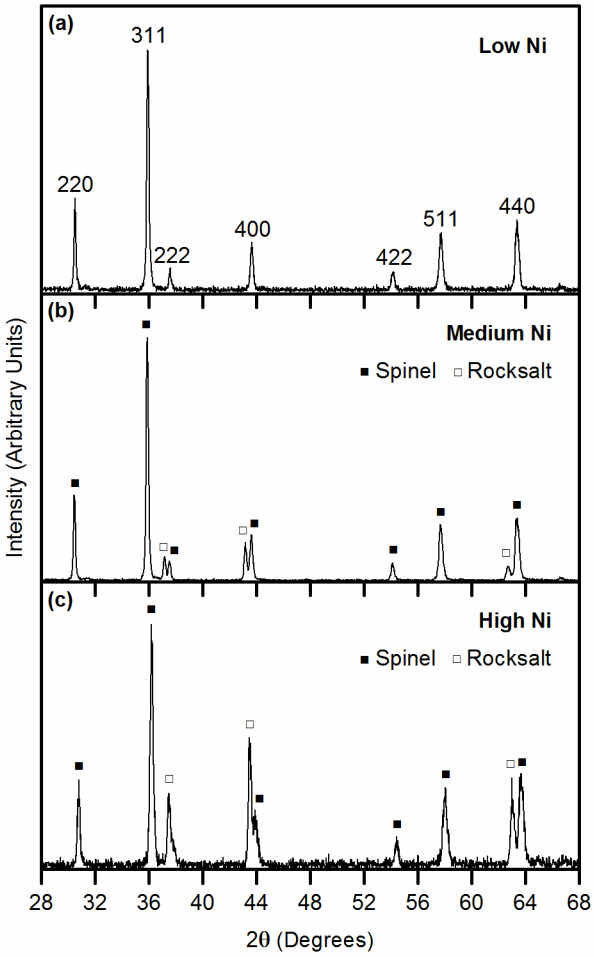

Figure 4.5: XRD data obtained from the calcined oxide powder for the three Ni-substituted samples:
(a) Low Ni; (b) Medium Ni; (c) High Ni.

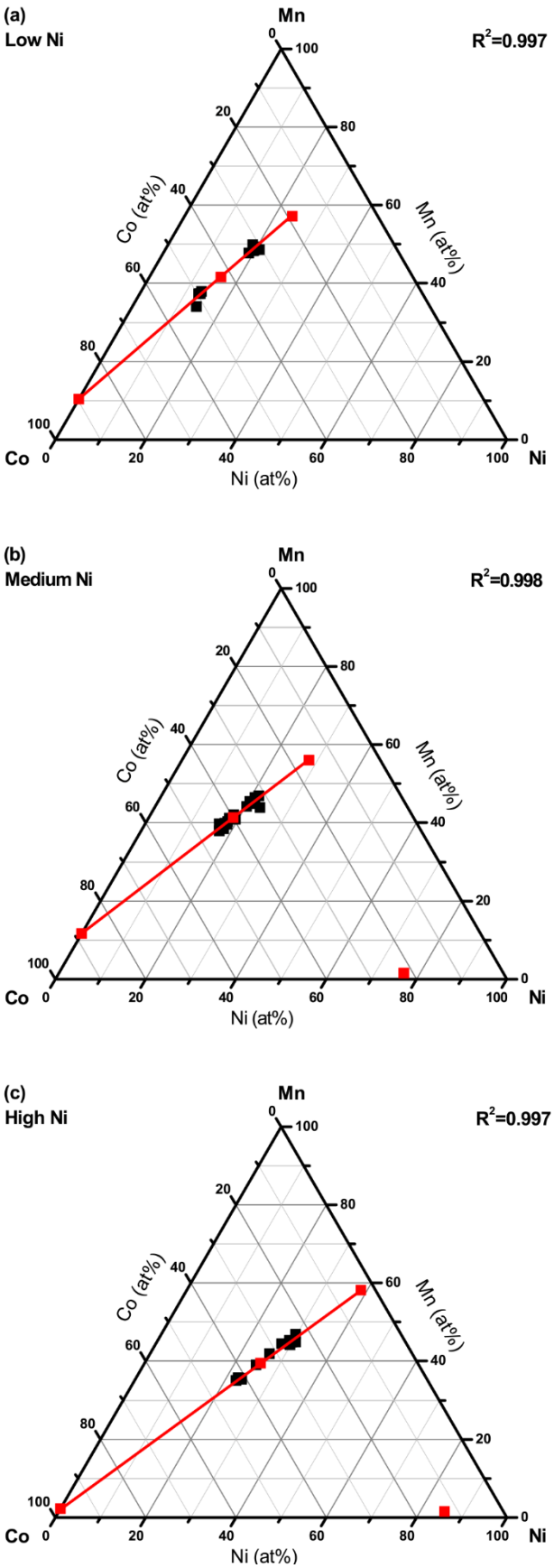

Figure 4.6: OTL plots obtained from sintered samples of the three Ni-substituted samples: (a) Low Ni; (b) Medium Ni; (c) High Ni.

The XRD data from the three Fe-substituted samples are shown in Figure 4.7. For the Low and Medium Fe samples, there appears to be a mixture of tetragonal and cubic phases, although in this case the magnitude of the tetragonal distortion appears to be smaller than in the Low Cr sample which showed the same phase mixture (Figure 4.3). Here again, the broadening and overlap of the peaks from the two phases precluded the accurate measurement of lattice parameters. In the High Fe sample, however, there was only a single cubic phase with a_0 = 0.8439 nm. The mean cation compositions of the spinel phases measured by EDXS are given in Table 4.4. The values for the Low Fe sample deviate significantly from the nominal composition. Occasional grains were observed with higher Fe and Mn, and lower Co, so this deviation could be due to phase separation in a similar manner to the Medium and High Ni samples. The cation compositions for the Medium and High Fe samples were much closer to the nominal values. Representative OTL plots from each of the Fe-substituted samples are shown in Figure 4.8, and the end-point compositions are given in Table 4.3. The OTL orientations for the Low and Medium Fe samples indicate that Co occupies the A sites, Mn occupies the B sites, and Fe is distributed evenly across the two types of sites. The values of R^2 and S are lower for the Medium Fe sample than for the Low Fe sample, suggesting that increasing the Fe content reduces the strength of ordering in these materials. Indeed for the High Fe sample there is no measureable channeling effect suggesting that the distribution of all three cations is uniform across the A and B sites.

Table 4.4: Summary of data from the spinel phase in three Fe-substituted samples.

	Phase	Lattice Parameter (nm)	Mean Cation Composition (%)			A Sub-Lattice (%)			B Sub-Lattice (%)			R^2	S
			Mn	Co	Fe	Mn	Co	Fe	Mn	Co	Fe		
Low Fe	C+T	*	34.9	51.6	13.5	0	92.8	7.2	52.3	31.0	16.7	0.999	0.24
Med. Fe	C+T	*	31.8	34.3	33.9	0	66.0	34.0	47.7	18.5	33.8	0.976	0.20
High Fe	C	a_0 - 0.8439	24.5	26.4	49.2	-	-	-	-	-	-	0	0

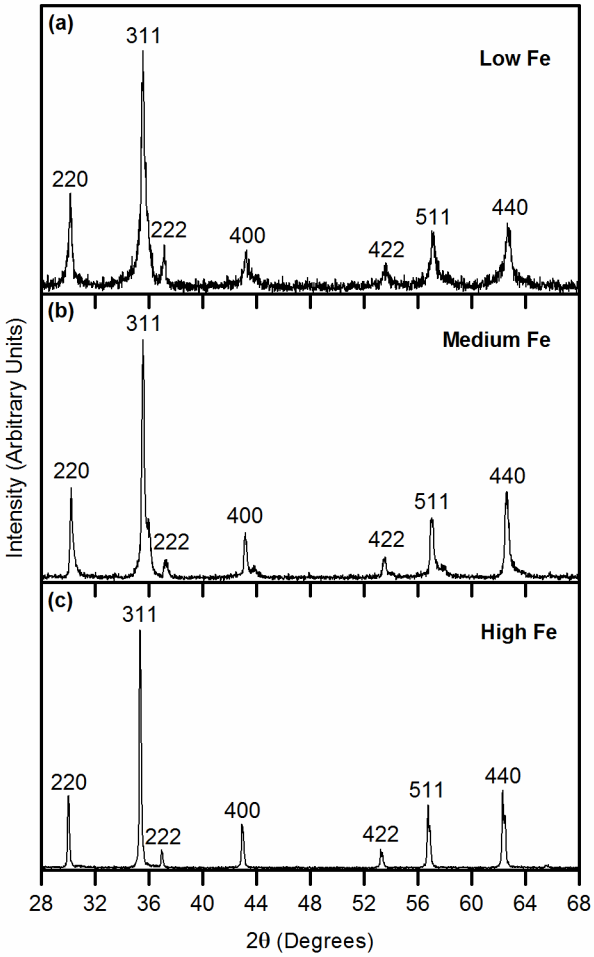

Figure 4.7: XRD data obtained from the calcined oxide powder for the three Fe-substituted samples:
(a) Low Fe; (b) Medium Fe; (c) High Fe.

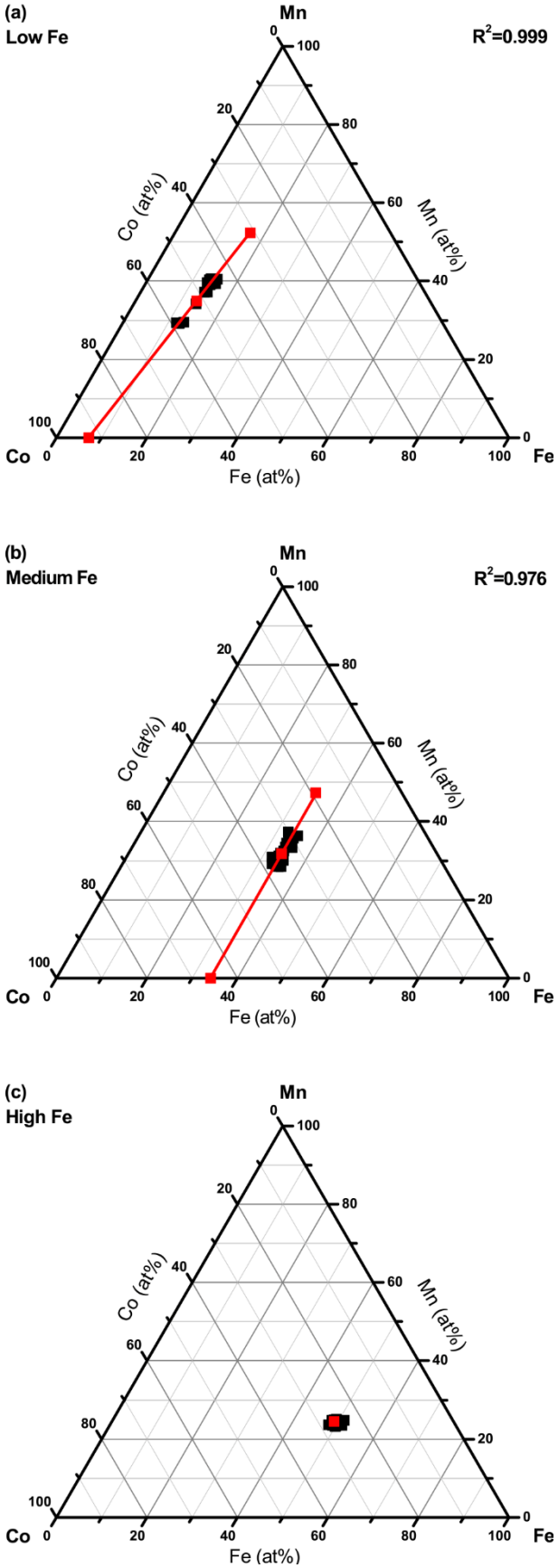

Figure 4.8: OTL plots obtained from sintered samples of the three Fe-substituted samples: (a) Low Fe; (b) Medium Fe; (c) High Fe.

4.4 Discussion

With the exception of the High Fe sample, the ALCHEMI data obtained in this study give particularly high values of R^2. This suggests that the experimental conditions used to acquire the data have been optimized well and that there is very little effect from electron delocalization, as one might expect for an oxide structure such as a spinel. While the ALCHEMI technique can only measure the sense of the ordering in such systems, not the degree of order, the OTL plots do suggest that the ordering must be very strong in these samples. The values of *S* obtained from the ALCHEMI data are ≥0.2 in all but the High Fe case. These are *lower bound* estimates of *S* based on the OTL end points corresponding to the most highly ordered state possible for each sample. There are various issues associated with the samples that could influence the values of *S*. For example, lattice defects that perturb the structure locally can reduce the strength of the channeling effect [235]. More general cation disordering in spinels can also occur due to ion or electron irradiation displacing ions from their equilibrium locations [223, 224]. Thus, during ion beam milling for TEM specimen preparation or during examination under the electron beam the degree of ordering on the cation sublattices could be reduced from that which prevails in the sintered ceramic pellets. Moreover, depending on the thermal history, the cation distributions in the pellets might not represent the equilibrium state (e.g. [236]), although the cooling of the pellets at 100°C/h was designed to minimize this effect. It is noted, however that each of these effects would reduce the degree of order and/or the strength of the resulting channeling effect. Thus the large values of *S* obtained experimentally suggest that the tie-line end points are a good approximation to the true sub-lattice compositions, and these compositions are used for the remainder of this discussion.

Three main approaches have been used to quantify the site preferences for cations in spinels. Traditionally, this was done by considering ionic size effects and Madelung constants [153, 237], but this was largely superseded by crystal field theory [155] and subsequent refinements using pseudo-potential orbital radii [157]. In an alternate approach due to Navrotsky *et al*., sophisticated calorimetric measurements were used to determine the interchange enthalpy for cations between tetrahedral and octahedral sites [140, 160]. While there cannot be a quantitative measure of site preferences extracted from the ALCHEMI data, the measurements do provide a clear rank of site preferences in the samples. In the following discussion, these preferences are compared with those expected for spinels on the basis of the study by Navrotsky and Kleppa [160], which includes results from both calorimetric measurements and crystal field theory.

Firstly, the OTLs from the Cr-substituted samples (Figure 4.2(c) and Figures 4.4(a)-(f)) are considered. As explained in the results section, these OTLs indicate that to within the experimental uncertainty: all of the Cr resides on the octahedral B sites; all of the Co resides on the tetrahedral A sites, except for in the Low Mn, Low Cr and High Co samples where the A sites are occupied by Co only and the excess Co goes to the B sites; and the Mn resides in the unoccupied B (and, where appropriate, A) sites. The strong preference of Cr for B sites is to be expected since in both crystal field theory calculations and calorimetric approaches Cr^{3+} has the highest B site preference energy of all the cations considered [160]. The strong preference of Co for the A sites is less straightforward; the empirical site preference energy of Co^{2+} for these sites from calorimetric measurements has the appropriate sign but a significantly smaller magnitude, and the value from crystal field theory has the opposite sign suggesting that Co^{2+}

would go to B sites. The situation is complicated further for Mn since there are two common oxidation states in spinels: Mn^{3+}, which shows a strong preference for the B sites, and Mn^{2+}, which shows a weaker preference for the A sites.

In the Ni-substituted samples, all of the Ni resides on the B sites. Here again this is consistent with both crystal field theory calculations and calorimetric approaches, which give a high B site preference energy for Ni^{2+} (i.e. these are inverse, or partially inverse spinels). In the High Ni sample, all of the Co lies on the A sites with all the Mn on the B sites, but for both the Low and the Medium Ni samples about 10% of the A site cations are Mn and 17% of the B site cations are Co. These trends are complicated somewhat by the presence of a significant volume fraction of NiO in the latter two samples, giving large deviations of the spinel compositions from the nominal compositions of the two ceramic pellets. It is noted, however, that the OTL orientations are the same in each case suggesting that the relative site preferences are the same.

The Fe-substituted samples exhibit rather different trends, with all of the Mn on the B sites in the Low and Medium Fe samples, roughly equal proportions of Fe on the A and B sites, and Co distributed across the remaining sites. It is tempting to speculate that the presence of Fe leads to Mn adopting only the 3+ oxidation state, since one would expect Mn^{3+} to have a strong preference for the B site. The calorimetry approach suggests that Fe, like Mn, exhibits an oxidation-state dependent site preference, although in this case Fe^{2+} has a weak preference for the B site and Fe^{3+} having a somewhat stronger preference for the A site [160]. It is also important to note that the degree of order decreases with increasing Fe content, with the High Fe sample exhibiting no channeling evidence for preferred site occupation.

An obvious weakness of the EDXS ALCHEMI approach is that it gives the location of the different species on the sublattices, but provides no information on the oxidation states. This is a severe limitation in systems such as MCO spinels since the cations can exhibit different oxidation states. Indeed since MCO is a small polaron conductor, the Mn ions must exhibit mixed oxidation states, and the conductivity of the oxide will depend upon the relative populations of the ions. An attempt was made to determine the oxidation states of the cations from the measured lattice parameters by calculating the oxygen displacement parameter (e.g. [140]) for different distributions of oxidation states using published values for the cation radii and the site occupancies measured experimentally. The differences between the lattice parameters calculated for the oxidation state models were within the experimental uncertainty in the measured values of a_0, and so no conclusions could be reached on this basis. The oxidation states of the cations could be evaluated by electron energy-loss spectroscopy (EELS) in the TEM using the white lines and/or other near-edge structure on the L_{23} ionization edges (e.g. [238, 239]). Moreover, the acquisition of EELS spectra at channeling orientations would allow data to be acquired with different contributions from the cation sub-lattices thereby revealing differences in oxidation state [240]. We are currently exploring the use of such EELS ALCHEMI approaches to study oxidation state distributions in MCO and related spinels.

Lastly, it is noted that these observations could have important consequences for reaction layer formation during elevated temperature exposure of MCO-coated stainless steels and superalloys, such as those observed in our recent studies [70, 71, 201, 241]. In pure MCO, Mn tends to reside preferentially in the B sites. Diffusion of Cr and/or Ni from the alloy substrate into the coating will tend to displace Mn from the B sites, and will presumably change

the balance of Mn oxidations state and therefore the conductivity. No clear link has been established yet between changes in the cation distributions and in the polaronic conductivity in these coatings. It is noted however that preliminary EDXS ALCHEMI data obtained from cross-sectional TEM specimens of MCO coatings on Crofer 22 APU substrates have shown that the site occupancies in the reaction layer correspond closely to those measured here for the sintered ceramic MCO samples [242].

4.5 Conclusions

Cation site occupancies have been studied by EDXS ALCHEMI in a range of ceramic spinels based upon MCO ($Mn_{1.5}Co_{1.5}O_4$) with different levels of Cr, Ni and Fe substitution on the cation sublattices. Analysis of the ALCHEMI data using the OTL approach enables the sub-lattice cation compositions to be determined for the most highly ordered state consistent with the overall sample composition and the sense of the ordering measured experimentally. In most cases the channeling is sufficiently strong to suggest that the samples exhibit these most highly ordered states. Thus, the main findings are as follows:

1. In Cr-substituted samples, all of the Cr ions lie on the octahedral B sites. The Co resides on the tetrahedral A sites, except when the Co content is high enough to completely fill the A sublattice and any excess Co goes to the B sites. The Mn occupies the remaining sites.

2. In Ni-substituted samples all of the Ni ions reside on the B sites. The Co and Mn ions tend to lie on A and B sites, respectively, although there is some mixing of Co onto B sites and Mn onto A sites at lower Ni contents.

3. In Fe-substituted samples with low to intermediate Fe contents, all of the Mn lies on the B sites, with roughly equal proportions of Fe on the A and B sites, and Co distributed across the remaining sites. The degree of order decreases with increasing Fe content, with the High Fe sample exhibiting no channeling evidence for preferred site occupation.

These observations could have important consequences for conductive MCO coatings on high temperature alloys. The diffusion of Cr, Ni and/or Fe into the coating to form an interfacial reaction layer could cause profound changes in the local site occupancy, cation oxidation state(s) and degree of ordering in the spinel leading to structural and functional differences within the reaction layer.

4.6 Future Work

The EDXS ALCHEMI study of MCO-based spinel ceramics has set the groundwork for using this technique to study the RLs formed between interconnect alloys and MCO-based coatings. Preliminary results have shown success with using this technique to measure the cation site occupancy in RLs formed in MCO coated Crofer 22 APU despite the complex microstructure, high concentration of defects, and composition gradient through individual grains [242]. Further ALCHEMI work needs to be performed to identify the effect that Ni- and Fe- substitution in MCO coatings have on rate of chromia scale growth and RL development.

Since it is the oxidation state of the cations across the A and B sublattice which determines the structure and properties of spinel, EELS ALCHEMI experiments are necessary to explain the principles which affect the performance of interconnect RLs. Published EELS ALCHEMI studies on spinel ceramics have shown the viability of this technique to measure the

oxidation state of Mn, Co, Fe, and Ni cations, although there were some difficulties with radiation damage [251, 252, 253]. EELS ALCHEMI can be used to explore how Ni- and Fe-substitution in MCO coatings affect the cation transport and conductivity of the RLs, since the oxidation state of the cations determines their diffusion path and the number of charge carriers. EELS ALCHEMI may also be used to determine if there is a difference in the oxidation state of the cations between the cathode and anode SOFC environment and with and without an applied voltage.

Chapter 5:

Microstructural Evolution in Manganese Cobaltite Films Grown on Crofer 22 APU Substrates by Pulsed Laser Deposition

5.1 Introduction/Preamble

Here a study is reported on the use of pulsed laser deposition (PLD) to produce MCO coatings on Crofer 22 APU substrates. While physical vapor deposition techniques are inherently less scalable than the slurry-based reactive consolidation process, they do offer the possibility of forming more uniform and much denser coatings. Such coatings are of interest as model systems to help study microstructural development in the coating phases, and might be practical for certain small-scale niche SOFC systems. There have been a few previous reports on the use of PLD to grow perovskite films [51, 52] and $MnCr_2O_4$ spinel films [52] onto interconnect alloys, but as far as is known this is the first reported use of PLD to deposit MCO. A combination of X-ray diffraction (XRD) and electron microscopy techniques have been used to reveal the details of the microstructures in as-deposited films and in films after post-deposition oxidation heat-treatment. The implications of these observations for the microstructural development in this system are discussed.

5.2 Materials and Methods

The PLD was performed using a ceramic $Mn_{1.5}Co_{1.5}O_4$ spinel target 25 mm in diameter and 10 mm in thickness. This target was produced by: synthesizing powders of this composition utilizing the glycine nitrate process [243]; cold pressing in a floating die to form a disc-shaped compact; cold isostatic pressing to increase green density; and then pressure-less sintering to give a final porosity of ≈30%. The details of the process are given in Section 4.2. The phase purity of the target was confirmed using Raman spectroscopy and X-ray diffraction (XRD) and no phases other than the tetragonal Mn_2CoO_4 and cubic $MnCo_2O_4$ spinels were detected.

Films were deposited onto Crofer 22 APU substrates cut from a cold-rolled sheet 200 μm in thickness. Preliminary experiments revealed profound orientation effects due to defects and/or crystallographic texture at the substrate surface. Thus, for all of the experiments presented here, the substrate was polished mechanically and then electrolytically in an aqueous mixture of sulfuric and chromic acids at 50°C. The combined effect of these polishing processes was to remove a surface layer of approximately 50 μm in thickness.

Deposition was performed using a Coherent Inc. Lambda Physik: Compex 201 KrF pulsed excimer laser (λ = 248 nm). The deposition conditions used were: pulse energy of 190 mJ, laser fluence of 1 J/cm^2, repetition rate of 5 Hz, pulse length of 25 ns, chamber pressure of 2.8×10^{-4} mTorr N_2, target/substrate distance of 80 mm, and a deposition time of 2.5 h. Prior to deposition the substrate was heated to 400°C from the back using a cartridge heater with the temperature monitored using an attached thermocouple. During deposition the substrate temperature was kept constant, and both the target and substrate were rotated to ensure uniformity of the thickness and composition in the deposits. Some of the deposits were

subjected to post-deposition annealing *ex situ* at 800°C for 0.5 and 14 h in a tube furnace at atmospheric pressure in laboratory air.

The structures of the as-deposited and the annealed films were characterized using XRD with a Bruker 5005 diffractometer. The XRD spectra were acquired by scanning over the angular range 2θ = 15° to 120° at a scan speed of 25 s/step with a step size of 0.02° using Cu Kα radiation with a monochromator. The morphologies of the films were evaluated by secondary electron (SE) imaging using the electron columns of FEI Strata 400S and Helios Nanolab G3 dual beam FIB instruments. These instruments were also used to perform site-selective sample preparation for transmission electron microscopy (TEM). The procedure used was to deposit protective Pt layers over the region of interest using first the electron beam and then the Ga^+ ion beam. Trenches were then cut through the deposits and into the underlying substrates, the lamellae between the trenches were then lifted out and mounted onto copper Omni grids. A scanning transmission electron microscopy (STEM) detector and flip-stage were used for final thinning. Ga^+ beam currents were reduced iteratively to a value of 9.7 pA during final milling to avoid excessive Ga^+ implantation and beam damage. The resulting samples were examined in FEI Tecnai T12, JEOL 2010 and FEI Talos F200X TEMs operating at accelerating voltages of 120, 200 and 200 kV, respectively.

5.3 Results

5.3.1 As-Deposited Films

The as-deposited films were firstly analyzed by XRD. Data such as those shown in Figure 5.1(a) contain two main sets of peaks: those corresponding to the BCC structure of the ferritic Crofer substrate and a second set from the deposit. The relative intensities of the BCC peaks varied from one location to another on the sample because the grain size at the surface of these electro-polished substrates (20 μm) is comparable to the collimated X-ray beam diameter used. The peaks from the deposit were not those expected for the spinel structure of MCO, but instead corresponded to a face-centered cubic lattice with a lattice parameter, a_0, of 0.4388 nm. This value of a_0 lies between those for CoO (0.4267 nm) and MnO (0.4442 nm), both of which exhibit the rock-salt structure (space group $Fm\bar{3}m$). In certain XRD scans where the Crofer grains were oriented such that the intensity of the 110_{BCC} peak was unusually low, there were small shoulder peaks that were subsequently shown to be from metallic Co as described below. An example of this is shown in the inset to Figure 5.1(a).

The surface morphology of the as-deposited film was investigated using SE imaging and a typical image is shown in Figure 5.1(b). The contrast in such images was fairly uniform suggesting that the films are relatively smooth, although there were subtle differences in contrast from one region to another. Since energy-dispersive X-ray spectrometry (EDXS) data obtained from such regions showed no differences in chemical composition, it seems likely that these contrast effects correspond to variations in the details of the deposit surface topography from one substrate grain to another.

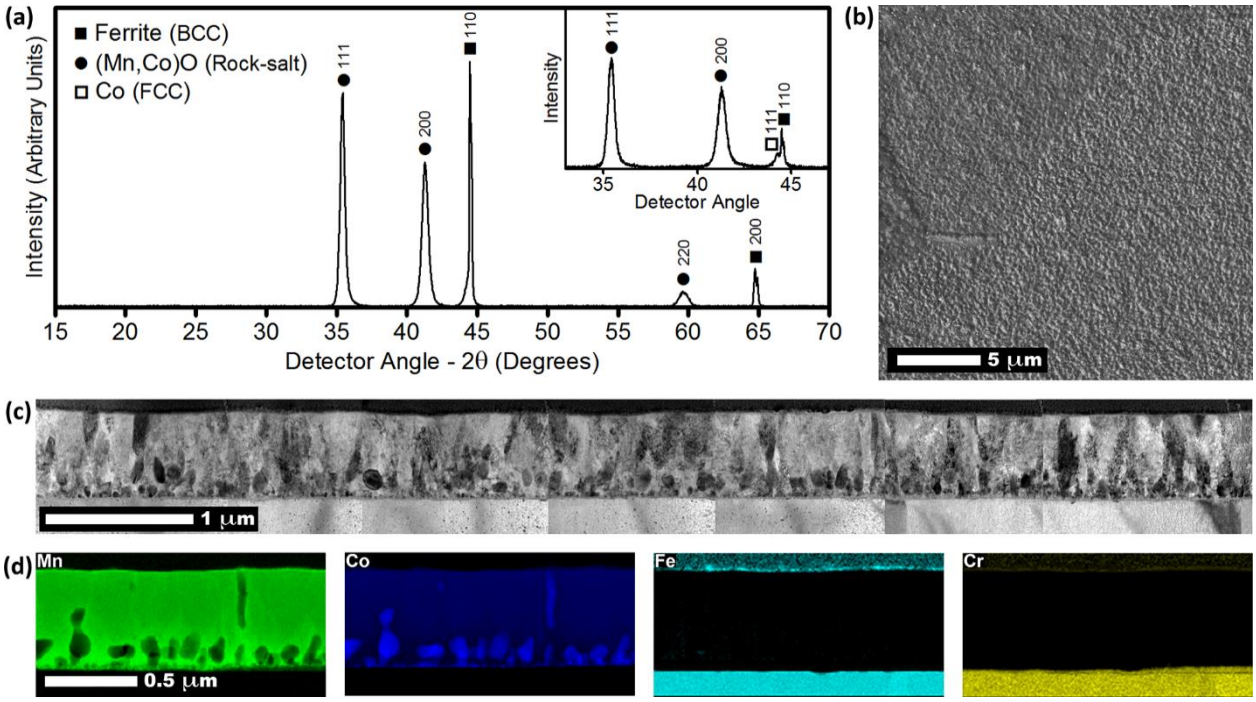

Figure 5.1: Overall microstructure of the as-deposited film: (a) XRD data with data from a second area on the same sample inset; (b) SE SEM image obtained from the deposit surface; (c) montage of BF TEM images obtained from a FIB-cut cross-section through the deposit; (d) maps showing the distribution of Mn, Co, Fe and Cr in a region of the sample shown in (c).

A montage of BF TEM images obtained from a FIB-cut cross-section through the deposit is shown in Figure 5.1(c). Such images confirm that the film is smooth and uniform with a deposit thickness of 680 ± 14 nm. The film exhibits a columnar microstructure throughout most of the thickness, with a mean grain width of 95 ± 37 nm measured parallel to the film/substrate interface. There are more equi-axed dark features in the regions adjacent to the deposit/substrate interface. The mean dimensions of these features measured parallel and perpendicular to the deposit surface are 57 ± 19 nm and 132 ± 78 nm, respectively. The character of these latter features was investigated by EDXS STEM experiments, and this is revealed most clearly in maps such as those shown in Figure 5.1(d). Data was acquired from the region of interest by collecting full spectra at each point in a 150 x 75 point grid. This spectrum

image was analyzed by performing a standard-less quantification for Mn, Co, Fe, Cr and O (not shown) at each point. Thus the maps shown in Figure 5.1(d) are compositional maps (rather than raw X-ray maps) and the intensity in these maps is proportional to the content of the corresponding elements. The maps indicate that: the majority of the film is a mixed Mn/Co oxide, presumably (Mn,Co)O, with some variation in the Co content with deposit thickness; the darker features are essentially pure Co; and there is a very thin layer of oxide (9 - 35 nm thick) at the interface that is enriched in Cr. Overall trends in composition were evaluated by integrating the compositional measurements over the whole film, and over the top, middle and bottom thirds of the film thickness. These data are given in Table 5.1.

Table 5.1: Average cation composition in film (atomic %).

	As-deposited		**0.5 Hour**		**14 Hour Dense**			**14 Hour Porous**		
	Mn	**Co**	**Mn**	**Co**	**Mn**	**Co**	**Cr**	**Mn**	**Co**	**Cr**
Whole film	50	50	50	50	49	46	5	50	47	3
Top third	50	50	49	51	46	52	2	43	51	6
Middle third	52	48	51	49	60	40	0	56	44	0
Bottom third	47	53	50	50	40	46	14	51	45	4

Further details of the as-deposited microstructure are shown in Figure 5.2. By comparing the high-angle annular dark field (HAADF) STEM image in Figure 5.2(a) with the data in Figures 5.1(a) & (d) and Table 5.1, it shows that:

- the film immediately below the protective Pt cap is columnar $Mn_{0.5}Co_{0.5}O$ with the rock-salt structure

- the center of the film is still single-phase oxide with the rock-salt structure, but is more Mn-rich
- near the substrate there is a mixture of metallic cobalt and very Mn-rich NaCl-type oxide. The mean volume fractions of the phases in the film were estimated by summing the projected area fractions in several HAADF images such as Figure 5.2(a), and the values obtained for Co and (Mn,Co)O were 0.17 and 0.83, respectively.

Higher magnification TEM images reveal further details of the interface structure. Figure 5.2(b) is a BF TEM image that shows a much smaller Co grain just above the interface, and indeed there seems to be a bimodal distribution of Co grain sizes, with the fine cobalt grains being equi-axed with mean diameters of 22 ± 8 nm. Figure 5.2(c) is a phase-contrast lattice image of a very fine grain at the alloy/coating interface whose lattice spacings correspond to those expected for the cubic spinel structure. Thus the thin Cr-enriched oxide layer appears to correspond to the onset of $(Mn,Cr)_3O_4$ spinel formation.

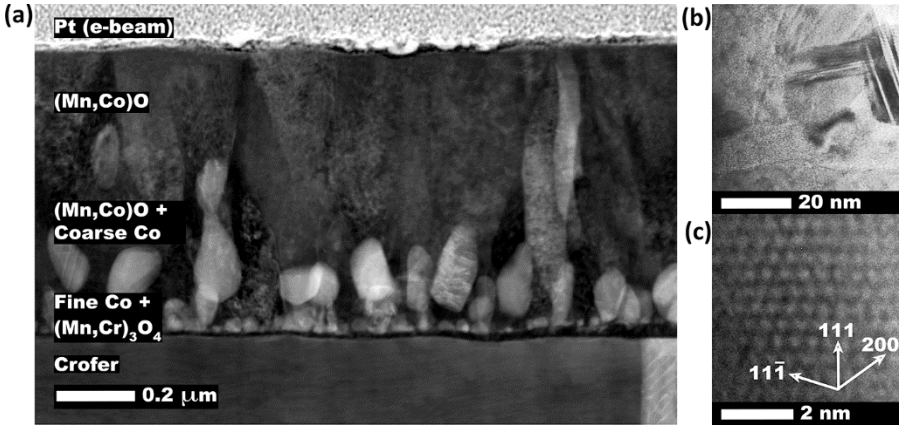

Figure 5.2: Microstructural detail from the cross-sectional sample shown in Figs 1 (c) and (d): (a) HAADF STEM image showing the main changes in microstructure through the deposit; (b) BF TEM image from a region at the alloy/coating interface; (c) HRTEM lattice image of a small (<5nm) spinel grain at the interface.

Other interesting features emerge from selected area diffraction pattern (SADP) analysis on these samples. Figure 5.3(a) is a bright field image showing a region of the deposit between the film center and the interface with the substrate, and Figure 5.3(b) is an SADP from the interface between the (Mn,Co)O grain at 1 and the Co grain at 2 in Figure 5.3(a). Firstly It is noted that the pattern from the Co (and indeed all other patterns from Co grains in this sample) correspond to those expected for the FCC allotrope of Co, rather than the equilibrium HCP structure. It is on this basis that the weak shoulder for the 110_{BCC} peak in the inset to Figure 5.1(a) was indexed as 111 for FCC Co, not 0002 for HCP Co. Secondly it is noted that the pattern in Figure 5.3(b) indicates that there is a strong orientation relationship (OR) between the (Mn,Co)O grain and the Co grain; the [011] directions are parallel in the two structures and there is a rotation of just 3° between the two structures about this axis. Similar effects were observed for other columnar (Mn,Co)O grains that lay above Co grains in the film.

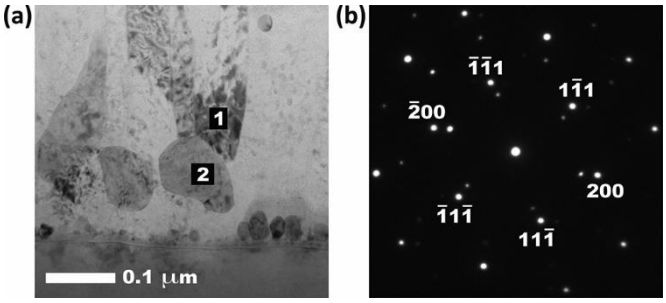

Figure 5.3: TEM data obtained from a region near the coating/substrate interface in the cross-sectional sample shown in Figs 1 (c) and (d): (a) BF TEM image; (b) SADP obtained from the interface between the (Mn,Co)O grain at 1 and the Co grain at 2 in (a).

5.3.2 Films after 0.5 h Annealing in Air at 800°C

The XRD data from the films after 0.5 h annealing (Figure 5.4(a)) revealed a very different phase mixture from that in the as-deposited films. There are peaks corresponding to the tetragonal Mn_2CoO_4 ($I4_1/amd$, a_0 = 0.5884 nm, c_0 = 0.8670 nm) and cubic $MnCo_2O_4$ ($Fd\bar{3}m$,

a_0 = 0.8433 nm) spinel phases, which co-exist for $Mn_{1.5}Co_{1.5}O_4$ at room temperature [200]. Thus, during the annealing, the phases in the film transform to those in the original MCO target. The SE images such as Figure 5.4(b) obtained from the deposit surface indicate that there is some moderate roughening during annealing. A montage of BF TEM images obtained from a FIB-cut cross-section through the deposit is shown in Figure 5.4(c). Such images reveal that the transformation to the spinel phases is accompanied by some dramatic changes in film structure. The film is still relatively smooth and uniform, but it is now much thicker (1020 ± 40 nm) and the columnar grains are coarser with a mean width of 158 ± 58 nm. However, the most remarkable difference in the film structure is the presence of large equi-axed pores with diameters of 134 ± 75 nm lying in the approximate location of the coarse Co grains in the as-deposited film. Compositional maps for Mn, Co, Fe and Cr obtained from an EDXS STEM spectrum imaging experiment on a region of this cross-section are shown in Figure 5.4(d). These maps show that: the Mn and Co are now distributed uniformly throughout the film; the bright features in Figure 5.4(c) are indeed pores; and there is now a significantly thicker (up to 90 nm) Cr-rich oxide layer at the interface. It is noted that while the images in Figures 5.4(b) and (c) are presented at the same scale as the corresponding data in Figure 5.1 for ease of comparison, the maps in Figure 4(d) are at roughly half the magnification of those in Figure 5.1(d). Here again, trends in composition were evaluated by integrating the measurements over the whole film, and over the top, middle and bottom thirds of the film thickness. These data are also given in Table 5.1.

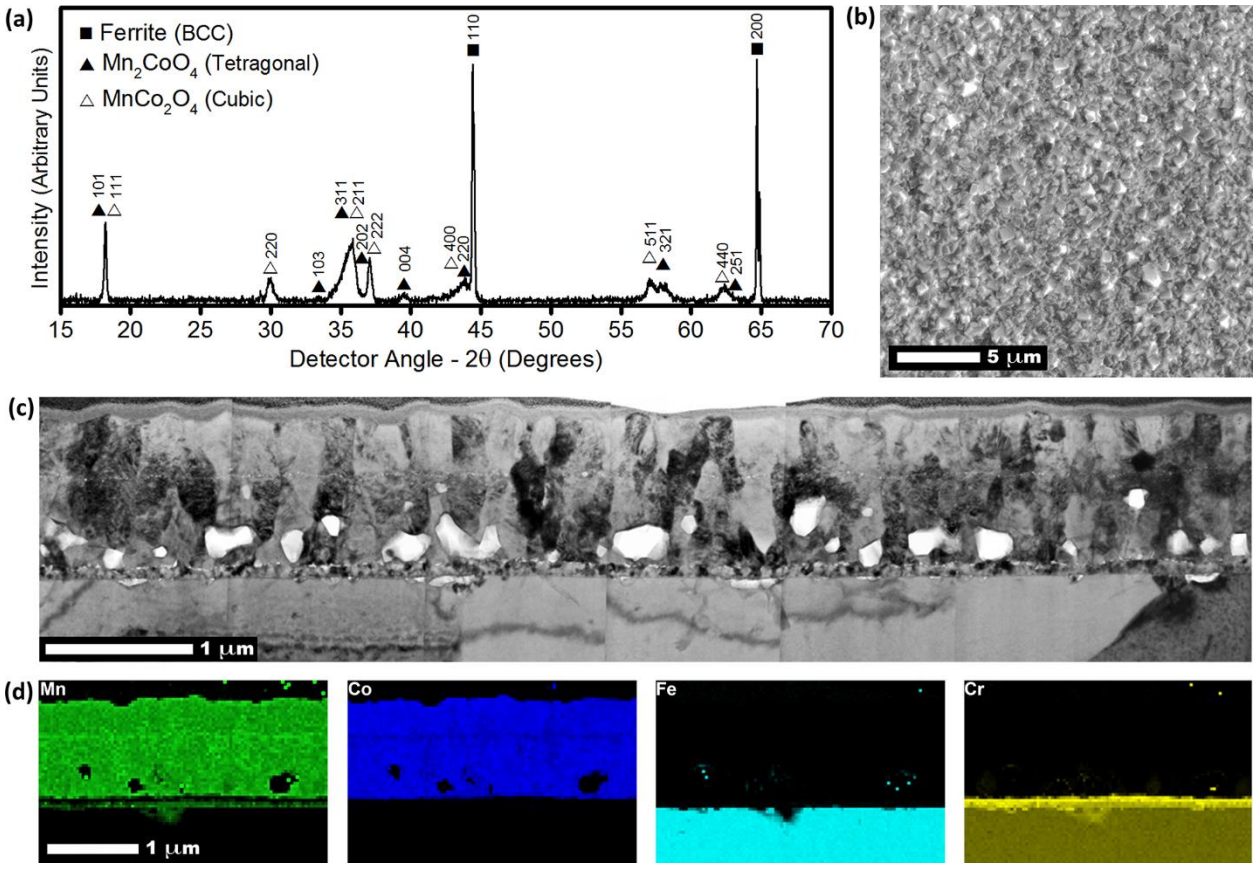

Figure 5.4: Overall microstructure of the film annealed at 800°C in air for 0.5 h: (a) XRD data; (b) SE SEM image obtained from the deposit surface; (c) montage of BF TEM images obtained from a FIB-cut cross-section through the deposit; (d) maps showing the distribution of Mn, Co, Fe and Cr in a region of the sample shown in (c).

Further details of the annealed microstructure were obtained by comparing HAADF STEM images such as Figure 5.5 with SADPs (not shown). Two additional features emerged from these data. Firstly, there is a band of very fine pores (<10 nm in diameter) lying parallel to the film surface at a depth of about 400 nm. Secondly, in this case the Cr-rich oxide layer at the film/substrate interface is essentially pure chromia (Cr_2O_3).

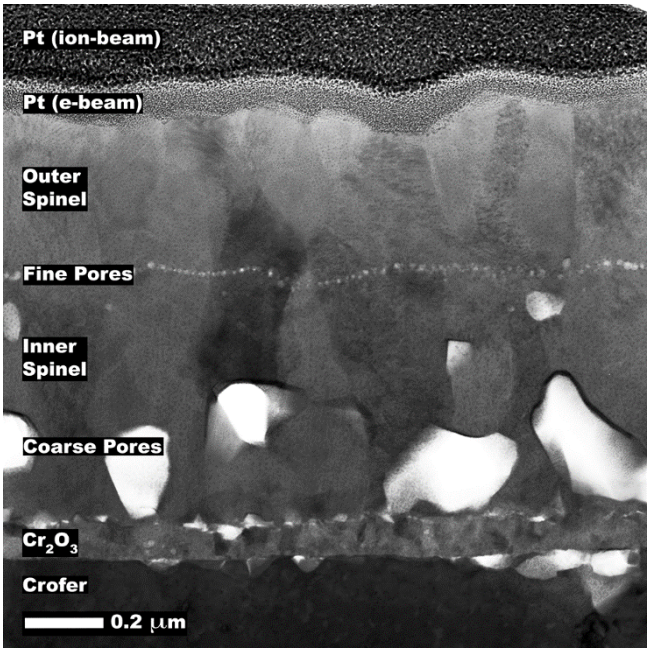

Figure 5.5: HAADF STEM image showing the main changes in microstructure through the cross-section shown in Figs 4 (c) and (d).

5.3.3 Films after 14 h Annealing in Air at 800°C

The XRD data obtained from the films annealed for 14 h (Figure 5.6(a)) reveal no further changes in the phases present, i.e. here again there is a mixture of cubic and tetragonal spinels. There are, however, marked changes in the surface topography of the films; SEM images such as Figure 5.6(b) show that faceted features up to 2 μm in diameter are present on the surface. The number and size of these features varies from location to location on the film surface, and the sizes and overall morphologies of the different regions suggest strongly that these are correlated with the underlying grains in the alloy substrate. Thus, the region shown in Figure 5.6(b) is smoother on the left and rougher with more large faceted features on the right, suggesting that this is a region of film across a grain boundary in the substrate. Figure 5.6(c) is a montage of BF TEM images obtained from a FIB-cut cross-section through the deposit along the

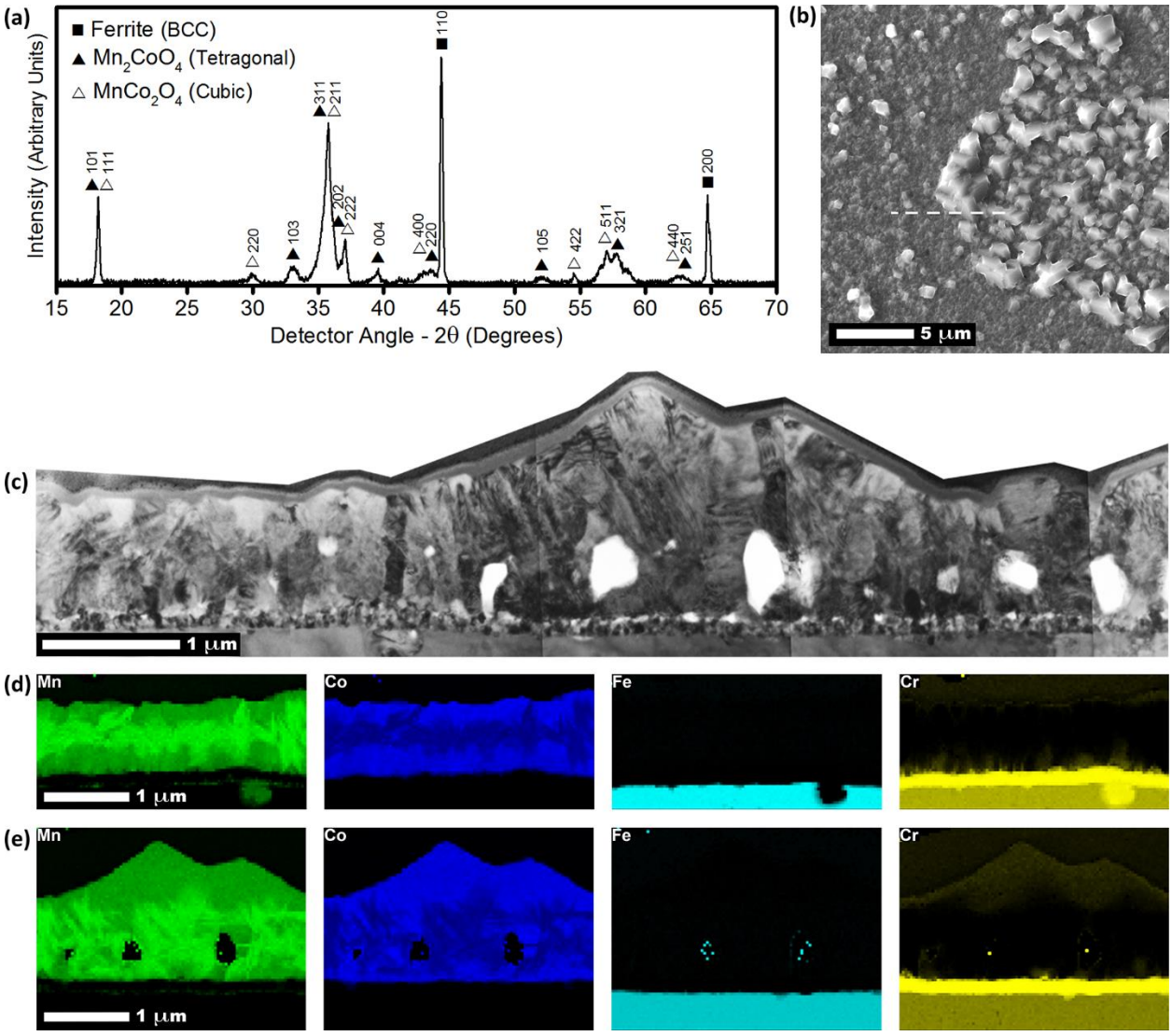

Figure 5.6: Overall microstructure of the film annealed at 800°C in air for 14 h: (a) XRD data; (b) SE SEM image obtained from the deposit surface; (c) montage of BF TEM images obtained from a FIB-cut cross-section through the deposit along the position marked by the dashed line in (b); (d) and (e) maps showing the distribution of Mn, Co, Fe and Cr in regions of the sample shown in (c): (d) is from the smooth region on the left of (c), whereas (e) is from the facetted region on the right of (c).

white dashed line in Figure 5.6(b). There are distinct differences in porosity across the field of view with a more dense film on the left below the smooth surface, and large pores on the right beneath the large faceted features. Figures 5.6(d) and (e) are compositional maps obtained from regions on the left and right of Figure 5.6(c), respectively. These maps show that the films exhibit a pronounced variation in composition. In the regions with smooth deposit surfaces (Figure 5.6(d)), the Mn and Co appear to have segregated, leaving the Mn-rich tetragonal spinel in the center of the film and the Co/Cr-rich cubic spinel phase at the film surface and at the interface with the substrate. The cation distribution in the rougher more faceted regions (Figure 5.6(e)) is rather different. While the center of the film is still Mn-rich and the surface is Co-rich, there is very little Mn depletion at the interface, and there is far more Cr in the faceted protrusions at the film surface than is found at the smoother surfaces, or indeed at the interface in these faceted regions. As before, the cation compositions were integrated over the top, middle and bottom thirds of the film thickness for both the smooth and the faceted regions, and these data are included in Table 5.1.

The microstructural details of the smooth region in Figure 5.6(c) are revealed in HAADF STEM images such as Figure 5.7. As for the 0.5 h sample, there is a band of fine pores between the inner and outer spinel, but the

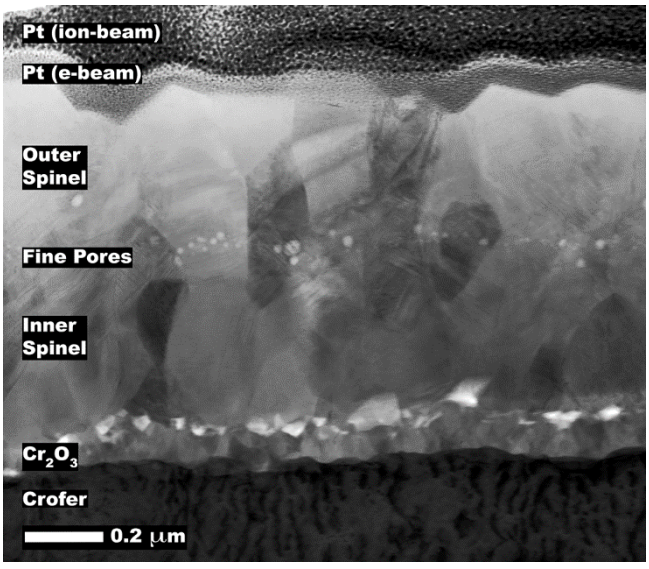

Figure 5.7: HAADF STEM image showing the main changes in microstructure through the cross-section shown in the smooth region in Figs 6 (c) and (d).

individual pores are larger (up to 60 nm in diameter) and the band is less well defined. Another interesting feature is that while the thicknesses of the outer spinel and the chromia layer at the interface are almost identical to those in the 0.5 h sample, the inner spinel is much thinner (445 nm as opposed to 610 after 0.5 h). The grains in both the inner and outer spinel layers are rather more equi-axed than in either the as-deposited or 0.5 h samples with a mean grain size of 180 ± 90 nm. There are some larger pores in the film, but these are less than 250 nm in diameter, irregularly shaped, and are confined to the interface between the inner spinel and the chromia layer.

The faceted regions exhibit rather different microstructures as shown in Figure 5.8. The overall average thickness of the film in these regions is >1000nm as compared to <850 nm in the smooth regions. The HAADF STEM images (Figure 5.8(a)) reveal the large pores clearly; these have diameters of up to 500 nm, and there is no evidence of the fine pores in these regions. The grain size in the

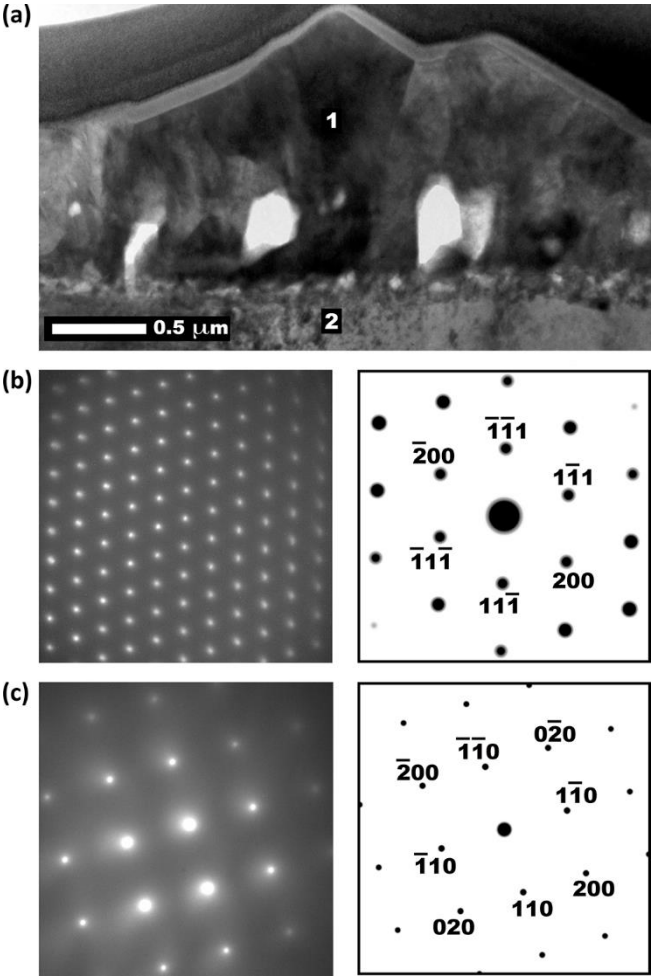

Figure 5.8: TEM data from grains in the facetted region in Figs 6 (c) and (e): (a) BF TEM image; (b) SADP obtained from the spinel grain at 1 in (a) and corresponding indexed schematic; (c) SADP obtained from the Crofer grain at 2 in (a) with corresponding indexed schematic. The SADPs in (b) and (c) are shown at the same camera length, but the schematic in (b) is enlarged for clarity.

spinel near the interface is similar to that in the smooth regions, but the faceted features comprise just a few grains of 1500 nm or more in diameter. It is interesting to note that these large grains appear to exhibit a well-defined OR with respect to the underlying ferrite grains in the Crofer substrate. One example is shown in Figures 5.8(b) and (c): these correspond to SADPs with indexed schematics from the spinel and ferrite grains at 1 and 2 in Figure 5.8(a), respectively. In each case the spinel grains lie within a few degrees of:

$$[100]_{Spinel} \text{ // } [100]_{Ferrite}$$

$$[011]_{Spinel} \text{ // } [010]_{Ferrite}$$

Also noted is that the large faceted spinel grains tend to lie with {111} parallel to the overall surface, but this is not a low index plane in the ferrite for the OR given above.

5.4 Discussion

5.4.1 As-Deposited Films

There were three distinct microstructural layers within the as-deposited film: a thin (≈ 50 nm) layer at the alloy/coating interface comprising a mixture of fine Co and (Mn,Co)O grains, a thicker (≈ 250 nm) layer of coarser Co and (Mn,Co)O grains, and a single phase (Mn,Co)O top layer that makes up over half of the deposit thickness. The formation of these layers can be accounted by considering the changes in temperature and oxygen partial pressure over the course of the deposition.

The transition from fine-grained equi-axed to coarse-grained columnar deposits is typical for polycrystalline thin films grown by PLD. At the onset of the deposition process, the cartridge heater current determines the substrate temperature. For deposition onto metallic

substrates, the temperature is typically kept at a moderate value (400°C in this case) that promotes the formation of crystalline deposits while inhibiting reactions between the substrate and the deposit. Thus, the material that arrives at the substrate in the first few pulses has limited surface mobility and tends to form a fine-grained microstructure. As the deposition proceeds, the surface temperature rises due to repeated exposure to the highly energetic plume and limited thermal conductivity through the oxide film. This leads to the formation of coarser microstructures by some combination of an increase in the scale of any phase separation and the overgrowth of less favorably oriented grains by those which grow more rapidly. At some point in the deposition, a steady state temperature is attained and a columnar microstructure develops.

To explain the difference between the phases present in the target and those in the deposit, it is important to recall that the deposition is performed at a very low partial pressure of oxygen. In the layers closest to the interface, the phase mixture of FCC metallic Co and Mn-rich oxide with the rock-salt structure resembles that which forms during the reduction stage of the reactive consolidation process for MCO slurry coatings [198, 241]. In the latter process, the MCO is reduced to pure MnO and pure Co because the temperatures are higher and the oxygen partial pressures are lower than in the PLD considered here. Nonetheless, in the earliest stages of our PLD experiments there is a reduction in the oxidation state of Mn and Co from a mixture of +2 and +3 in the MCO target to +2 for Mn and a mixture of +2 and 0 for Co in the (Mn,Co)O + Co deposit. As the deposition proceeds, both the temperature and the effective partial pressure of oxygen will increase at the deposit surface. At some point this leads to a transition from (Mn,Co)O + Co to single-phase (Mn,Co)O where both Mn and Co must adopt the +2 oxidation

state. Such transitions have been reported previously, albeit under rather different conditions. For example, Bergman and Ågren calculated the isothermal section of the Mn-Co-O system at 1500 K and showed that there is a transition from pure FCC Co and (Mn,Co)O to single phase (Mn,Co)O at an oxygen partial pressure of $7.6 \cdot 10^{-4}$ mTorr [244].

To simplify the discussion of the reactions and transformations that occur upon subsequent heat treatment, there is an extracted mean value for the composition of the (Mn,Co)O phase in two different ways. Firstly, the used measured value of a_0 to obtain an effective composition by assuming that the lattice parameter obeys Vegard's law in this phase; it is noted that this assumption is reasonable since it has been shown previously for $Mn_{1-x}Co_xO$ that a_0 varies linearly with x [245]. Secondly, the composition of the phase has been calculated by assuming that the overall cation composition of the film is exactly equi-atomic as indicated by the EDXS data, and then subtracting the Co atoms in the metallic grains using the measured volume fraction of these grains. Both approaches gave the same result: $Mn_{0.7}Co_{0.3}O$.

Lastly, it is noted that there is a very thin $(Mn,Cr)_3O_4$ RL at the interface due to outward diffusion of Cr into the deposit. Such Cr-rich spinel RLs have been shown to form even under conditions where MCO is reduced [241], but the extent of this RL is presumably restricted by the limited mobility of Cr at the substrate temperature of 400°C. The absence of chromia is further evidence of this limited mobility: Koc and Timucin have shown that the limit of Cr solubility in $(Mn,Cr)_3O_4$ spinel is $MnCr_2O_4$ and that further Cr substitution results in the formation of chromia [77]. The disparity in the thickness of the $(Mn,Cr)_3O_4$ layer from one ferrite grain to another indicates a local variation in the Cr flux, but in no case is this high enough to form a chromia scale under the deposition conditions used here.

5.4.2 Films after 0.5 h Annealing in Air at 800°C

Annealing for 0.5 h in air at 800°C resulted in a conversion of the phases in the film from (Mn,Co)O + Co to Mn_2CoO_4 + $MnCo_2O_4$ (i.e. the phases present in the original target). There is clear evidence that this re-oxidation of the film proceeds by outward diffusion of the cations to form fresh oxide at the surface, rather than by inward diffusion of oxygen. Firstly, there are large pores whose size and location correspond approximately to those of the Co phase in the as-deposited film; this clearly shows that that the Co must diffuse outwards during the re-oxidation process. Secondly, there is a band of very fine pores at around 610 nm from the alloy/coating interface. This is similar to the initial thickness of the deposit and suggests strongly that the pores mark the position of the film surface at the onset of the re-oxidation process. Such pores have been observed previously in, for example, studies of the oxidation of CoO to Co_3O_4 [246], wherein they were ascribed to surface impurities or imperfections acting as vacancy sinks during growth of the Co_3O_4 layer.

Following Przybylski and Smeltzer [246] one can consider the conversion of the rock-salt (Mn,Co)O phase to spinel by the two coupled reactions:

(1) $24\ Mn_{0.5}Co_{0.5}O \rightarrow 6\ Mn_{1.5}Co_{1.5}O_4 + 3\ Mn^{n+} + 3\ Co^{n+} + 3\ ne^-$

(2) $3\ Mn^{n+} + 3\ Co^{n+} + 3\ ne^- + 4O_2 \rightarrow 2\ Mn_{1.5}Co_{1.5}O_4$

Reaction (1) is a displacement reaction by which the spinel layer grows to consume the rock-salt phase, whereas Reaction (2) is the process by which fresh spinel oxide grows at the surface. For simplicity, the composition $Mn_{0.5}Co_{0.5}O$ for the rock-salt phase is used, which is equal to that measured experimentally near the surface of the initial deposit. The effects of phase separation in the spinel is neglected since MCO is a single-phase cubic spinel at the oxidation

temperature for this cation ratio [198]. In this stage of the re-oxidation process, the two reactions indicate that 24 moles of the rock-salt phase would react to form 6 moles of spinel at the rock-salt / spinel interface with the excess cations diffusing to the surface and forming two moles of additional spinel by the reduction of four moles of oxygen. Thus, it is expected that the band of very fine pores marking the initial surface to lie at a depth equal to 25% of the spinel layer thickness.

As the re-oxidation proceeds, the situation becomes more complex. The Mn content of the rock-salt phase increases with distance from the original film surface, and so there will initially be an excess of Mn ions produced by the displacement reaction. Once the reaction front reaches the point where the rock-salt phase becomes more Mn-rich than $Mn_{0.625}Co_{0.375}O$, a net inward flux of Co is required to produce $Mn_{1.5}Co_{1.5}O_4$ spinel via the displacement reaction. As discussed in the previous section, the mean composition of the rock-salt phase in the films is $Mn_{0.7}Co_{0.3}O$ and so during much of the process the displacement reaction will produce Mn ions only. Since the spinel at the surface in the films after 0.5 h annealing is actually slightly Co-rich, the flux of these excess Mn ions must be compensated for by a flux of Co ions from the Co grains. In the seminal work by Gulbransen and Andrew [247], it was shown that oxidation of Co in such situations proceeds by ionization of Co at the metal/oxide interface and that the oxidation rate is dictated by the mobility of Co. Since the compositional inhomogeneities in the as-deposited film are almost completely eliminated during re-oxidation, one can infer that the mobility of the Co ions is much higher than that of the Mn ions in both the rock-salt oxide and spinel phases. Clearly, these additional fluxes of Mn and Co will enhance the rate at which fresh

spinel oxide is formed at the surface relative to spinel formation by the displacement reaction, resulting in a thicker outer spinel layer as observed experimentally.

It is noted that while it is expected that the re-oxidized $Mn_{1.5}Co_{1.5}O_4$ film to exhibit a single-phase cubic spinel structure at the annealing temperature, the XRD data indicate that phase separation occurs upon cooling to ambient conditions giving the same mixture of cubic ($MnCo_2O_4$-type) and tetragonal (Mn_2CoO_4-type) spinels found in ceramic samples with this composition. Since the individual phase domains cannot be resolved clearly in the compositional maps, this phase separation must occurs on a very fine scale.

5.4.3 Films after 14 h Annealing in Air at 800°C

Annealing for 14 h in air at 800°C resulted in a remarkably different microstructure to that observed after 0.5 h annealing. While the XRD data indicate that the same mixture of cubic and tetragonal spinel phases are present, the TEM data show a very different phase distribution. In the sample annealed for 14 h, not only do the compositional maps reveal the phase separation clearly, but also they indicate that there is phase segregation. There is more Mn-rich tetragonal spinel present in the center of the film and more Co-rich cubic spinel at the coating surface and at the alloy/coating interface. Given that the samples annealed for 0.5 and 14 h were cooled to room temperature under the same conditions, both the phase separation and the phase segregation presumably occur in the latter sample during the annealing rather than during cooling.

It is noted that the upper and lower layers in this sample contain Cr while the center layer does not (Table 5.1). It is shown previously that the presence of Cr stabilizes the cubic

spinel structure in MCO [71, 201] and that Cr occupies the in the octahedral B sites structure preferentially [242, 248]. Thus the diffusion of Cr from the chromia layer into the spinel coating during annealing could lead to the rejection of Mn, and this could act as the driving force for the formation of a cubic Co-rich layer at the interface with a tetragonal Mn-rich layer above. The solubility of Cr is limited in the tetragonal structure due to the symmetry of the octahedral site [152]. On this basis, the presence of Cr in the layer at the coating surface is also consistent with this being a cubic Co-rich layer, but it is not clear why the formation of this layered structure is favored rather than a mixture of cubic and tetragonal phase domains. Possible reasons for this effect include volumetric differences between the Cr-substituted, Co-rich cubic spinel and the Mn-rich tetragonal spinel, and/or differences in the diffusivities of the Co, Cr and Mn cations through the spinel phases (e.g. [108]). Further work is required to elucidate this effect.

The sample annealed for 14 h also exhibited pronounced differences in the microstructure of the coating from one substrate grain to another. For some substrate grains the coating is relatively smooth and exhibits a somewhat more dense structure than that observed for the 0.5 h sample. For other substrate grains, large facetted protrusions appear on the coating surface and there are coarse pores near the substrate/coating interface. In the latter case, the protrusions are cubic spinel grains, which exhibit a simple OR with respect to the underlying substrate grain, and the Cr content in these regions is higher than that at the surface in the smooth regions of the coating. Clearly, these differences must be related to the orientation of the substrate grains. For substrate grains that lead to favorably oriented columnar spinel grains, growth of the upper layer may be enhanced and coarsening of the

pores in the underlying coating could lead to enhanced vapor phase transport of chromium species across the pores. For other substrate grains, the spinel columns may be oriented less favorably and the formation of the Cr-substituted Co-rich layer at the interface could lead to closure of the pores inhibiting subsequent transport of Cr towards the coating surface.

5.5 Conclusions

Coatings have been deposited onto electro-polished Crofer 22 APU substrates by PLD from an $Mn_{1.5}Co_{1.5}O_4$ target. A combination of XRD, SEM and TEM techniques has been used to characterize the coatings in the as-deposited condition and after annealing in air at 800°C. The main findings are as follows:

1. The as-deposited coatings contain columnar rock-salt (Mn,Co)O grains with embedded grains of FCC Co near the coating/substrate interface. This phase mixture arises from reduction of the target material in the PLD plume due to the low partial pressure of oxygen in the chamber during deposition.
2. After 0.5 h annealing in air the coatings re-oxidize to form spinel phases with the same overall composition as the target. This results in a significant expansion in the volume of oxide present. This re-oxidation proceeds by a displacement reaction in the rock-salt oxide accompanied by outward diffusion of the cations to form fresh oxide at the free surface. The even distribution of the Co throughout the coating indicates that the Co ions are significantly more mobile than the Mn ions in the oxide phases at the annealing temperature. The spinel reaction product is cubic at

the annealing temperature but undergoes phase separation upon cooling to form a very fine mixture of tetragonal and cubic spinels.

3. After 14 h annealing the re-oxidized coatings exhibit significant phase segregation with cubic Co-rich layers at the alloy/coating interface and at the coating surface, and a tetragonal Mn-rich layer in the center of the coating. The presence of Cr in the former layers but not in the latter indicates that Cr stabilizes the cubic phase. The coating morphology varies locally with smooth dense regions and facetted regions with large sub-surface pores. The latter regions correspond to areas with a well-defined OR between the spinel at the surface and the underlying substrate grain indicating that substrate orientation may have a significant effect on Cr transport through the coating.

Thus, while high quality MCO coatings can be produced on Crofer 22 APU by a combination of PLD and post-deposition annealing, the substrate grain structure and texture may need to be controlled to promote the long-term high-temperature microstructural stability of such coatings.

5.6 Future Work

In future studies of the oxidation behavior of PLD MCO-based films, the process parameters should be modified to include a higher oxygen partial pressure so that there is direct deposition of a dense spinel film. A comparative study between an MCO film deposited directly and the vacuum deposited MCO film would help to clarify the mechanism for the formation of the facetted regions and the phase segregation.

The work performed on PLD MCO films on alloy interconnects until now has focused on the early stages of chromia scale growth and RL development. Long term heat treatments are necessary to assess the performance of MCO over periods of time in which SOFCs operate. With heat treatments of 1000 h, the equilibrium RL composition would be attained and the effects from degradation would be observed. Long term heat treatments would also allow a clear comparison of the performance of MCO-based spinel substituted with Fe and Ni. The performance could be based on a parabolic oxidation behavior and provide values for the diffusivity of the chromium and oxygen through the spinel lattice. This comparative study is necessary because there is no clear evidence on the effect that Fe and Ni substitution have on the performance of MCO interconnect coatings [188, 193].

6 References

[1] A.E. Lutz, R.S. Larson, and J.O. Keller, “Thermodynamic comparison of fuel cells to the carnot cycle,” *Int. J. Hydrogen Energy*, **27** [10] 1103–1111 (2002).

[2] R. Kurz, “Gas turbine performance;” pp. 131–146 in *Proc. thirty-fourth Turbomach. Symp.* 2005.

[3] C. Soares, *Gas Turbines: A Handbook of Air, Land, and Sea Applications*, Second. Butterworth-Heinemann, Oxford, 2014.

[4] W. Grove, “On voltaic series and the combination of gases by platinum,” *London Edinburgh Philos. Mag. J. Sci.*, **14** [86] 127–130 (1839).

[5] H. Hassanzadeh and S.H. Mansouri, “Efficiency of ideal fuel cell and carnot cycle from a fundamental perspective;” pp. 245–254 in *Proc. Inst. Mech. Eng. Part A J. Power Energy*. 2005.

[6] W. Dunbar, N. Lior, and R.A. Gaggioli, “Combining fuel cells with fuel-fired power plants for improved exergy efficiency,” *Energy*, **16** [10] 1259–1274 (1991).

[7] P. Singh and N.Q. Minh, “Solid oxide fuel cells: technology status,” *Int. J. Appl. Ceram. Technol.*, **1** [1] 5–15 (2004).

[8] S. Curtin and J. Gangi, “2013 fuel cell technologies market report,” *Energy Efficiency & Renewable Energy* (2014).

[9] 4th Energy Wave, “The fuel cell and hydrogen annual review, 2015,” (2015).

[10] A.B. Stambouli and E. Traversa, “Solid oxide fuel cells (SOFCs): a review of an environmentally clean and efficient source of energy,” *Renew. Sustain. Energy Rev.*, **6** [5] 433–455 (2002).

[11] L. Mond and C. Langer, “A new form of gas battery,” *Proc. R. Soc. London*, **46** [280-285] 296–304 (1889).

[12] *http://science.nasa.gov*, *Cool Fuel Cells*, (2015).

[13] S. Sieniutycz, “Thermodynamic basis of fuel cell systems,” *Cybern. Phys.*, **1** [1] 67–72 (2012).

[14] Müller, A. Weber, H.J. Beie, A. Krügel, D. Gerthsen, and E. Ivers-Tiffee, “Influence of current density and fuel utilization on the degradation of the anode;” pp. 353–362 in *Proc. 3rd Eur. Solid Oxide Fuel Cell Forum*. 1998.

[15] A.V. Virkar, J. Chen, C.W. Tanner, and J. Kim, “The role of electrode microstructure on activation and concentration polarisations in solid oxide fuel cells,” *Solid State Ionics*, **131** 189 (2000).

[16] F. Zhao and A.V. Virkar, “Dependence of polarization in anode-supported solid oxide fuel cells on various cell parameters,” *J. Power Sources*, **141** [1] 79–95 (2005).

[17] A. Musa, A. Agina, and M. Talbi, “Operating conditions on the performances of SOFC fueled with methane;” in *Int. Conf. Renew. Energies Power Qual.* 2012.

[18] T. Kuramochi, H. Wu, A. Ramírez, A. Faaij, and W. Turkenburg, “Techno-economic prospects for CO_2 capture from a solid oxide fuel cell-combined heat and power plant. preliminary results,” *Energy Procedia*, **1** [1] 3843–3850 (2009).

[19] W.Y. Wang, Y. Peng, P. Zhang, L. Yang, and Z. Mao, “Research progress in perovskite type cathode material for intermediate-to-low temperature SOFC,” *Batter. Bimon.*, **35** [5] 393–394 (2005).

[20] S. Elangovan, J. Hartvigsen, D. Larsen, I. Bay, and F. Zhao, “Materials for solid oxide fuel cells,” *ECS Trans.*, **35** [1] 2875–2882 (2011).

[21] W.Z. Zhu and S.C. Deevi, “A review on the status of anode materials for solid oxide fuel cells,” *Mater. Sci. Eng. A*, **362** [1-2] 228–239 (2003).

[22] D. Ding, X. Li, S.Y. Lai, K. Gerdes, and M. Liu, “Enhancing SOFC cathode performance by surface modification through infiltration,” *Energy Environ. Sci.*, **7** [2] 552 (2014).

[23] S. De Souza, S.J. Visco, and L.C. De Jonghe, “Thin-film solid oxide fuel cell with high performance at low- temperature,” *Solid State Ionics*, **98** 57–61 (1997).

[24] L. Antoni, “Materials for solid oxide fuel cells : the challenge of their stability,” *Mater. Sci. Forum*, **461** 1073–1090 (2004).

[25] X. Montero, F. Tietz, D. Stöver, M. Cassir, and I. Villarreal, “Evaluation of commercial alloys as cathode current collector for metal-supported tubular solid oxide fuel cells,” *Corros. Sci.*, **51** [1] 110–118 (2009).

[26] R. Singer, “Flat plate solid oxide fuel cells,” *Mod. Power Syst.*, **10** [10] 19–19 (1990).

[27] O. Yamamoto, “Solid oxide fuel cells: fundamental aspects and prospects,” *Electrochim. Acta*, **45** [15-16] 2423–2435 (2000).

[28] N.Q. Minh, “Ceramic fuel cells,” *J. Am. Ceram. Soc.*, **76** [3] 563–588 (1993).

[29] N.Q. Minh and T. Takahashi, Science and Technology of Ceramic Fuel Cells, Elsevier, 1995.

[30] J.W. Fergus, “Metallic interconnects for solid oxide fuel cells,” *Mater. Sci. Eng. A*, **397** [1-2] 271–283 (2005).

[31] J. Wu and X. Liu, “Recent development of SOFC metallic interconnect,” *J. Mater. Sci. Technol.*, **26** [4] 293–305 (2010).

[32] Z. Yang, G. Xia, M. Walker, C. Wang, J. Stevenson, and P. Singh, “High temperature oxidation/corrosion behavior of metals and alloys under a hydrogen gradient,” *Int. J. Hydrogen Energy*, **32** [16] 3770–3777 (2007).

[33] B. Stacey, S.P.S. Badwal, and K. Foger, “Review of manufacturing processes for fabrication of SOFC components,” *J. Aust. Ceram. Soc.*, **34** [1] 1998 (1998).

[34] M. Brandner, “Herstellung einer metall/keramik verbundstruktur fuer hochtemperaturbrennstoffzellen in mobilen anwendungen,” Ph.D. Thesis, Research Center Juelich, Juelich, Germany (2006).

[35] S.T. Ertl, “Untersuchungen zur oxidationsbedingten lebensdauer von chromstählen für die anwendung in der hochtemperaturbrennstoffzelle (SOFC),” Ph.D. Thesis, RWTH Aachen, Germany (2006).

[36] M. Alinger and S. Taylor, “SECA SOFC program at GE global research;” pp. 1–34 in *8th Annu. SECA Work. Peer Rev. Meet.* 2007.

[37] L. Chen, N. Magdefrau, E. Sun, J. Yamanis, D. Frame, and C. Burila, “Strontium transport and conductivity of $Mn_{1.5}Co_{1.5}O_4$ coated haynes 230 and Crofer 22 APU under simulated solid oxide fuel cell condition,” *Solid State Ionics*, **204-205** 111–119 (2011).

[38] S. Megel, E. Girdauskaite, V. Sauchuk, M. Kusnezoff, and A. Michaelis, “Area specific resistance of oxide scales grown on ferritic alloys for solid oxide fuel cell interconnects,” *J. Power Sources*, **196** [17] 7136–7143 (2011).

[39] M. Stanislowski, E. Wessel, K. Hilpert, T. Markus, and L. Singheiser, “Chromium vaporization from high-temperature alloys,” *J. Electrochem. Soc.*, **154** [4] A295–A306 (2007).

[40] J. Froitzheim, H. Ravash, E. Larsson, L.G. Johansson, and J.E. Svensson, “Investigation of chromium volatilization from FeCr interconnects by a denuder technique,” *J. Electrochem. Soc.*, **157** [9] B1295–B1300 (2010).

[41] S.P. Jiang, J.P. Zhang, L. Apateanu, and K. Foger, “Deposition of chromium species at sr-doped $LaMnO_3$ electrodes in solid oxide fuel cells. I. mechanism and kinetics,” *J. Electrochem. Soc.*, **147** [11] 4013 (2000).

[42] E. Konysheva, H. Penkalla, E. Wessel, J. Mertens, U. Seeling, L. Singheiser, and K. Hilpert, “Chromium poisoning of perovskite cathodes by the ODS alloy $Cr_5Fe_1Y_{23}$ and the high chromium ferritic steel Crofer22APU,” *J. Electrochem. Soc.*, **153** [4] A765 (2006).

[41] W.N. Liu, X. Sun, E. Stephens, and M. a. Khaleel, “Life prediction of coated and uncoated metallic interconnect for solid oxide fuel cell applications,” *J. Power Sources*, **189** [2] 1044–1050 (2009).

[42] N. Shaigan, W. Qu, D.G. Ivey, and W. Chen, “A review of recent progress in coatings, surface modifications and alloy developments for solid oxide fuel cell ferritic stainless steel interconnects,” *J. Power Sources*, **195** [6] 1529–1542 (2010).

[43] H. Kozuka, K. Yamagiwa, K. Ohbayashi, and K. Koumoto, “Origin of high electrical conductivity in alkaline-earth doped $LaCoO_3$,” *J. Mater. Chem.*, **22** [22] 11003 (2012).

[44] N. Shaigan, D.G. Ivey, and W. Chen, “Co/$LaCrO_3$ composite coatings for AISI 430 stainless steel solid oxide fuel cell interconnects,” *J. Power Sources*, **185** [1] 331–337 (2008).

[45] Z. Yang, G.-G. Xia, G.D. Maupin, and J.W. Stevenson, “Evaluation of perovskite overlay coatings on ferritic stainless steel for SOFC interconnect application,” *J. Electrochem. Soc.*, (2006).

[46] H. Kozuka, K. Ohbayashi, and K. Koumoto, “Electronic conduction in La-based perovskite-type oxides,” *Sci. Technol. Adv. Mater.*, **16** [2] 026001 (2015).

[47] C. Gindorf, L. Singheiser, K. Hilpert, M. Schroeder, M. Martin, H. Greiner, and F. Richter, “Chromium vaporization from metallic interconnect and retention by perovskite layers,” *Solid oxide fuel cells (SOFC VI) Proc. Sixth Int. Symp.*, 774–782 (1999).

[48] C. Gindorf, K. Hilpert, H. Nabielek, and L. Singheiser, “Chromium release from metallic interconnects with and without coatings;” pp. 845–854 in *Fourth Eur. Solid Oxide Fuel Cell Form*. 2000.

[49] C. Gindorf, L. Singheiser, and K. Hilpert, “Chromium vaporisation from Fe,Cr base alloys used as interconnect in fuel cells,” *Mater. Technol.*, **72** [11] 528–533 (2001).

[50] F. Mattu, F. Ebrahimi, E. Traversa, and E.D. Wachsman, “Ceramic PLD coatings on ferritic stainless steel for interconnect in IT-SOFCs;” pp. 2005–2007 in *Solid Oxide Fuel Cells (SOFC IX)*. Edited by S.C. Singhal and J. Mizusake. Eletrochemical Society, 2005.

[51] L. Mikkelsen, N. Pryds, and P.V. Hendriksen, “Preparation of $La_{0.8}Sr_{0.2}Cr_{0.97}V_{0.03}O_{3-\delta}$ films for solid oxide fuel cell application,” *Thin Solid Films*, **515** [16] 6537–6540 (2007).

[52] L. Mikkelsen, M. Chen, P.V. Hendriksen, A. Persson, N. Pryds, and K. Rodrigo, “Deposition of $La_{0.8}Sr_{0.2}Cr_{0.97}V_{0.03}O_3$ and $MnCr_2O_4$ thin films on ferritic alloy for solid oxide fuel cell application,” *Surf. Coatings Technol.*, **202** [4-7] 1262–1266 (2007).

[53] Y. Larring and T. Norby, “Spinel and perovskite functional layers between plansee metallic interconnect (Cr-5 wt % Fe-1 wt % Y_2O_3 and ceramic $(La_{0.85}Sr_{0.15})_{0.91}MnO_3$ cathode materials for solid oxide fuel cells,” *J. Electrochem. Soc.*, **147** [9] 3251 (2000).

[54] D.-J. Jan, C.-T. Lin, and C.-F. Ai, “Structural characterization of $La_{0.67}Sr_{0.33}MnO_3$ protective coatings for solid oxide fuel cell interconnect deposited by pulsed magnetron sputtering,” *Thin Solid Films*, **516** [18] 6300–6304 (2008).

[55] M. Mori, Y. Hiei, and N.M. Sammes, “Sintering behavior and mechanism of Sr-doped lanthanum chromites with a site excess composition in air,” *Solid State Ionics*, **123** [1] 103–111 (1999).

[56] C. Chu, J. Lee, T. Lee, and Y. Cheng, “Oxidation behavior of metallic interconnect coated with La–Sr–Mn film by screen painting and plasma sputtering,” *Int. J. Hydrogen Energy*, **34** [1] 422–434 (2009).

[57] T. Brylewski, M. Nanko, T. Maruyama, and K. Przybylski, “Application of Fe – 16Cr ferritic alloy to interconnector for a solid oxide fuel cell,” *Solid State Ionics*, **143** 131 – 150 (2001).

[58] Brylewski T, Nanko M, Maruyama T, and Przybylski K. “Microstructure of Fe–25Cr/ (La, Ca)CrO_3 composite interconnector in solid oxide fuel cell operating conditions.” Mater. Chem. Phys. **81** 434–437 (2003).

[59] Z. Yang, G.-G. Xia, G.D. Maupin, and J.W. Stevenson, “Conductive protection layers on oxidation resistant alloys for SOFC interconnect applications,” *Surf. Coatings Technol.*, **201** [7] 4476–4483 (2006).

[60] M.V.F. Schlupp, J.W. Kim, A. Brevet, C. Rado, K. Couturier, U.F. Vogt, F. Lefebvre-Joud, and A. Züttel, “Avoiding chromium transport from stainless steel interconnects into contact layers and oxygen electrodes in intermediate temperature solid oxide electrolysis stacks,” *J. Power Sources*, **270** 587–593 (2014).

[61] X. Montero, N. Jordán, J. Pirón-Abellán, F. Tietz, D. Stöver, M. Cassir, and I. Villarreal, "Spinel and perovskite protection layers between Crofer22APU and $La_{0.8}Sr_{0.2}FeO_3$ cathode materials for SOFC interconnects," *J. Electrochem. Soc.*, **156** [1] B188–B196 (2009).

[62] X. Montero, F. Tietz, D. Sebold, H.P. Buchkremer, a. Ringuede, M. Cassir, a. Laresgoiti, and I. Villarreal, "$MnCo_{1.9}Fe_{0.1}O_4$ spinel protection layer on commercial ferritic steels for interconnect applications in solid oxide fuel cells," *J. Power Sources*, **184** [1] 172–179 (2008).

[63] T. Akashi, T. Inuoue, and T. Maruyama, "Electrical conductivity measurement for estimation of standard gibbs energy change of ternary oxide formation," *Mater. Trans. JIM(Japan)*, **41** [12] 1646–1650 (2000).

[64] M. Mori, Y. Hiei, N.M. Sammes, and G. a. Tompsett, "Thermal-expansion behaviors and mechanisms for Ca- or Sr-doped lanthanum manganite perovskites under oxidizing atmospheres," *J. Electrochem. Soc.*, **147** [4] 1295 (2000).

[65] L. Xu, L. Wencong, P. Chunrong, S. Qiang, and G. Jin, "Two semi-empirical approaches for the prediction of oxide ionic conductivities in ABO_3 perovskites," *Comput. Mater. Sci.*, **46** [4] 860–868 (2009).

[66] E. Bucher, W. Sitte, I. Rom, I. Papst, W. Grogger, and F. Hofer, "Microstructure and ionic conductivity of strontium-substituted lanthanum cobaltites," *Solid State Ionics*, **152-153** 417–421 (2002).

[67] N. Pryds, B. Toftmann, J. Schou, P.V. Hendriksen, and S. Linderoth, "Electrical and structural properties of $L_{0.8}Sr_{0.2}Mn_{0.5}Co_{0.5}O_3 \pm \delta$ films produced by pulsed laser deposition," *Appl. Surf. Sci.*, **247** 466–470 (2005).

[68] E. Konysheva, J. Laatsch, E. Wessel, F. Tietz, N. Christiansen, L. Singheiser, and K. Hilpert, "Influence of different perovskite interlayers on the electrical conductivity between $La_{0.65}Sr_{0.3}MnO_3$ and Fe/Cr-based steels," *Solid State Ionics*, **177** [9-10] 923–930 (2006).

[69] A.A. Taskin, A.N. Lavrov, and Y. Ando, "Achieving fast oxygen diffusion in perovskites by cation ordering," *Appl. Phys. Lett.*, **86** 091910 (2005).

[70] L. Chen, E.Y. Sun, J. Yamanis, and N. Magdefrau, "Oxidation kinetics of $Mn_{1.5}Co_{1.5}O_4$-coated haynes 230 and Crofer 22 APU for solid oxide fuel cell interconnects," *J. Electrochem. Soc.*, **157** [6] B931–B942 (2010).

[71] N.J. Magdefrau, L. Chen, E.Y. Sun, J. Yamanis, and M. Aindow, "Formation of spinel reaction layers in manganese cobaltite- coated Crofer22 APU for solid oxide fuel cell interconnects," *J. Power Sources*, **227** 318–326 (2013).

[72] E. Aukrust and A. Muan, “Thermodynamic properties of solid solutions with spinel-type structure. I, the system Co_3O_4-Mn_3O_4,” *Trans. Metall. Soc. AIME*, **230** 378–382 (1964).

[73] H. Bordeneuve, C. Tenailleau, S. Guillemet-Fritsch, R. Smith, E. Suard, and a. Rousset, “Structural variations and cation distributions in $Mn_{3-x}Co_xO_4$ ($0 \le x \le 3$) dense ceramics using neutron diffraction data,” *Solid State Sci.*, **12** [3] 379–386 (2010).

[74] A. Petric and H. Ling, “Electrical conductivity and thermal expansion of spinels at elevated temperatures,” *J. Am. Ceram. Soc.*, **90** [5] 1515–1520 (2007).

[75] M. Stanislowski, J. Froitzheim, L. Niewolak, W.J. Quadakkers, K. Hilpert, T. Markus, and L. Singheiser, “Reduction of chromium vaporization from SOFC interconnectors by highly effective coatings,” *J. Power Sources*, **164** [2] 578–589 (2007).

[76] C. Collins, J. Lucas, T.L. Buchanan, M. Kopczyk, A. Kayani, P.E. Gannon, M.C. Deibert, R.J. Smith, *et al.*, “Chromium volatility of coated and uncoated steel interconnects for SOFCs,” *Surf. Coatings Technol.*, **201** [7] 4467–4470 (2006).

[77] N. Koc and M. Timucin, “Activity-composition relations in $MnCr_2O_4$-$CoCr_2O_4$ solid solutions and stabilities of $MnCr_2O_4$ and $CoCr_2O_4$ at 1300°C,” *J. Am. Ceram. Soc.*, **88** [9] 2578–2585 (2005).

[78] R. Trebbels, T. Markus, and L. Singheiser, “Investigation of chromium vaporization from interconnector steels with spinel coatings,” *J. Electrochem. Soc.*, **157** [4] B490–B495 (2010).

[79] Z. Yang, K.S. Weil, D.M. Paxton, and J.W. Stevenson, “Selection and evaluation of heat-resistant alloys for SOFC interconnect applications,” *J. Electrochem. Soc.*, **150** [9] A1188 (2003).

[80] Kofstad, P. *High Temperature Corrosion.* Elsevier Applied Science/Chapman and Hall, London (1988).

[81] W.J. Quadakkers, T. Malkow, J. Piron-Abellan, U. Flesch, V. Shemet, L. Singheiser, “Suitability of ferritic stainless steels for applications as construction materials for SOFC interconnects”, 4th European SOFC Forum, 10-14 July 200, Lucerne, CH, Proceedings, Edt, McEvoy 827-836 (2000).

[82] J. Piron-Abellan, V. Shemet, F. Tietz, L. Singheiser, W.J. Quadakkers, 7th International Symposium on Solid Oxide Fuel Cells (SOFC VII) EPOCHAL, Tsukuba, Japan, 3-8 June 2001, Proceedings, The Electrochem. Soc. 147 Pennington N.J., USA, 2001 811-819 (2001).

[83] R. Hojda, W. Heimann, and W.J. Quadakkers, “Production-capable materials concept for high-temperature fuel cells,” *ThysennKrupp techforum*, **July** 20–22 (2003).

[84] L. Singheiser, J. Piron-Abellan, V. Shemet, and W.J. Quadakkers, “Ferritic steel in solid oxide fuel cells,” *V.D.I Berichte*, **1680** 267–274 (2002).

[85] Crofer 22 APU Material Data Sheet 4046 May 2010 Edition, Thyssen Krupp VDM.

[86] C. Barrett and T.B. Massalsku (ed.), *Structure of Metals*, 3rd Revised Edition, Pergamon Press, Oxford, (1980).

[87] J.K. Stanley, “The diffusion and solubility of carbon in alpha iron,” *Trans. Am. Inst. Min. Metall. Pet. Eng.,* **185** 752–761 (1949).

[88] E. Schürmann E. and R. Schmid, “The phase lines of the system iron-carbon of the stable and instable phase equilibria of austenite and ferrite with graphite and cementite and also the melt,” *Arch. Eisenhuettenwes.*, **50**, 185−188 (1979).

[89] J.R. Davis (ed.), *Metals Handbook Desk Edition*, 2nd Edition. ASM International, Materials Park, 1998.

[90] J. Froitzheim, G.H. Meier, L. Niewolak, P.J. Ennis, H. Hattendorf, L. Singheiser, and W.J. Quadakkers, “Development of high strength ferritic steel for interconnect application in SOFCs,” *J. Power Sources*, **178** [1] 163–173 (2008).

[91] L. Mikkelsen, *High Temperature Oxidation of Iron- Chromium Alloys*. Information Service Department Riso National Laboratory, Roskilde, 2003.

[92] J. Kunze, “Precipitation of titanium nitride in low-alloyed steel during cooling and deformation,” *Steel Res.*, **68** [10] 441–449 (1997).

[93] J. Kunze, C. Mickel, M. Leonhardt, and S. Oswald, “Precipitation of titanium nitride in low-alloyed steel during solidification,” *Steel Res.*, **68** [9] 403–408 (1997).

[94] F. Toscan, L. Antoni, Y. Wouters, M. Dupeux, and A. Galerie, “Oxidation kinetics and scale spallation of iron-chromium alloys with different titanium contents,” *Mater. Sci. Forum*, **461-464** 705–712 (2004).

[96] N.J. Magdefrau, L. Chen, E.Y. Sun, M. Aindow, L. Chen, E.Y. Sun, and M. Aindow, “Effects of alloy heat treatment on oxidation kinetics and scale morphology for Crofer 22 APU,” *J. Power Sources*, **241** 756–767 (2013).

[97] D.P. Whittle and J. Stringer, “Improvements in high temperature oxidation resistance by additions of reactive elements or oxide dispersions,” *Philos. Trans. R. Soc. A Math. Phys. Eng. Sci.*, **295** [1413] 309–329 (1980).

[98] P.Y. Hou and J. Stringer, “The effect of reactive element additions on the selective oxidation, growth and adhesion of chromia scales,” *Mater. Sci. Eng. A*, **202** 1–10 (1995).

[99] I. Melas and D.G. Lees, “Factors affecting adhesion of chromia scale on chromium,” *Mater. Sci. Technol.*, **4** (1988) 455 456.

[100] H.J. Schmutzler, H. Viefhaus and H.J. Grabke, “Influence of the oxide/metal interface composition on the adherence of oxide layers on metal substrates,” *Surf Interface Anal.*, **18** (1992) 581–584.

[101] Metals Handbook, Vol. 3: Properties and Selection: Stainless Steels, Tool Materials and Special Purpose Materials, American Society of Metals, Metals Park, OH (1980).

[102] J.E. Hammer, S.J. Laney, R.W. Jackson, K. Coyne, F.S. Pettit, and G.H. Meier, “The oxidation of ferritic stainless steels in simulated solid-oxide fuel-cell atmospheres,” *Oxid. Met.*, **67** [1-2] 1–38 (2007).

[103] W.J. Quadakkers, J. Piron-Abellan, V. Shemet, and L. Singheiser, “Metallic interconnectors for solid oxide fuel cells-a review,” *Mater. High Temp.*, **20** [2] 115–127 (2003).

[104] Y. Ustinovshikov and B. Pushkarev, “Morphology of Fe – Cr alloys,” *Mater. Sci. Eng. A*, **241** 159–168 (1998).

[105] M.J. Marcinkowski and D.S. Miller, “A study of defect sub-structures in the Fe-Cr sigma phase by means of transmission electron microscopy,” *Philos. Mag.*, **78** [7] 1025–1059 (1962).

[106] L. Reinhard, J.L. Robertson, S.C. Moss, G.E. Ice, P. Zschack, S.C. Sparks, “Anomalous-X-ray-scattering study of local order in BCC $Fe_{53}Cr_{47}$,” *Phys. Rev.*, **B45** (1992) 2662–2676.

[107] I. Barin, Thermochemical Data of Pure Substances (VCH Verlagsgesellschaft: Weinheim, 1993).

[108] M.G.C. Cox, B. McEnaney, and V.D. Scott, “Chemical diffusion model for partitioning of transition elements in oxide scales on alloys,” *Philos. Mag.*, **26** [4] 839–851 (1972).

[109] X. Pang, K. Gao, H. Yang, L. Qiao, Y. Wang, and a. a. Volinsky, “Interfacial microstructure of chromium oxide coatings,” *Adv. Eng. Mater.*, **9** [7] 594–599 (2007).

[110] A. Kantor, I. Kantor, M. Merlini, K. Glazyrin, C. Prescher, M. Hanfland, L. Dubrovinsky, "High-pressure structural studies of eskolaite by means of single-crystal X-ray diffraction," *Am. Mineral.,* **97** 1764–1770 (2012).

[111] R.E. Newnham and Y.M. de Haan, "Refinement of the alpha Al_2O_3, Ti_2O_3, V_2O_3 and Cr_2O_3 structures locality: synthetic," *Zeitschrift fur Kristallographie*, **117** 235–237 (1962).

[112] A. Holt and P. Kofstad, "Electrical conductivity and defect structure of Cr_2O_3. I. High temperatures (>~1000 °C)," *Solid State Ionics*, **69** 127–136 (1994).

[113] A. Holt and P. Kofstad, "Electrical conductivity and defect structure of Cr_2O_3. II. Reduced temperatures (<~1000 °C)," *Solid State Ionics*, **69** 137–143 (1994).

[114] E.W.A. Young, J.H. Gerretsen, and J.H.. Wit, "The oxygen partial pressure dependence of the defect structure of chromium(Ill)oxide," *J. Electrochem. Soc.*, **134** 2257–2260 (1987).

[115] J.-H. Park and K. Nateson, "Electronic transport in thermally grown Cr_2O_3," *Oxid. Met.*, **33** [1/2] 31–54 (1990).

[116] A. Holt and P. Kofstad, "Electrical conductivity of Cr_2O_3 doped with TiO_2," *Solid State Ionics*, **117** [3] 21–25 (1999).

[117] K. El-Menshawy, H.P. Buchkremer, F. Tietz, and D. Stoever, "Electrical conductivity of sintered chromia mixed with TiO_2 , CuO and Mn-Oxides," *J. Mater. Sci. Technol.*, **22** [2] 245–251 (2006).

[118] H.-S. Seo and K.-Y. Kim, "Electric and ionic property of oxide scale formed on ferritic stainless steel containing titanium;" in *18th Int. Corros. Congr. 2011,*. Perth, Australia, 2011.

[119] W.C. Hagel and a U. Seybolt, "Cation diffusion in Cr_2O_3," *J. Electrochem. Soc.*, **108** [12] 1146–1152 (1961).

[120] N. Iordanova, M. Dupuis, and K.M. Rosso, "Theoretical characterization of charge transport in chromia (alpha-Cr_2O_3).," *J. Chem. Phys.*, **123** [7] 074710 (2005).

[121] J.T. Devreese, "Polarons," *Encycl. Appl. Phys.*, **14** 383–409 (1996).

[122] L. D. Landau, *Phys. Z. Sowjetunion English translation, Collected Papers*, New York Gordon and Breach 67–68 (1965).

[123] B. Chattopadhyay and G.C. Wood, "The transient oxidation of Fe-Cr and Ni-Cr alloys," *J. Electrochem. Soc.*, **117** [9] 1163 (1970).

[124] T. Horita, H. Kishimoto, K. Yamaji, Y. Xiong, M. Brito, H. Yokokawa, Y. Baba, K. Ogasawara, *et al.*, "Diffusion of oxygen in the scales of Fe–Cr alloy interconnects and oxide coating layer for solid oxide fuel cells," *Solid State Ionics*, **179** [38] 2216–2221 (2008).

[125] S.C. Tsai, A.M. Huntz, and C. Dolin, "Growth mechanism of Cr_2O_3 scales: oxygen and chromium diffusion, oxidation kinetics and effect of yttrium," *Mater. Sci. Eng. A*, **212** 6–13 (1996).

[126] K. Hoshino and N. Peterson, "Cation self-diffusion in Cr_2O_3," *Commun. Am. Ceram. Soc.*, [November] C202–C203 (1983).

[127] T. Horita, Y. Xiong, K. Yamaji, N. Sakai, and H. Yokokawa, "Evaluation of Fe-Cr alloys as interconnects for reduced operation temperature SOFCs," *J. Electrochem. Soc.*, **150** [3] A243 (2003).

[128] Y. Zhao and J.W. Fergus, "Oxidation of alloys 430 and 441 in SOFC dual atmospheres: effects of flow rate and humidity," *J. Electrochem. Soc.*, **159** [3] C109–C113 (2012).

[127] M.R. Ardigo, I. Popa, S. Chevalier, S. Weber, O. Heintz, and M. Vilasi, "Effect of water vapor on the oxidation mechanisms of a commercial stainless steel for interconnect application in high temperature water vapor electrolysis," *Oxid. Met.*, **79** [5-6] 495–505 (2012).

[128] P. Huczkowski, N. Christiansen, V. Shemet, L. Niewolak, J. Piron-Abellan, L. Singheiser, and W.J. Quadakkers, "Growth mechanisms and electrical conductivity of oxide scales on ferritic steels proposed as interconnect materials for SOFC's," *Fuel Cells*, **6** [2] 93–99 (2006).

[129] S. Fontana, S. Chevalier, and G. Caboche, "Metallic interconnects for solid oxide fuel cell: effect of water vapour on oxidation resistance of differently coated alloys," *J. Power Sources*, **193** [1] 136–145 (2009).

[130] S.R.J. Saunders, M. Monteiro, and F. Rizzo, "The oxidation behaviour of metals and alloys at high temperatures in atmospheres containing water vapour: a review," *Prog. Mater. Sci.*, **53** [5] 775–837 (2008).

[131] M.R. Ardigo, I. Popa, S. Chevalier, S. Weber, O. Heintz, and M. Vilasi, "Effect of water vapor on the oxidation mechanisms of a commercial stainless steel for interconnect application in high temperature water vapor electrolysis," *Oxid. Met.*, **79** [5-6] 495–505 (2012).

[132] Y. Larring, R. Haugsrud, and T. Norby, "HT corrosion of a Cr-5 wt % Fe-1 wt % Y_2O_3 alloy and conductivity of the oxide scale," *J. Electrochem. Soc.*, **150** [8] B374 (2003).

[133] W.H. Bragg, “The structure of the spinel group of crystals,” Philos. Mag., **30** [176] 305–15 (1915).

[134] S. Nishikawa, “Structure of some crystals of the spinel group,” Proc. Math. Phys. Soc. Tokyo, **8**, 199–209 (1915).

[135] K. Sickafus and J. Wills, “Structure of spinel,” *J. Am. Ceram. Soc.*, **82** 3279–3292 (1999).

[136] B. Mansour, N. Baffier, and M. Huber, “Distortion de type jahn-teller et repartition des cations dans les oxydes spinelles $CoMn_xCr_{2-x}O4$ (0<x<). etude par diffraction des rayons x et des neutrons.,” *C.R. Acad. Sc. Paris*, **277** [Série C] 867–869 (1973).

[137] C.C. Fischer, K.J. Tibbetts, D. Morgan, and G. Ceder, “Predicting crystal structure by merging data mining with quantum mechanics.,” *Nat. Mater.*, **5** [8] 641–6 (2006).

[138] F. S. Galasso, Structure and Properties of Inorganic Solids. Pergamon Press, Oxford, U.K., 1970.

[139] R.D. Shannon, “Revised effective ionic radii and systematic studies of interatomic distances in halides and chalcogenides,” *Acta Crystallogr.*, **32** [5] 751–767 (1976).

[140] H.S.C. O’Neill and A. Navrotsky, “Simple spinels: crystallographic parameters, cation radii, lattice energies, and cation distribution,” *Am. Mineral.*, **68** 1983 (1983).

[141] A. Purwanto, A. Fajar, H. Mugirahardjo, J.W. Fergus, and K. Wang, “Cation distribution in spinel $(Mn,Co,Cr)_3O_4$ at room temperature,” *J. Appl. Crystallogr.*, **43** [3] 394–400 (2010).

[142] A. Rousset, C. Tenailleau, P. Dufour, H. Bordeneuve, I. Pasquet, S. Guillemet-Fritsch, V. Poulain, and S. Schuurman, “Electrical properties of $Mn_{3-x}Co_xO_4$ ($0 \le x \le 3$) ceramics: an interesting system for negative temperature coefficient thermistors,” *Int. J. Appl. Ceram. Technol.*, **10** [1] 175–185 (2013).

[143] P.L. Meena, R. Kumar, C.L. Prajapat, K. Sreenivas, and V. Gupta, “Dielectric studies of $Co_{3-x}Mn_xO_4$ (x=0.1–1.0) cubic spinel multiferroic,” *J. Appl. Phys.*, **106** [2] 024105 (2009).

[150] J.-L. Benard, N. Baffier, and M. Huber, “Distorsion cristalline et distribution des cations dans les spinelles de la serie $CoMn_xFe_{2-x}O_4$,” *J. Solid State Chem.*, **8** [1] 50–56 (1973).

[151] G.F. Dionne, “Theory of Co^{2+} exchange isolation in ferrimagnetic spinels and garnets,” *J. Appl. Phys.*, **64** [3] 1323–1331 (1988).

[152] E. Pollert, “Crystal chemistry of magnetic oxides part 1: general problems - spinels,” *Prog. Cryst. Growth Charact.*, **9** 263–323 (1984).

[153] F. de Boer, J.H. van Santen, and E.J.W. Verwey, “The electrostatic contribution to the lattice energy of some ordered spinels,” *J. Chem. Phys.*, **18** [8] 1032–1034 (1950).

[154] N. W. Grimes, P. Thompson, and H. F. Kay, “New symmetry and structure for spinel,” *Proc. Phys. Soc., London*, Sect. A, 386, 333–345 (1983).

[155] D.S. McClure, “The distribution of transition metal cations in spinels,” *J. Phys. Chem. Solids*, **3** 311–317 (1957).

[156] E. Pollert, “Ordering in spinels and perovskites,” *React. Solids*, **5** 279–291 (1988).

[157] J.K. Burdett, G.D. Price, and S.L. Pricelb, “Role of the crystal-field theory in determining the structures of pinels,” *J. Am. Chem. Soc.*, **104** 92–95 (1982).

[158] G.P. Glasby, “Limitations of crystal field theory applied to sedimentary systems,” *Geoderma*, **13** [4] 363–367 (1975).

[159] J.E. Iglesias, “Crystal chemistry of AB_2X_4 (X = S, Se, Te) compounds,” *J. Solid State Chem.*, **6** [1] 119–125 (1973).

[160] A. Navrotsky and O.J. Kleppa, “Thermodynamics of cation distributions in simple spinels,” *J. Inorg. Nucl. Chem.*, **29** [11] 2701–2714 (1967).

[161] H. Bordeneuve, A. Rousset, C. Tenailleau, and S. Guillemet-Fritsch, “Cation distribution in manganese cobaltite spinels Co3-x Mn x O4 ($0 \leq x \leq 1$) determined by thermal analysis,” *J. Therm. Anal. Calorim.*, **101** [1] 137–142 (2010).

[162] H. Bordeneuve, S. Guillemet-Fritsch, A. Rousset, S. Schuurman, and V. Poulain, “Structure and electrical properties of single-phase cobalt manganese oxide spinels $Mn_{3-x}Co_xO_4$ sintered classically and by spark plasma sintering (SPS),” *J. Solid State Chem.*, **182** [2] 396–401 (2009).

[163] Y.E. Roginskaya, O.V. Morozova, E.N. Lubnin, Y.E. Ulitina, G.V. Lopukhova, and S. Trasatti, “Characterization of bulk and surface composition of $Co_xNi_{1-x}O_y$ mixed oxides for electrocatalysis,” *Langmuir*, **13** 4621–4627 (1997).

[164] N.K. Appandairajan and J. Gopalakrishnan, “A study of $Co_{3-x}Ni_xO_3$ ($0<x<1$) system,” *Proc. Indian Acad. Sci*, **87 A** [4] 115–120 (1978).

[165] S. Fritsch, J. Sarrias, M. Brieu, J.J. Couderc, J.L. Baudour, E. Snoeck, and a. Rousset, “Correlation between the structure , the microstructure and the electrical properties of nickel manganite negative temperature coefficient (NTC) thermistors,” *Solid State Ionics*, **109** 229–237 (1998).

[166] T. Yokoyama, Y. Kumashiro, Y. Abe, T. Meguro, and K. Komeya, “Revaluation of cation radii of Mn, Co, and Ni in spinel-type oxides,” *J. Aust. Ceram. Soc.*, **34** [1] 30–34 (1998).

[167] T. Yokoyama, Y. Abe, T. Meguro, K. Komeya, K. Kondo, S. Kaneko, and T. Sasamoto, “Preparation and electrical properties of sintered bodies composed of monophase spinel $Mn_{(2-x)}Co_{2x}Ni_{(1-x)}O4$ (0<x<1) derived from rock-salt-type oxides,” *Jpn. J. Appl. Phys.*, **35** [11] 5775–5780 (1996).

[168] T. Yokoyama and T. Meguro, “Relationship between average cation radii and oxygen parameter for various oxides with spinel-type structure,” *Japanese J. Appl. Physics, Part 1 Regul. Pap. Short Notes Rev. Pap.*, **44** [8] 6201–6203 (2005).

[169] T. Meguro, Y. Abe, T. Yokoyama, S. Murosawa, K. Komeya, and J. Tatami, “Effect of oxygen partial pressure during firing on electrical properties of sintered body composed of $Mn_{1.5}CoNi_{0.5}O_4$,” *Jpn. J. Appl. Phys.*, **40** [8] 5041–5045 (2001).

[170] D.G. Wickham, “The chemical composition of spinels in the system Fe_3O_4-Mn_3O_4,” *J. Inorg. Nucl. Chem.*, **31** [2] 313–320 (1969).

[171] T. Battault, R. Legros, and a. Rousset, “Structural and electrical properties of iron manganite spinels in relation with cationic distribution,” *J. Eur. Ceram. Soc.*, **15** 1141–1147 (1995).

[172] G.F. Dionne, “Origin of the magnetostriction effects from Mn^{3+}, Co^{2+}, and Fe^{2+}ions in ferrimagnetic spinels and garnets,” *J. Appl. Phys.*, **50** [6] 4263–4272 (1979).

[173] V. Šepelák, D. Baabe, F.J. Litterst, and K.D. Becker, “Structural disorder in the high-energy milled magnesium ferrite,” *J. Appl. Phys.*, **88** [10] 5884 (2000).

[174] D.K. Kulkarani and C. Mande, “X-ray study of the structural and ionic configuration of the $CoMnCrO_4$ spinel,” *Acta Crystallogr. Sect. B Struct. Crystallogr. Cryst. Chem.*, **27** [5] 1044–1047 (1971).

[175] R.J. Hill, J.R. Craig, and G.V. Gibbs, “Systematics of the spinel structure type,” *Phys. Chem. Miner.*, **4** [1] 21–41 (1979).

[176] J.D. Dunitz and L.E. Orgel, “Electronic properties of transistion-metal oxides-I distortions from cubic symmetry,” *J. Phys. Chem. Solids*, **3** 20–29 (1957).

[177] P.J. Wojtowicz, “Theoretical model for cubic-to-tetragonal phase transformations in transition metal spinels,” *J. Appl. Phys.*, **30** [4] S30–S31 (1959).

[178] P.K. Baltzer and P.J. Wojtowicz, “On the origin of low moments in chromium-containing spinels,” *J. Appl. Phys.*, **30** [4] S27–S30 (1959).

[179] F.A. Cotton, G. Wilkinson, C.A Murillo, and M. Bochmann, *Advanced Inorganic Chemistry* (6th ed.), Wiley-Interscience New York (1999).

[180] F. Tielens, M. Calatayud, R. Franco, J.M. Recio, J. Pérez-Ramírez, and C. Minot, "Theoretical investigation of the inversion parameter in $Co_{3-s}Al_sO_4$ (s=0–3) spinel structures," *Solid State Ionics*, **180** [14-16] 1011–1016 (2009).

[181 F. Tielens, M. Calatayud, R. Franco, J.M. Recio, J. Pe, M. Curie, P. Vi, and P. Jussieu, "Periodic DFT study of the structural and electronic properties of bulk $CoAl_2O_4$ spinel," *J. Phys. Chem. B*, **110** 988–995 (2006).

[182] R. Franco, F. Tielens, M. Calatayud, and J.M. Recio, "Cation distributions on $CoAl_2O_4$ and Co_2AlO_4 spinels: pressure and temperature effects," *High Press. Res.*, **28** [4] 521–524 (2008).

[183] N.W. Grimes, "Self-diffusion compounds with spinel structure," *Philos. Mag.*, **25** [1] 67–76 (1972).

[184] T. Battault, R. Legros, and a. Rousset, "Structural and electrical properties of iron manganite spinels in relation with cationic distribution," *J. Eur. Ceram. Soc.*, **15** 1141–1147 (1995).

[185] P. Poix, "Sur une methode de determination des distances cation-oxygene dams les oxydes mixtes a structure spinelle, application des valeurs a queiques cas particuliers," *Bull. Soc. Chim. Fr.*, **5** 1085–1087 (1965).

[186] H.-Q. Wang, F.-Y. Lai, Y. Li, X.-H. Zhang, Y.-G. Huang, S.-J. Hu, and Q.-Y. Li, "Excellent stability of spinel $LiMn_2O_4$-based cathode materials for lithium-ion batteries," *Electrochim. Acta*, **177** 290–297 (2015).

[187] W. Hu, N. Qin, G. Wu, Y. Lin, S. Li, and D. Bao, "Opportunity of spinel ferrite materials in nonvolatile memory device applications based on their resistive switching performances," *J. Am. Chem. Soc.*, **134** [36] 14658–14661 (2012).

[188] K. Wang, Y. Liu, and J.W. Fergus, "Interactions between SOFC interconnect coating materials and chromia," *J. Am. Ceram. Soc.*, **94** [12] 4490–4495 (2011).

[189] W. Huang, S. Gopalan, U.B. Pal, and S.N. Basu, "Evaluation of electrophoretically deposited $CuMn_{1.8}O_4$ spinel coatings on Crofer 22 APU for solid oxide fuel cell interconnects," *J. Electrochem. Soc.*, **155** [11] B1161–B1167 (2008).

[190] G. V. Pattarkine, N. Dasgupta, and A. V. Virkar, "Oxygen transport resistant and electrically conductive perovskite coatings for solid oxide fuel cell interconnects," *J. Electrochem. Soc.*, **155** [10] B1036 (2008).

[191] D.M. England and A. V Virkar, “Oxidation kinetics of some nickel-based superalloy foils and electronic resistance of the oxide scale formed in air part I,” *J. Electrochem. Soc.*, **146** [9] 3196–3202 (1999).

[192] I. Barin, Thermochemical Data of Pure Substances (VCH Verlagsgesellschaft: Weinheim, 1993).

[193] J.W. Fergus, K. Wang, and Y. Liu, “Effect of titanium and iron additions on the transport properties of manganese cobalt spinel oxide,” *Adv. Mater. Sci. Environ. Nucl. Technol. II*, **227** 33–37 (2011).

[194] Y. Liu, C.J.D. Kumar, and J.W. Fergus, “Electrical properties of transition metal-doped $(Mn,Co)_3O_4$ spinels and their interaction with chromia for SOFC interconnect coatings,” *ECS Trans.*, **45** [1] 421–427 (2012).

[195] C.J.D. Kumar, A. Dekich, H. Wang, Y. Liu, W. Tilson, J. Ganley, and J.W. Fergus, “Transition metal doping of manganese cobalt spinel oxides for coating SOFC interconnects,” *J. Electrochem. Soc.*, **161** [1] F47–F53 (2014).

[196] R. Sun, “Diffusion of cobalt and chromium in chromite spinel,” *J. Chem. Phys.*, **28** [2] 290 (1958).

[197] L. V. Azároff, “Role of crystal structure in diffusion. I. Diffusion paths in closest-packed crystals,” *J. Appl. Phys.*, **32** [9] 1658–1662 (1961).

[198] Z. Yang, G. Xia, and J.W. Stevenson, “$Mn_{1.5}Co_{1.5}O_4$ spinel protection layers on ferritic stainless steels for SOFC interconnect applications,” *Electrochem. Solid-State Lett.*, **8** [3] A168–A170 (2005).

[199] M. J. Radler, J. B. Cohen, G. P. Sykora, T. Masn, D. E. Ellis and J. Faber, “The defect structures of $Mn_{1-x}O$,” J. *Phys. Chem. Sol*., **53** 141–154 (1992).

[200] Z. Yang, G. Xia, X. Li, and J. Stevenson, “$(Mn,Co)_3O_4$ spinel coatings on ferritic stainless steels for SOFC interconnect applications,” *Int. J. Hydrogen Energy*, **32** [16] 3648–3654 (2007).

[201] N.J. Magdefrau, L. Chen, E.Y. Sun, M. Aindow, E.Y. Sun, and L. Chen, “The effect of $Mn_{1.5}Co_{1.5}O_4$ coatings on the development of near surface microstructure for haynes 230 oxidized at 800°C in air,” *Surf. Coatings Technol.*, **242** 109–117 (2014).

[202] T. Onozuka, S. Yamaguchi, M. Hirabayashi, and T. Wakiyama, “Double HCP phase in cobalt alloys with dilute contents of iron,” *J. Phys. Soc. Japan*, **37** [3] 686–693 (1974).

[203] T. Brylewski, M. Nanko, T. Maruyama, and K. Przybylski, “Application of Fe – 16Cr ferritic alloy to interconnector for a solid oxide fuel cell,” *Solid State Ionics*, **143** 131 – 150 (2001).

[204] M. J. Garcia-Vargas, L. Lelait, V. Kolarik, H. Fietzek and M. Juez- Lorenzo, “Oxidation of potential SOFC interconnect materials, Crofer 22 APU and avesta 353 MA, in dry and humid air studied by x-ray diffraction,” *Mater. High Temp*., **22** [3/4] 245–251 (2005).R.E.

[205] Lobnig, “Diffusion of cations in chromia layers grown on iron-base alloys,” *Oxid. Met.*, **37** [1-2] 81–93 (1992).

[206] P. Kofstad, *High temperature corrosion*, (1st ed.), Chap. 8, “Effects of water vapour on oxidation behaviour,” London, *Springer* 383–389 (1988).

[207] J. Issartel, S. Martoia, F. Charlot, V. Parry, G. Parry, R. Estevez and Y. Wouters, “High temperature behavior of the metal/oxide interface of ferritic stainless steels,” *Corros. Sci.*, **59** 148–156 (2012).

[208] G. Blasse, “Crystal chemistry and some magnetic properties of mixed metal oxides with spinel structures,” *Philips Res. Rep. Suppl*., **3** 1−139 (1964).

[209] R.F. Cooley and J.S. Reed, “Equilibrium cation distribution in $NiAl_2O_4$, $CuAl_2O_4$, and $ZnAl_2O_4$ Spinels,” *J. Am. Ceram. Soc.*, **55** [8] 395–398 (1972).

[210] H. Schmalzried, “Radiographic investigation of cation distribution in spinel phases,” *Z. Phys. Chem.*, **28**, 203-19 (1961).

[211] B. Boucher, R. Buhl, R. Di Bella, and M. Perrin, “Etude par des mesures de diffraction de neutrons et de magnétisme des propriétés cristallines et magnétiques de composés cubiques spinelles $Co_{3-x}Mn_xO_4$ (0,6 ≤ x ≤ 1,2)” *J. de Physique* **31** [1], 113-9 (1970).

[212] C.J. Kriessman and S.E. Harrison, “Cation distributions in ferrospinels. Magnesium-manganese ferrites”, *Phys. Rev.* **103** [4], 857-60 (1956).

[213] J. De Sitter, A. Govaert, E. De Grave, and D. Chambaere, “Mossbauer spectroscopy as a tool for the investigation of industrial iron ore sinters”, *Bulletin des Sociétés Chimiques Belges*, **86** [11], 851-849 (1977).

[214] J. Tafto, and J.C.H. Spence, “Atomic site determination using the channeling effect in electron-induced x-ray emission”, *Ultramicroscopy*, **9** [3], 243–7 (1982).

[215] J.C.H. Spence, and J. Tafto, “ALCHEMI: a new technique for locating atoms in small crystals”, *J. Microscopy*, **130** [2], 147-54 (1982).

[216] Z. Horita, S. Matsumura, and T. Baba, “General formulation for ALCHEMI”, *Ultramicroscopy*, **58** [3-4], 327–35 (1995).

[217] N. Jiang, D.H. Hou, and I.P. Jones, “Optimizing the ALCHEMI technique”, *Philos. Mag. A*, **79** [10], 2525–38 (1999).

[218] I.P. Jones, “Determining the locations of chemical species in ordered compounds: ALCHEMI”, *Adv. Imaging Electron Phys.*, **125,** 63–117 (2002).

[219] J.C.H. Spence, and J. Tafto, “Atomic site and species determination using the channeling effect in electron diffraction”, *Scanning Electron Microscopy*, **2**, 523-31 (1982).

[220] J.R. Smyth, and T.C. McCormick, “Earth science applications of ALCHEMI”, *Ultramicroscopy*, **26** [1-2], 77-85 (1988).

[221] C.J. Rossouw, P.S. Turner, T.J. White, and A.J. O'Connor, “Statistical analysis of electron channelling microanalytical data for the determination of site occupancies of impurities”, *Phil. Mag. Lett.,* **60** [5], 225-32 (1989).

[222] L.J. Allen, T.W. Josefsson, and C.J. Rossouw, “Interaction delocalization in characteristic x-ray emission from light elements”, *Ultramicroscopy*, **55** [3], 258-67 (1994).

[223] T. Soeda, S. Matsumura, C. Kinoshita, and N.J. Zaluzec, “Cation disordering in magnesium aluminate spinel crystals induced by electron or ion irradiation”, *J. Nuc. Mater.*, **283-287**, 952-6 (2000).

[224] T. Sawabe, and T. Yano, “Neutron irradiation effect on site distribution of cations in non-stoichiometric magnesium aluminate spinel”, *J. Nuc. Mater.*, **373** [1-3], 328-34 (2008).

[225] L.A. Chick, G.D. Maupin, and L.R. Pederson, “Glycine-nitrate synthesis of a ceramic-metal composite,” *Nanostructured Mater.*, **4** [5], 603–15 (1994).

[226] S.R. Jain, K.C. Adiga, and V.R. Pai Verneker, “A new approach to thermochemical calculations of condensed fuel-oxidizer mixtures”, *Combust. Flame*, **40** [C], 71–9 (1981).

[227] D.H. Hou, I.P. Jones, and H.L. Fraser, “The ordering tie-line method for sublattice occupancy in intermetallic compounds” *Philos. Mag. A,* **74** [3], 741-60 (1996).

[228] S. Amancherla, R. Banerjee, S. Banerjee, and H.L. Fraser, “Ordering in ternary B2 alloys” *International Journal of Refractory Metals & Hard Materials* **18** [4-5], 245-52 (2000).

[229] K.J. Leonard, and V.K. Vasudevan, “Phase equilibria and solid state transformations in Nb-rich Nb-Ti-Al intermetallic alloys” *Intermetallics* **8** [9-11], 1257-68 (2000).

[230] R. Banerjee, S. Amancherla, S. Banerjee, and H.L. Fraser, “Modeling of site occupancies in B2 FeAl and NiAl alloys with ternary additions” *Acta Mater.* **50** [3], 633–41 (2002).

[231] T.S. Rong, D.N. Horspool, and M. Aindow, “Microstructure and mechanical behaviour of Nb-Al-V alloys with 10-25%Al and 20-40%V: I microstructural observations,” *Intermetallics* **10** [1], 1-12 (2002).

[232] Y.L. Hu, L.C. Zhang, D. Shuman, B.D. Huey, and M. Aindow, “Atomic site occupancies and mechanical response of the eutectic C14 and A15 phases in a quinternary Nb-Mo-Cr-Al-Si alloy,” *Scripta Mater* **60** [5], 309-12 (2009).

[233] L.C. Zhang, A.L. Vasiliev, I.B. Misirlioglu, R. Ramesh, S.P. Alpay, and M. Aindow, “Cation ordering in epitaxial lead zirconate titanate films,” *Appl Phys Lett* **93** [26], 262903 (1-3) (2008).

[234] E. Vila, R. M. Rojas, J. L. Martin de Vidales, and O. Garcia-Martinez, Structural and thermal properties of the tetragonal cobalt manganese spinels $Mn_xCo_{3-x}O_4$ ($1.4 < x < 2.0$), *Chem. Mater.* **8**, 1078-1083 (1996).

[235] N. Jiang, T.S. Rong, I.P. Jones, M. Aindow, “On the effect of antiphase domain boundaries on ALCHEMI,” *Phys. Stat. Sol. B*, **214** 237-243 (1999).

[236] K. Mocala and A. Navrotsky, “Structural and thermodynamic variation in nickel aluminate spinel,” *J. Am. Ceram. Soc.*, **72** [5] 826–832 (1988).

[237] Verwey JW, de Boer F, van Santen JH (1948) Cation arrangements in spinels, J Chem Phys, 16:1091-1092.

[238] J.H. Paterson and O.L. Krivanek, “ELNES of 3d transition-metal oxides. II. Variations with oxidation state and crystal structure,” *Ultramicroscopy*, **32** 319-325 (1990).

[239] H. Tan, J. Verbeeck, A. Abakumov, and G. Van Tendeloo, “Oxidation state and chemical shift investigation in transition metal oxides by EELS,” *Ultramicroscopy*, **116** 24-33 (2012).

[240] L.J. Allen “Electron energy loss spectroscopy in a crystalline environment using inner-shell ionization,” *Ultramicroscopy*, **48** 97-106 (1993).

[241] L.V. Gambino, N.J. Magdefrau, and M. Aindow, “Microstructural effects of the reduction step in the reactive consolidation of manganese cobaltite coatings on Crofer 22 APU”, *Mater. High Temp.*, **32** [1-2], 142-7 (2015).

[242] L. V Gambino, N.J. Magdefrau, and M. Aindow, “ALCHEMI studies of spinel oxides for SOFC interconnect alloy coatings,” *Microsc. Microanal.*, **21** [1137] 2277–2278 (2015).

[243] L.A. Chick, L.R. Pederson, G.D. Maupin, J.L. Bates, L.E. Thomas, and G.J. Exarhos, "Glycine-nitrate combustion synthesis of oxide ceramic powders," Mater. Lett. **10** 6-12 (1990).

[244] B. Bergman and J. Agren, "Thermodynamic assessment of the system CoO-MnO," J. Am. Ceram. Soc. **69** 877–881 (1986).

[245] E. Aukrust and A. Muan, "Activities of components in oxide solid solutions. The systems CoO-MgO, CoO-MnO, and CoO-FeO at 1200°C," Trans. Metall. Soc. AIM, **227** 1378–80 (1963).

[246] K. Przybylski and W.W. Smeltzer, "High temperature oxidation mechanism of CoO to Co_3O_4," J. Electrochem. Soc. **128** 897–902 (1981).

[247] E.A. Gulbransen and K.F. Andrew, "The kinetics of the oxidation of cobalt," *J. Electrochem. Soc.*, **98** [6] 241–251 (1951).

[248] L. V. Gambino, A.B. Freeman, N.J. Magdefrau, and M. Aindow, "ALCHEMI studies of site occupancies in Cr-, Ni-, and Fe-substituted manganese cobaltite spinels," *J. Mater. Sci.*, **1** [1] (2015).

[249] B.P. McCarthy, L.R. Pederson, Y.S. Chou, X.D. Zhou, W. a. Surdoval, and L.C. Wilson, "Low-temperature sintering of lanthanum strontium manganite-based contact pastes for SOFCs," *J. Power Sources*, **180** [1] 294–300 (2008).

[250] B.P. McCarthy, L.R. Pederson, R.E. Williford, and X.D. Zhou, "Low-temperature densification of lanthanum strontium manganite ($La_{1-x}Sr_xMnO_{3+\delta}$), x=0.0-0.20," *J. Am. Ceram. Soc.*, **92** [8] 1672–1678 (2009).

[251] O.L. Krivanek and J. Tafto, "EELS under standing wave conditions," *Proc. Electron Microsc. Soc. Am.*, **1** 492–495 (1982).

[252] R. Brydson, A.P. Brown, S. McBride, C. Calvert, and A.. Bell, "EELS ALCHEMI revisted," *Electron Microsc. Anal.*, **179** [7] 295–298 (2003).

[253] O.L. Krivanek, M.M. Disko, J. Tafto, and J.C.H. Spence, "Electron energy loss spectroscopy as a probe of the local atomic environment," *Ultramicroshcopy*, **9** 249–254 (1982).